Alma Mater Studiorum – Università di Bologna

DOTTORATO DI RICERCA IN

Meccanica e Scienze Avanzate dell'Ingegneria

Ciclo XXXIII

**Settore Concorsuale: 09/A1 Ingegneria Aeronautica, Aerospaziale e Navale**

**Settore Scientifico Disciplinare: ING-IND/05 Impianti e Sistemi Aerospaziali**

# ORBIT DETERMINATION TECHNIQUES FOR SPACE MISSIONS TO SMALL BODIES

**Presentata da:** **Riccardo Lasagni Manghi**

**Coordinatore Dottorato**

Prof. Marco Carricato

**Supervisore**

Prof. Paolo Tortora

**Co-Supervisore**

Marco Zannoni

**Esame finale anno 2021**

# Author's Note

This thesis is continuously revised to correct all typos that are found during a constant revision process. To obtain the most updated version, please feel free to contact the author by sending an e-mail to: riccardo.lasagni@unibo.it.

# Summary


## Part I

Precise radiometric tracking is of key importance to meet the demanding navigation and scientific requirements of the most recent deep space missions such as BepiColombo and Juice. Media propagation errors are one of the main error sources for radiometric observables, with fluctuations of tropospheric excess path length due to atmospheric components (e.g. gases, clouds, precipitation) representing one of the most relevant contributors to Doppler noise. Microwave radiometers currently represent the most accurate instruments for the determination of the water vapor content within the atmosphere and for the calibration of tropospheric delay along the slant path.

A prototype of a Tropospheric Delay Calibration System (TDCS), using a 14 channel $K_A$/V band microwave radiometer, has been developed under ESA contract and installed at the DS3 ESTRACK complex in Malargue on February 2019. After its commissioning, the TDCS has been involved in an extensive testbed campaign by recording a total of 44 tracking passes of the GAIA spacecraft, which were used to perform an orbit determination analysis to characterize the prototype performances in an operative scenario.

Section 1 introduces the problem of orbit determination and provides a summary of the mathematical formulation for the main radiometric observables used in the subsequent analysis.

Section 2 describes the analysis that was performed as a part of the TDCS testbed campaign using the MONTE software tool developed by JPL. This analysis, which does not replicate the full orbit determination solution used for the navigation of GAIA, is mostly intended as a side by side comparison of the filter performances when TDCS-based tropospheric calibrations are used in place of standard GNSS-based calibrations. The results will show that a reduction of the Doppler noise is obtained using TDCS data, with a magnitude that depends on the atmospheric conditions encountered at the time of the tracking pass. A consistent reduction is also observed in the Allan Standard Deviation of the Doppler residuals, although a significant amount of uncalibrated atmospheric instability is still observed for specific tracking arcs, suggesting that a fine tuning of the TDCS retrieval algorithms and processing procedures might lead to improved performances.

## Part II

Small bodies represent one of the most active research fields for planetary science and deep space exploration, as witnessed by the increasing number of missions towards these targets, such as the recent OSIRIS-REx and Hayabusa-2 missions or the future DART and Hera missions.

In this framework, Rosetta represented a crucial step towards a higher understating of small bodies, being the first mission to successfully orbit a cometary target. Being able to follow the temporal evolution of the surface activity as the comet moved though the perihelion and back to the outer regions of the Solar System, the Rosetta mission provided a unique test case to evaluate the physical properties of the comets.

Specifically, the work described in the second part of this thesis focuses on the ephemeris reconstruction of comet 67P/Churyumov-Gerasimenko for the period between July 2014 and October 2016, through a complete reanalysis of the ranging and ΔDOR measurements collected by Rosetta during its proximity phase with the comet. Using as input the relative orbit trajectory reconstructed by ESOC FD, the s/c radiometric observables were mapped to the comet nucleus and used to estimate the comet state and some key physical and observational parameters within a SRI batch filter implemented in MONTE, most notably the Non-Gravitational Acceleration acting on the comet nucleus due to surface outgassing.

Section 3 provides a detailed description of the Rosetta orbit determination setup and of the data processing procedures. Several test cases were explored by varying the model used to represent the non-gravitational acceleration. The results of this orbit determination analyses are then compared, using the reduced chi-square statistics to identify the most suitable trajectory estimations for each of the proposed models. From this narrow list of solutions, a preliminary selection for the final ephemeris reconstruction is proposed, based on its adherence to the original ESOC trajectory and on the consistency of its formal state uncertainties with the remaining candidate solutions. The main outcome of this work it thus represented by a continuous trajectory reconstruction for comet 67P/Churyumov-Gerasimenko, and a preliminary estimation of the non-gravitational accelerations acting on the comet during its active periods, which will serve as a baseline solution for more complex dynamical models of the evolution of the surface activity.

Finally, Section 4 highlights the main conclusions of the studies described within this PhD thesis, and outlines the open points that will be addressed in future investigations.

# Acknowledgements

First of all I would like to thank my supervisor, Professor Paolo Tortora, for trusting me with the opportunity of this PhD position and for introducing me to the fascinating fields of radioscience and space exploration.
A huge thanks to my colleague and friend Marco Zannoni, for his continuous support and for the stimulating discussions (sometimes occurring at prohibitive hours of the night).

A heartfelt thanks to Alberto Graziani, Gerrit Maschwitz, Antonio Martellucci, Javier De Vicente, Jose Villalvilla, Mattia Mercolino, and all the other ESA and RPG personnel involved in the TDCS development, for trusting an unexperienced young professional with such challenging yet rewarding tasks.

A sincere thanks to Frank Budnik and Ruaraidh Mackenzie for their continuous support and suggestions, which proved to be incredibly helpful for completing this work.

A big thanks to all my friends and colleagues at the Radio Science and Planetary Exploration laboratory, for the great moments we had in these past few years. Working alongside such passionate and positive people is the reason why I go to work every day with a smile.

And last, but not least, a huge thanks to my family. To Maura, Alberto, and Federico, for their unconditional support and love throughout these years.

# Contents

# Acronyms

| | |
|---|---|
| **AOCS** | Attitude and Orbital Control System |
| **ASD** | Allan Standard Deviation |
| **AU** | Astronomical Units |
| **CAPS** | Calibration, data Acquisition, and Processing System |
| **COB** | Center Of Brightness |
| **COM** | Center Of Mass |
| **CSM** | Constant Stochastic Model (for NGA representation) |
| **DSA** | Deep Space Antenna |
| **DSN** | Deep Space Network |
| **DOR** | Differential One-way Ranging |
| **ECMWF** | European Center for Medium-Range Weather Forecasts |
| **EME2000** | Earth Mean Equator at J2000 |
| **EMO2000** | Earth Mean Orbit at J2000 |
| **EoM** | End of Mission |
| **EOP** | Earth Orientation Parameters |
| **ESA** | European Space Agency |
| **ESM** | Extended Standard Model (Yeomans & Chodas) |
| **ESTRACK** | ESA Tracking Stations Network |
| **ET** | Ephemeris Time |
| **FD** | Flight Dynamics |
| **GNSS** | Global Navigation Satellite System |
| **ICRS** | International Celestial Reference Frame |
| **IFMS** | Intermediate Frequency and Modem System |
| **IWV** | Integrated Water Vapor |
| **LSM** | Linear Stochastic Model (for NGA representation) |
| **LOS** | Line Of Sight |
| **LWP** | Liquid Water Path |
| **MWR** | Microwave Radiometer |
| **NN** | Neural Network |
| **OCM** | Orbit Control Maneuver |
| **OD** | Orbit Determination |
| **POS** | Plane Of the Sky |
| **PSD** | Power Spectral Density |
| **RJM** | Rotating Jet Model |
| **RMS** | Root Mean Square |
| **RPG** | Radiometer Physics GMBH (A Rohde & Schwarz Company) |
| **SEP** | Sun Earth Probe angle |

| | |
|---|---|
| **SHD** | Slant Hydrostatic Delay |
| **SM** | Standard Model (Mardsen) |
| **SPK** | Spacecraft Kernel |
| **TB** | Brightness Temperature |
| **TDCS** | Tropospheric Delay Calibration System |
| **TDM** | Trajectory Data Message |
| **TTCP** | Telemetry and Telecommand Processor |
| **UTC** | Coordinated Universal Time |
| **VLBI** | Very Large Base Interferometry |

# 1 The orbit determination problem

The orbit determination problem is an iterative process, which consists in estimating the trajectory of a target body and a series of related physical parameters from a set of tracking measurements. A schematic representation of this process is given in Figure 1-1.

Starting from an a-priori estimation of the target's state and of the physical parameters, the trajectory is propagated using an accurate dynamical model, which should include all relevant forces acting on the system. Expected values for the tracking observables are computed using detailed observation models and compared with the observed measurements. If the dynamic and the observation models were perfectly known, the residuals would show a zero mean and purely random behavior.

In real world scenarios, dynamic and observation mismodelling cause the residuals to show characteristic signatures (i.e. biases, drifts, discontinuities) that can be used to adjust the model parameters through the process of weighted least square linear estimation. In this process, the optimal solution is defined as the one minimizing the weighted sum of the squares of the residuals, which also represents the solution of minimum variance when the inverse of the measurement error covariance is used to weight the measurements.

Since dynamic and observation models are often non-linear, this procedure is repeated, using the previous estimated parameters as a-priori values for the new iteration, until convergence is reached.

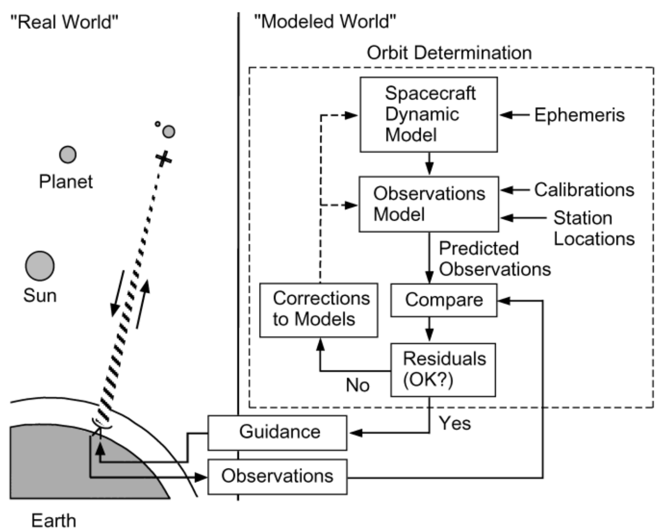


Figure 1-1 Schematic representation of the orbit determination process (credit [1])

## 1.1 Radiometric Observables

Since the beginning of the deep space exploration in the early 1960s, s/c tracking has been mainly performed using optical and radiometric measurements[1]. While the optical measurements are becoming increasingly common for missions that require a high level of autonomy, as is the case for small-body exploration, the most widely used tracking observable is still represented by radiometric measurements exploiting the radio link between the s/c and the Earth ground stations.

[1] In the context of radioscience and orbit determination, the term radiometric measurement is used to define RF tracking links between a ground station on Earth and a deep space probe. In the context of microwave remote sensing, this term refers to the measurement of physical properties (e.g. power and polarization) of spontaneously emitted radiation from the atmosphere or other natural surfaces (e.g. ground or seas).

Starting from the initial S-band capabilities, developed by the Deep Space Network (DSN), X-band and $K_A$-band capabilities were slowly introduced to improve the measurement quality.

Several tracking configurations are currently used, the most common of which is the two-way link, for which the signal is generated and transmitted by an Earth ground station, received by the s/c and transmitted back to the same station. This configuration allows to have the same frequency standards for uplink and downlink, using the highly stable reference provided by the ground station clock.

Another configuration is the three-way link, for which the receiving and transmitting ground stations are different. Although less accurate than a two-way link, due to the different frequency standards at the transmitting and receiving stations, this configuration is often necessary for deep space missions towards the outer Solar System, where the long round-trip light times limit the useful tracking time for s/c navigation.

Finally, a few radiometric observables exploit the so called on-way link, for which the signal is generated onboard the s/c and transmitted directly to the Earth ground station. This configuration provides higher flexibility by decoupling s/c and GS operations. However, the accuracy of one-way measurements is often limited by the lower frequency stability of the onboard ultra-stable oscillators when compared to the GS time references.

In the next sections, a brief description will be given for the mathematical formulation of the light-time solution and for the most commonly used radiometric observables, namely Range, Doppler, and ΔDOR, which will also be used within the OD analyses described in Section 2 and Section 3.

### 1.1.1 Light-time solution

For a correct modelling of radiometric observables it is necessary to compute the accurate times at which the radio signal interacts with each participant, namely the transmitting station ($t_1$), the spacecraft transponder ($t_2$), and the receiving station ($t_3$). From these, we define the up-link light time $\tau_{UL} = t_2 - t_1$, the down-link light time $\tau_{DN} = t_3 - t_2$, and the round-trip light time $RTLT = t_3 - t_1$.

Finding a solution for the light-time problem consists in finding the times of participation and the states of each participant evaluated at that time. Depending on the type of observable, the state could comprise only the position and velocity or require also the knowledge of the acceleration and the jerk.

The one-body light time equation (1.1), which is derived in [2], computes the time required to travel front point $r_i$ to point $r_j$ when a single massive body is present at the center of the coordinate reference frame.

$$t_j - t_i = \frac{1}{c}\left[r_{ij} + k_B \ln\left(\frac{r_i + r_j + r_{ij} + k_B}{r_i + r_j - r_{ij} + k_B}\right)\right] \tag{1.1}$$

$$k_B = \frac{(1+\gamma)\mu_B}{c^2} \tag{1.2}$$

In these expressions, $c$ is the speed of light in vacuum, $\gamma$ is the free parameter of Brans-Dicke theory of relativity, $\mu_B$ is the gravitational parameter of the massive body, $r_k$ is the absolute value of the position vector at time $t_k$, and$r_{ij}$ is the geometric straight line joining the vectors $r_i$ and $r_j$. The first term of (1.1) is the Newtonian contribution for light-time, while the second term is the relativistic contribution (abbreviated to $RLT_{ij}$), which accounts for both the propagation velocity reduction and for the bending of the light path.

The final expression for the one-way light time is given in (1.3) by summing the relativistic contributions for the Sun and for all Solar System bodies relevant to the analysis, which are “switched on” by the user in the dynamical model. It can be seen that the bending contribution to the relativistic term is used only for the Sun.

$$t_j - t_i = \frac{1}{c}\left[r_{ij} + k_S \ln\left(\frac{r_i^S + r_j^S + r_{ij}^S + k_S}{r_i^S + r_j^S - r_{ij}^S + k_S}\right) + \sum_{P=1}^{10} k_P \ln\left(\frac{r_i^P + r_j^P + r_{ij}^P}{r_i^P + r_j^P - r_{ij}^P}\right)\right] \tag{1.3}$$

The light-time equation in (1.3) is solved by defining the function $f$ in (1.4). For a given reception time $t_j$, the solution for the transmission time $t_i$ is the one for which this function goes to zero.

$$f = t_j - t_i - \frac{1}{c}[r_{ij} + RLT_{ij}] \tag{1.4}$$

A differential corrector for $t_i$ is then constructed, which drives $f$ linearly to zero:

$$f + \frac{\delta f}{\delta t_i}\Delta t_i = 0 \tag{1.5}$$

Starting from an initial guess for $t_i$, the corresponding values for $f$ and $\delta f/\delta t_i$ are computed and the correction $\Delta t_i$ is given by (1.6), where $\hat{\boldsymbol{r}}_{\boldsymbol{ij}}$ represents the geometric propagation direction, and $\dot{\boldsymbol{r}}_{\boldsymbol{i}}$ is the velocity of the transmitter. This equation is solved iteratively until a given convergence criterion for $\Delta t_i$ is met.

$$\Delta t_i = \frac{t_j - t_i - \frac{r_{ij}}{c} - RTL_{ij}}{1 - \frac{\hat{\boldsymbol{r}}_{\boldsymbol{ij}} \cdot \dot{\boldsymbol{r}}_{\boldsymbol{i}}}{c}} \tag{1.6}$$

The first contribution to be determined is the down-link light time $\tau_{DN}$. Starting from the reception time $t_3$, which corresponds to the time-tag of the observed radiometric measurements, $\tau_{DN}$ is computed using the iterative procedure described above and $t_2 = t_3 - \tau_{DN}$ is determined. For 2-way and 3-way links the up-link light time $\tau_{UP}$ is then computed to retrieve the up-link transmission time $t_1$.

### 1.1.2 Range

The basic principle behind ranging measurements is quite simple. By accurately measuring the time it takes for a radio signal to reach Earth after its transmission it is possible to determine the line of sight (LOS) geocentric distance of the target s/c by multiplying this quantity for the speed of light. However, what is actually measured with common radiometric systems is actually the fractional phase of the transmitted signal and not the transmission time itself.

An expression for the for 2-way observed range $R_{2way}$ is given in (1.7), where $f_T(t)$ is the time-dependent transmitted frequency (to account for possible ramps), $t_{3e}|_{ST}$ is the reception time at the station electronics (corresponding to the time-tag of the measured data), and $t_{1e}|_{ST}$ is the corresponding transmission time at the station electronics. For both the transmission and reception times, the specifier $|_{ST}$ indicates that the participation times are given in the local station time (usually UTC).

$$R_{2way} = \int_{t_{1e}|_{ST}}^{t_{3e}|_{ST}} f_T(t)dt\,, \quad mod\ M \tag{1.7}$$

The transmission time is derived from the reception time according to (1.8), where $\rho_{2way}$ is the precision round-trip light-time solution in (1.9). This last expression follows the definitions given in section 1.1.1, where $r_{ij}$ and $RLT_{ij}$ represent the Newtonian and relativistic contributions to light time propagation, $(ET - ST)$ is the correction between the Barycentric Dynamical Time (or Ephemeris Time) and the local station time, and $\Delta\rho$ represents the time delays due to the transmitting media, s/c transponder, and station electronics.

$$t_{1e}|_{ST} = t_{1e}|_{ST} - \rho_{2way} \tag{1.8}$$

$$\rho_{2way} = \frac{1}{c}[r_{12} + RLT_{12} + r_{23} + RLT_{23}] - (ET - ST)_{t_3} + (ET - ST)_{t_1} + \Delta\rho \tag{1.9}$$

It is important to note that only the fractional part of the phase difference can be measured, so range observables are intrinsically ambiguous. The integer number of cycles $M$ (the ambiguity) must be resolved as part of the OD process using the characteristics of the ranging signals. Depending on the signal structure, two main range types are currently in use:

- Sequential range signals consist in a sequence of periodic tones, all coherently related to each other, which are phase modulated onto the uplink carrier. The highest frequency component (clock) determines the measurement resolution, while the lowest frequency component determines the ambiguity resolution. This method has been widely used in the past decades by both NASA and ESA, which employ different schemes for their ranging system. NASA transmits one frequency component at a time, maximizing power, while ESA combines all components in a single code, reducing the transmission time.
- Pseudo-noise range (PN) signals are built from the logical combination of a clock component and a series of pseudo-noise components (binary ±1 sequences) of variable length for ambiguity resolution. Using this method allows to digitally detect and regenerate the signal onboard the s/c, ensuring a higher signal-to-noise ratio at downlink.

### 1.1.3 Doppler

Range-rate (or Doppler) observables are based on the measurement of the frequency shift of a received signal, with respect to the transmitted one, when the transmission participants are in relative motion with respect to each other.

The Doppler extraction process starts by subtracting the received carrier frequency from a local replica of the transmitted one, obtaining the so called Doppler tone. A cycle counter then measures the phase change of the Doppler tone, giving an indication of the range increment over the count-time.

Similarly to the range case, the most accurate Doppler measurements are obtained in two-way configuration, for which the receiving and transmitting station are the same and the highest frequency standards of the ground based oscillators can be exploited (as compared to onboard s/c oscillators).

A mathematical expression for the 2-way Doppler observables is given in (1.10), where $f_T(t)$ is the time-dependent transmitted frequency, $M_2$ is the s/c transponder ratio, and $T_C$ is the selected count-time for the measurement. The integration extremes $(t_{1e}|_{ST})_{beg}$ and $(t_{1e}|_{ST})_{end}$ represent the transmitting times at the start and at the end of the count-time interval, respectively.

$$D_{2way} = \frac{M_2}{T_C} \int_{(t_{1e}|_{ST})_{beg}}^{(t_{1e}|_{ST})_{end}} f_T(t)dt \tag{1.10}$$

If the transmitted frequency is constant, the expression in (1.10) simplifies to (1.11), where $\rho_{beg}$ and $\rho_{end}$ are the precision round-trip light times for the signals received at times $(t_{3e}|_{ST})_{beg}$ and $(t_{3e}|_{ST})_{end}$, respectively (corresponding to the beginning and end of the count-time interval).

$$D_{2way} = \frac{M_2 f_T}{T_C}(\rho_{end} - \rho_{beg}) \tag{1.11}$$

From the actual measured Doppler frequency $D_{2\,way}$ it is possible to retrieve the LOS range-rate in units of velocity according to (1.12).

$$\dot{\rho} = \frac{c\left(\rho_{end} - \rho_{beg}\right)}{T_C} \tag{1.12}$$

### 1.1.4 ΔDOR

Delta-Differential One-way Range (Delta-DOR or ΔDOR) is an observable commonly used in deep space tracking, which gives an almost instantaneous angular position of the target s/c with respect to a natural radio source (a Quasar), whose position in the plane of the sky is accurately known . This measurement relies on the same principles of Very Large Base Interferometry (VLBI), for which it represents a particular application.

#### *1.1.4.1 Very Large Base Interferometry (VLBI)*

The fundamental principle of VLBI measurements is shown in Figure 1-1. A signal from a distant source is simultaneously received by two antennas, separated by a large baseline distance; after processing, the received signals are cross correlated to determine the difference between the time of arrival at the two stations. In an ideal situation, this delay can be expressed as a purely geometric term, as shown in (1.13), where $\hat{s}$ is the unit vector towards the signal source, $\vec{B}$ is the baseline between the two stations and $c$ is the speed of light. Knowing the geometry of the stations, it is possible to determine the angle $\theta$ between the baseline and the source direction. Combining two or more VLBI measurements with different baseline geometries allows to determine the celestial coordinates of the source.

$$\tau_{geom} = \frac{1}{c}\vec{B} \cdot \hat{s} = \frac{1}{c} B\ cos\theta \tag{1.13}$$

The VLBI angular measurements are affected by several errors sources, including clock offsets and jitter between the two stations, instrumental delays, baseline orientation errors, and different media propagation delays along the observed line-of-sight (ionosphere and troposphere). The accuracy of VLBI measurements is determined by the accuracy to which these error source can be calibrated.

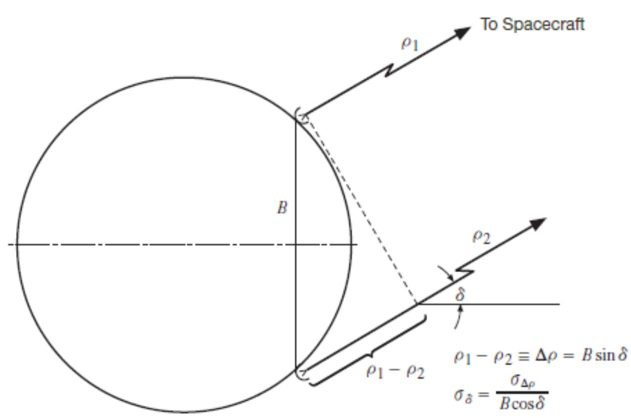


Figure 1-2 VLBI measurement principle

#### *1.1.4.2 ΔDOR*

An effective way to calibrate the VLBI measurement error contributions is to introduce a second measurement of a nearby radio source (i.e. a Quasar) for which the position is known and differentiate the two DOR measurements. This differentiation allows to almost completely remove the error contributions from station clock offsets and instrumental delays, which are common for the two measurements. Errors from uncalibrated media and baseline orientation modelling are also reduced, to an extent which depends on the commonality of the signal path, on the time interval between the successive measurements, and on the different spectral structures for the two signals.

A typical ΔDOR campaign consists in a set of three DOR measurements taken either in Spacecraft-Quasar-Spacecraft (SQS) or Quasar-Spacecraft-Quasar (QSQ) sequence, each having a duration of a few minutes. The use of more than two measurements is needed to remove clock-epoch and clock-rate offsets by linearly interpolating the extreme measurements to the time-tag of the central measurement, which represents the time reference of the final ΔDOR product.

# 2 Tropospheric Delay Calibration System testbed using GAIA data analysis

## 2.1 Introduction

Precise radiometric tracking is of key importance during operations of interplanetary missions and for radio science applications. Most of the recent deep space missions, including Cassini, BepiColombo, and the upcoming JUICE mission, rely on a combination of X and $K_A$ band radio links to mitigate the dispersive effects of propagation through interplanetary plasma, solar corona and Earth ionosphere, leaving tropospheric delay as one of the main error contributors to Doppler and ranging errors [3].

To meet the demanding requirements of the MORE and 3GM radioscience experiments on-board the BepiColombo and JUICE missions, in terms of radiometric tracking accuracy and end-to-end frequency stability, ground-based Microwave Radiometers (MWR) are deemed as the most appropriate instruments for tropospheric delay calibration [4].

These issues were initially addressed by JPL, during the development, testing and operations of the Advanced Water Vapor Radiometers for the CASSINI Media Calibration System [5]. Later, ESA performed the ASTRA [3] and AWARDS [6] studies for the definition of the requirements for accurate spacecraft tracking and for the preliminary design of a Tropospheric Delay Calibration system (TDCS), respectively.

The TDCS system that is described here represents the prototype of a new instrument for the calibration of tropospheric delay based on a high stability and high accuracy $K_A$/V band MWR, which was developed within an ESA-ESTEC contract by a consortium of Radiometer Physics GmbH (A Rohde & Schwartz Company), University of Bologna, and the Université catholique de Louvain.

Specifically, this work focuses on the end-to-end performance characterization of the TDCS system, which was realized through a detailed OD analysis using a series of Doppler measurements for the GAIA spacecraft. It is important to clarify that the purpose of this test is not to reproduce the full OD solution of the ESOC FD team, but to validate the TDCS products by making a punctual evaluation of the relative noise reduction and improved stability performances when TDCS-based calibrations are used in place of standard GNSS-based calibrations.

## 2.2 Tropospheric Delay Calibration System

The TDCS is a combination of instruments, software tools and operational procedures that allows for an accurate estimation of the tropospheric delay and delay-rate along the s/c direction while minimizing the effect of the instrument instability. The TDCS is composed of three main subsystems:

- An ultra-stable MWR for deep-space applications: this system, which is shown in Figure 2-1, is a modified version of the standard HATPRO-G5 MWR developed by RPG [7]. This instrument measures sky noise emissions at frequencies near the water vapor absorption peak at 22.2 GHz, the oxygen absorption band around 60 GHz and in the 30 GHz window, which is sensitive to liquid water (clouds and rain). With respect to its standard counterpart, this version was tailored for s/c tracking applications by adding:
    - A 2-axes Antenna Tracking System (ATS) to gain full sky scanning capabilities.
    - An external parabolic reflector dish with a diameter of 1.2 meters. This allows to narrow the MWR half-power beamwidth (HPBW) down to 1.3°, thus reducing the effect of solar intrusions during periods of superior conjunction.

    - Air blowers and heater systems on both the MWR receiver and the parabolic dish to avoid water and ice condensation over the exposed surfaces.
    - A high precision meteo station providing values of air pressure, temperature and relative humidity at ground level.
    - A rain detector, which is used to identify periods for which collected data is affected by precipitation on the antenna system.

- <u>MWR External Control System (MWR-ECS)</u>: this system is a modified version of the standard RPG h/w and s/w platform, which is responsible for monitoring and controlling of the MWR unit and for generating all the output atmospheric products. Specifically, s/w updates include:
    - Control procedures for the new ATS.
    - Specific calibration procedures for the instrument parameters (e.g. gain, receiver noise temperature and noise diode emission).
    - Mission specific coefficients for the Neural Network (NN) retrieval algorithms (i.e. tailored for the Malargue station and for low elevation measurements). These are used to convert the measured Brightness Temperature (TB) data from the 14 $K_A$/V band channels to the final atmospheric products along the slant direction. In particular, the main output of the MWR-ECS is represented by time series of Slant Wet Delay (SWD) and Slant Hydrostatic Delay (SHD) for a radio-link propagating along the LOS direction.
- <u>Calibration, data Acquisition and Processing System (CAPS)</u>: this software tool acts as a high-level access point for monitoring and controlling of TDCS functions by the ground station Front-End Controller (FEC), representing an intermediate layer between the FEC and the MWR-ECS for improved flexibility during the prototype testing. The system, developed by the University of Bologna, is responsible for: 1) processing tracking data files from the FEC and generating topocentric tracking coordinates compatible with the ATS, 2) monitoring and controlling the MWR through real-time TCP-IP communications with the MWR-ECS, 3) processing SPD data provided by the MWR unit and generating the final CSP calibration cards that are used for orbit determination by ESOC Flight Dynamics.

Figure 2-1 TDCS prototype.

### 2.2.1 Methods for stability characterization

Long-term stability is a key driver when using tropospheric delay measurements for the calibration of Doppler observables. The system stability performance is conventionally quantified using the Allan Standard Deviation (ASD) of the relative frequency shift for one-way links. This is expressed using the so called JPL representation in (2.1), where $\tau_{tr}$ is the tropospheric path delay, $y(t) = -d\tau(t)/dt$ is the rate of change of the path delay, $\Delta T$ is the stability time interval, and the brackets $\langle\cdot\rangle$ indicate an ensemble average of the measured time series.

$$ASD_{y-1way}(\Delta T) = \frac{\sqrt{\langle[\tau_{tr}(t) - 2\cdot\tau_{tr}(t+\Delta T) + \tau_{tr}(t+2\cdot\Delta T)]^2\rangle}}{\Delta T\cdot\sqrt{2}}\,[\mathrm{s/s}] \qquad (2.1)$$

Measurements of the tropospheric delay using MWRs are affected by a series of error sources, which can be broadly divided into scene-dependent and scene-independent contributions. The former comprises all error sources whose magnitude depends on the local atmospheric conditions encountered during the measurements. These include contributions from:

- Retrieval Algorithm: depending on the observed scene (e.g. clear sky or cloud front), the retrieval algorithms used to estimate the SPD from raw TB measurements may perform with different accuracies. The magnitude of this error contribution is highly dependent on the characteristics of the retrieval algorithm. For the specific case of NN retrieval it depends on the completeness and variety of the test cases that were used to train the NN.
- Beam Mismatch: this term is related to the different air volumes observed by the MWR and the DSA during the s/c radiometric tracking. The most common causes for this discrepancy are the different shape and size of the MWR and DSN beams, the finite baseline distance between the two instruments, and pointing errors induced by the ATS.

The scene-independent contribution comprises all error sources which are related to the MWR components or to the physical modelling. These include contributions from:

- Instrumental noise: this term accounts for a) the magnitude and spectral characteristics of the noise emitted by the RF front-end of the instruments, b) the stability of the parameters for the Ka/V band receivers (i.e. gain, receiver noise figure) and of the power emitted by the noise diode used for internal calibration.
- Antenna effects: this accounts for fluctuations of the absorption coefficient for the main reflector ( caused by the hydrophobic coating) and for spill-over losses of the $K_A$-band channels over a variable background.

Most of the single contributions described above were the subject of previous investigations by the author [7] and by other institutions involved in the TDCS development [8] [9], and were numerically quantified with simulations and testing in controlled environments.

### 2.2.2 Installation and testbed campaign

After successfully passing its Factory Acceptance Review, the TDCS was shipped to Argentina and deployed at the Malargue ESTRACK complex, where it was installed in the proximity of the DS3 main antenna, as shown in Figure 2-2. The installation campaign, which lasted from the 5th to the 8th February 2019, comprised several functionality and performance tests, including a series of end-to-end tracking passes.

The final testbed campaign started on the 16th February 2019 and lasted until the end of July of the same year. A total of 44 tracking passes were collected for the GAIA s/c, which acted as main target for the testbed campaign.

This particular choice of target was mainly driven by geometric and operational considerations.

By operating constantly near solar opposition, the impact of solar plasma and ionospheric delay on both Doppler and ranging data is particularly limited for GAIA. This factor becomes particularly relevant when using a single radiometric link, which does not allow for a direct removal of these dispersive effects. Furthermore, several GAIA tracking passes were already scheduled at the DS3 complex for the same time period (mostly involving telemetry downlink and other standard operations). Additional radiometric tracking would therefore have a limited impact on ground station operations.

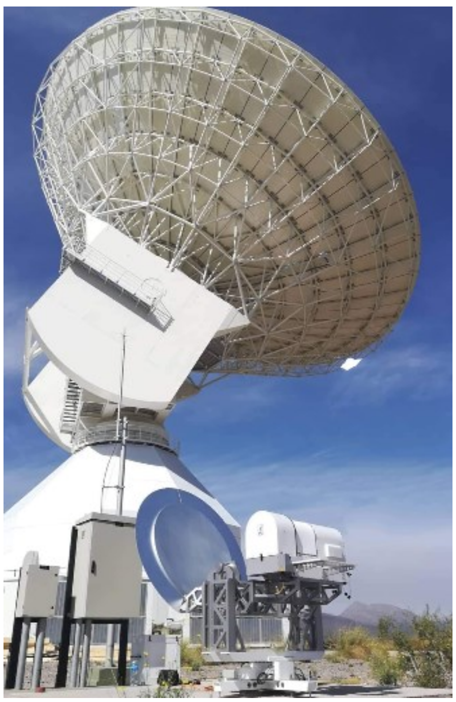

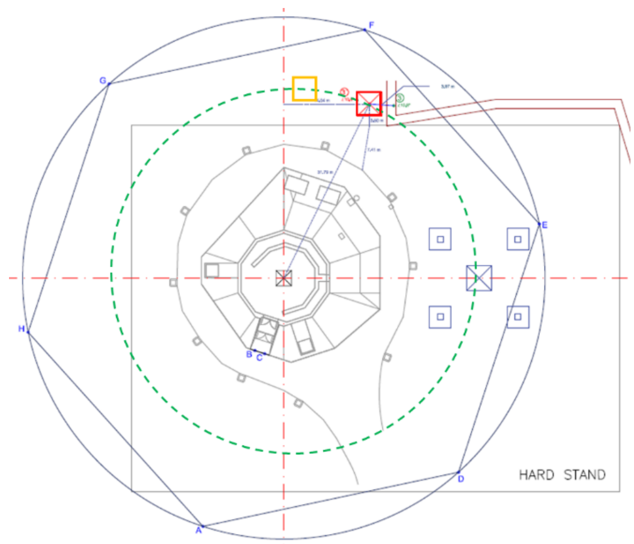


Figure 2-2 Left: TDCS operating alongside the DS3 antenna. Right: top view of the Malargue station complex with the location of the TDCS mounting platform (red square) and pre-selected location for a second TDCS (orange square)

## 2.3 The GAIA mission

### 2.3.1 Overview

GAIA is an ESA cornerstone scientific mission, whose main aim is to measure the three-dimensional position and velocity distributions of stars within the Milky Way.

Launched from Kourou onboard a Soyuz-STB rocket on 19th December 2013, the spacecraft was soon inserted into a transfer orbit towards the second Lagrange point ($L_2$), which was reached after roughly 26 days. The s/c operates from a Lissajoux-type orbit, with an orbital period of roughly 180 days. These types of orbit have several advantages with respect to Earth bound orbits when it comes to long term astrometric observations, including: stable thermal conditions, low-radiation environments, and optimal observing geometry (having the Sun, Earth and Moon always in the same direction and with almost no eclipses).

The GAIA scanning law, which is graphically depicted in Figure 2-3, was accurately designed to ensure optimal astrometric performances, and follows the general principles used in the 1990s for the Hipparcos spacecraft. This foresees two superimposed motions:

- A fixed spin rate of $\overrightarrow{\omega_S} = 60''[1/s]$ around the s/c axis of symmetry, ensuring a complete scan of the payload focal plane every 6 hours.
- A slow precession of the spin axis around the Sun direction with a period of 63 days. This particular precession period, coupled with the selected value for the solar aspect-angle of 45°, ensures that at least six distinct observations are available for each target during a single year.

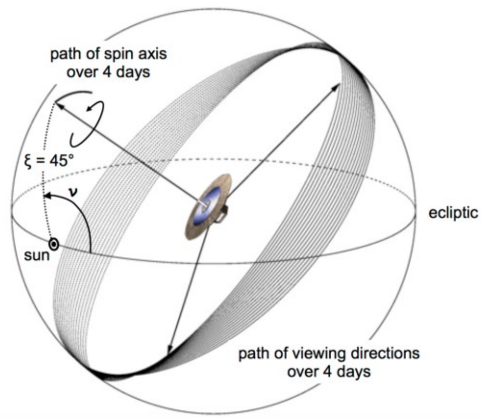


Figure 2-3 Illustration of the GAIA scanning law (Credit [10])

### 2.3.2 The GAIA spacecraft

The GAIA spacecraft is composed of:

a) A Payload Module (PM), containing the optical bench and the two main telescopes. The PM is externally covered by a thermal tent, providing insulation from the external environment and protecting the mirrors from the impact of micro-meteoroids.

b) A Service Module (SM): this comprises all mechanical, structural, and thermal elements supporting the instrument and the s/c electronics. The SM also houses the propulsion system, which comprises a set of bi-propellant NTO/MMH thrusters for orbital maneuvers and a cold-gas micro-propulsion system for attitude control.

c) A high-gain Phased Array Antenna (PAA): this antenna comprises six radiating elements and is mounted on the Sun- and Earth- directed side of the SM. Using electronic beam steering (phase shifting), the PAA allows for high-rate downlink transmissions at X-band.

d) A deployable sunshield assembly: this structure is used to block the Sun and prevent any stray light from reaching the PM. The sunlit side also houses the solar arrays for power supply.

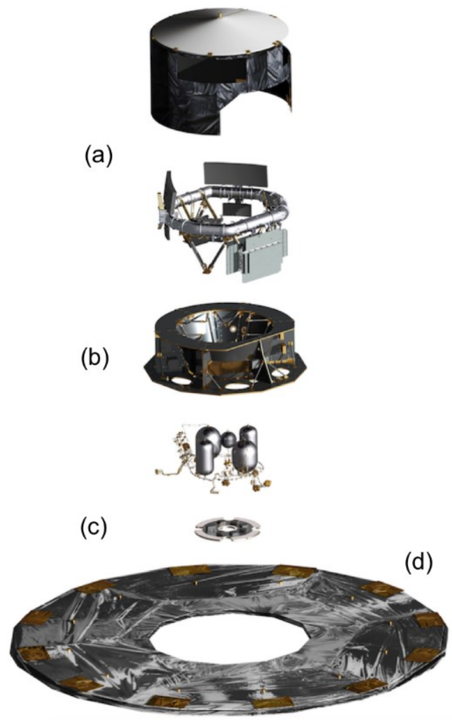


Figure 2-4 Exploded schematic view of GAIA (Credit [10])

### 2.3.3 Spacecraft model

The employed s/c model is the one shown in Figure 2-5, which represents a simplified version of Figure 2-4. Only a few elements that are relevant to the OD analysis are retained here, including: the Service Module (SM), whose base plane contains the origin of the s/c body frame, the Centre of Mass (COM) location, and the communication antennae, which are further described in Section 2.3.3.4. Additional elements such as the optical payload or the solar panels are not considered for this analysis, since no acceleration model relies on an accurate model of the s/c shape.

#### *2.3.3.1 S/C body frame*

The s/c body frame, which is used as reference for most of the non-gravitational accelerations, is defined as follows:

- The x-axis is the cross product of ASTRO1 and ASTRO2 Line-Of-Sight (LOS) directions, which represent the optical axes of the main telescopes. The x-axis is also aligned with the spin axis of the s/c but pointing in the opposite direction. As a consequence, a positive right-handed spin occurs around the $-\hat{x}$ direction.
- The z-axis lies in the plane perpendicular to the x-axis and bisecting the angle between the ASTRO1 and ASTRO2 LOS directions.
- The y-axis completes the orthogonal right-handed reference frame.

The origin of the s/c body frame lies in the separation plane between the launcher adapter and the satellite, which also represents the s/c center of symmetry.

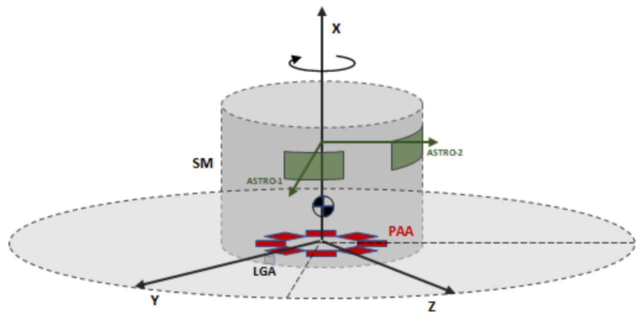

Figure 2-5 Simplified s/c model for the OD analysis

#### 2.3.3.2 S/C mass and COM location

The s/c mass is considered as constant throughout each OD arc, corresponding to a single tracking pass. This constant value is changed only in response to major Orbit Trim Maneuvers (OTMs), as shown in Table 2-1, where the total wet mass is expressed as a function of the Day Of the Year (DOY) for 2019.

Table 2-1 S/C mass as a function of the DOY

| DOY | Mass [kg] | Comment |
|---|---|---|
| 47 – 58 | 1844.752 | Initial wet mass |
| 62 – 113 | 1844.319 | Following OTM01 |
| 115 – 197 | 1843.420 | Following OTM02 |
| 199 | 1832.263 | Following OTM11 |

The s/c COM coordinates are defined in Table 2-2. Since their medium-term variation is considered to be smaller than the uncertainty in their computation, we consider these coordinates as fixed.

By definition the MONTE OD s/w assumes the s/c body frame to have its centre at the COM location for the target body. To compensate for this effect, a trajectory offset is defined from the actual COM to the internal MONTE reference, with equal magnitude and opposite sign with respect to the coordinates in Table 2-2.

#### 2.3.3.3 S/C attitude and a-priori state

The s/c attitude is taken from the online Tool for Auxiliary Scientific Calculations (TASC) from ESOC FD [11]. This tool provides time series of quaternions defining the rotation from the Earth Mean Equator of J2000 frame (EME2000) to the s/c body frame, and corresponding values for the s/c angular rate about the body frame. These discrete rotation data points are imported in MONTE using built-in functions. Whenever the s/c attitude is required at a given time, which is not explicitly included in the input timeseries, a linear interpolation scheme is used to retrieve it.

The a-priori s/c state is taken again from the online TASC tool, which was used to generate a time series of GAIA state vectors with respect to the Solar System barycenter in the EME2000 reference frame. This dataset covers the whole testbed window from February to August 2019 with a time-step of 10 minutes. The discrete state vectors are imported in MONTE using built in functions that employ a 3$^{rd}$ order Lagrange fitting scheme. These a-priori states were used as initial guess in the filter setup and to compute the a-priori values of position dependent parameters such as the SRP normalization scale factor.

#### 2.3.3.4 S/C antennae

GAIA uses separate antennae for up-link and down-link at X-band, namely a Low Gain Antenna (LGA) and a Phased Array Antenna (PAA), respectively. The physical coordinates of the PAA and of the LGA, expressed in s/c body frame, are given in Table 2-2.

Table 2-2 Coordinates of key components in the s/c body frame

| **Target** | $\vec{x}_{S/C}\ [m]$ |
|---|---|
| PAA | [-0.119, 0.0, 0.0] |
| LGA | [-0.0405, 1.55, -0.3] |
| COM | [1.0521, -0.0212, 0.0181] |

For the purpose of the OD estimation, more relevant than the physical coordinates are those of the antenna phase centre, which may vary over time depending on the operating mode and on the s/c attitude. The phase centre of the PAA is moving along its axis of symmetry, which coincides with the rotation axis of the spacecraft. An analytical model for the variation of the phase centre location for the PAA is not available, so its coordinates were estimated as part of the OD process.

A limitation imposed by using the MONTE OD s/w is the inability to separate the up-link and down-link antennae for two-way or three-way links. A workaround to overcome this issue is to define a virtual antenna, located along the LGA-PAA segment, and to estimate its coordinates within the filter, using as a-priori value the midpoint between the PAA and the LGA. A value of 10 cm is used for the a-priori uncertainty of the virtual antenna coordinates (see Table 2-8), which are treated as local parameters and estimated separately for each arc. This a-priori uncertainty is consistent with the estimated values of the phase center offset for the virtual antenna coordinates in the single arcs, which are shown in Figure 2-6.

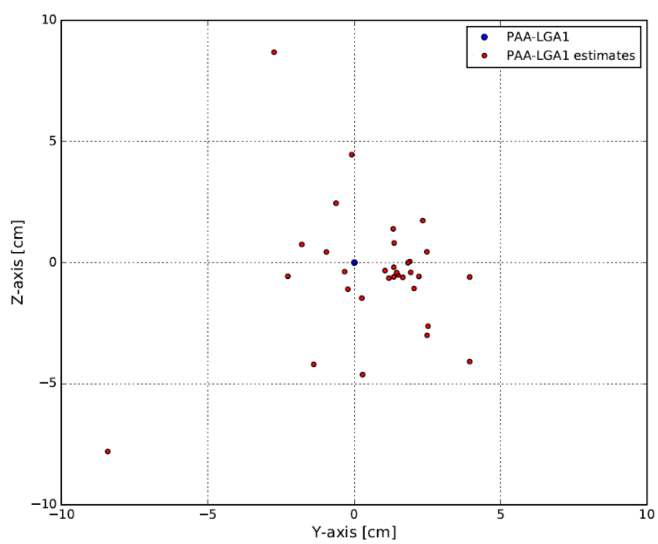


Figure 2-6 Estimated values for the location of the virtual antenna phase center

## 2.4 Dynamical model

The overall goal of the OD analysis described in this study was to validate the TDCS products by performing a direct comparison between the OD performances obtained using TDCS and the ones obtained using GNSS-based calibrations. Keeping this in mind, the dynamical model was kept reasonably simple, to reduce the likelihood of possible biases in the results caused by mismodelling errors. The selected approach, which mostly relies on tabulated data and a-priori information from ESOC FD, also allows for easier replicability of the analysis for further validation.

### 2.4.1 Gravitational accelerations

The gravitational accelerations that were considered for this analysis include point-mass gravity from the Sun, the planets and their satellites, the Moon, and Pluto. Higher order gravitational harmonics are neglected. State vectors and gravitational parameters for the Solar System bodies are taken from JPL's DE430 planetary ephemerides [12].

### 2.4.2 Non-gravitational accelerations

Non-Gravitational Accelerations (NGA) were mostly introduced in the form of polynomial functions using tabulated coefficients. Each NGA was validated by integrating the s/c trajectory and comparing the residuals of the integrated state with the reference a-priori solution from ESOC FD. Introduction of a new NGA model should progressively reduce the s/c state residuals.

#### *2.4.2.1 Solar and thermal radiation pressure*

Instantaneous accelerations from Solar Radiation Pressure (SRP) and Thermal Radiation Pressure (TRP) were provided in form of an ASCII text file, along with instantaneous values for the s/c mass. The acceleration components, normalized at 1 AU, were provided in a reference frame defined as follows:

- The x-axis is the s/c to Sun direction
- The y-axis is the projection of the ecliptic north pole onto the plane perpendicular to the x-axis.
- The z-axis completes the orthogonal right-handed reference frame.

The instantaneous acceleration values were provided in blocks of contiguous data, which were implemented in MONTE using a Lagrange fitting scheme of order 9 (or of the highest degree allowed by the number of available points). A multiplicative scaling factor for de-normalization was computed according to (2.2), where $R_{S/C}$ is the s/c heliocentric distance at the mid-time of the corresponding block.

$$SF = \left(\frac{1AU}{R_{s/c}}\right)^2 \tag{2.2}$$

#### *2.4.2.2 Micro-propulsion system*

Attitude control on GAIA is performed using a cold-gas Micro-Propulsion System (MPS), which causes parasitic accelerations to act permanently on the s/c. Instantaneous accelerations from cold-gas MPS thrusters, expressed in the s/c body frame, were provided in form of an ASCII text file.

These values are separated into blocks of contiguous data, for which a Lagrange fitting scheme of order 3 is applied (or of the highest degree allowed by the number of available points).

### 2.4.3 Maneuvers

#### *2.4.3.1 Orbit Trim Maneuvers*

Throughout the GAIA testbed campaign, three main Orbit Trim Maneuvers (OTMs) were performed: two station keeping OTMs, respectively in February and April 2019, and an inclination change maneuver, split into 9 burns, in July 2019. All these OTMs were modelled as impulsive burns and estimated in the filter.

Table 2-3 shows the a-priori $\Delta\vec{V}$ values for the main OTMs, which were provided in form of ASCII text files. The reference burn times were taken at the midpoint of the tabulated start and end times, while the mass variation was applied only at the end of the single impulsive burns. Of the 11 total OTMs that were performed during the testbed campaign, only the ones occurring during the tracking passes in Table 2-9 were considered here.

Table 2-3 A-priori values for the maneuvers ΔV in the EME2000 reference frame

| **Maneuver** | **Reference epoch** | **A-priori $\overrightarrow{\Delta V}$ [cm/s]** |
|---|---|---|
| OTM1 | 27/02/2019 H 07:37:23 ET | [34.820, 12.156, 11.895] |
| OTM2 | 24/04/2019 H 12:16:32 ET | [-10.102, -17.686, -2.468] |
| OTM3 | 16/07/2019 H 09:00:48 ET | [-39.528, 16.085, -152.824] |

#### *2.4.3.2 Maneuver parasitic ΔV*

Attitude control during chemically propelled maneuvers is performed using the Reaction Control System (RCS), which causes parasitic $\Delta Vs$ to be imparted on the s/c. RCS firings are modelled as impulsive burns and estimated within the filter, using a-priori $\Delta V$ values provided by ESOC FD in form of ASCII text files and expressed in the EME2000 reference frame.

### 2.4.4 Dynamical model validation

To check the validity of the dynamical model described above, the s/c trajectory was integrated at each arc and compared with the a-priori solution for ESOC FD. As example, Figure 2-7 shows the position and velocity differences between the two trajectories for DOY 180. We can observe that throughout the course of the 10 hour long tracking pass, the position residual remains below a 4 m value, while the velocity residual is below 0.3 mm/s.

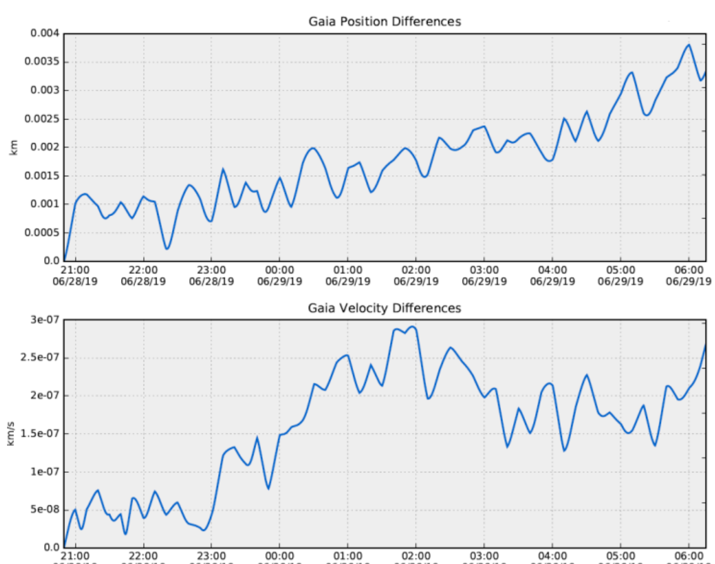


Figure 2-7 Position and velocity differences between a-priori and integrated trajectories for DOY 180

## 2.5 Data selection and pre-processing

### 2.5.1 Data summary

Raw Doppler measurements for the testbed campaign were provided in TTCP format following the naming convention in [13]. As a first step, Doppler data files were converted to Binary Object Archive (BOA) format, which is compatible with MONTE OD s/w and merged to single files covering the different tracking passes. Then, a series of data editing routines were performed as part of the pre-processing activities to include relevant a-priori information on the measurements or to calibrate known error sources.

All the definitions for the Doppler observables and the algorithms for data processing, which are not explicitly described in the following sections, can be found on chapter 13 of [2].

### 2.5.2 S/C delays

Raw measurements are edited to introduce the s/c transponder phase and group delays, which affect the Doppler and ranging measurements, respectively. The reference values for these parameters are displayed in Table 2-4. Path delays from or to the antennas due to other onboard electronic components are currently not available.

Table 2-4 S/C transponder delays

| | |
|---|---|
| Phase delay $[s]$ | $1.5009 \cdot 10^{-3}$ |
| Group delay $[s]$ | $1.0867 \cdot 10^{-5}$ |

### 2.5.3 The Marini effect

Since GAIA is a spinning s/c, an additional correction must be applied to remove the Doppler-shift induced by the s/c rotation over circularly polarized signals. According to [14], the Doppler error introduced for a coherent two-way tracking link is approximately expressed as in (2.3), where $s_\uparrow$ and $s_\downarrow$ represent the signs of the frequency shift on the up-link and down-link signals, $M_2$ is the s/c transponder ratio, $\lambda_\uparrow = c/\nu_\uparrow$ is the wavelength of the transmitted frequency, $\overrightarrow{\omega_S}$ is the s/c angular velocity, and $\hat{r}_{GS}$ is the LOS direction to the Earth ground station.

$$\Delta f_{Marini} \cong (s_\uparrow + \frac{s_\downarrow}{M_2}) \frac{\lambda_\uparrow (\overrightarrow{\omega_S} \cdot \hat{r}_{GS})}{2\pi} \tag{2.3}$$

The sign of the frequency shift depends upon the sign of the spin rate with respect to the one of the signal polarization. The magnitude of the induced Doppler shift will be maximum when the transmitted and received signals have the same polarization signs, which is the case for GAIA s/c, having Right-Handed Circularly Polarized (RHCP) signals for both up-link and down-link transmissions.

An order of magnitude estimation of the Doppler correction to be applied is computed in (2.4), where the characteristic rotation rate of $\omega_S = 60\ arcsec/s$ (used for GAIA scientific observations) was employed, and considering values of $\lambda_\uparrow^X \cong 3.56\ cm$ and $M_2 = 880\ /\ 749$ for transmission at X-band.

$$\Delta f_{MAX} \cong \left(1 + \frac{749}{880}\right) \cdot \frac{3.56 \cdot 10^{-2}\ [m] \cdot 2.91 \cdot 10^{-4} [rad/s]}{2\pi} \cong 3\mu m/s \tag{2.4}$$

It can be seen from (2.4) that the expected error is almost negligible when compared to the other main error sources described in Section 2.5.4. Nonetheless, an accurate calibration of this effect was performed at each tracking pass, using the s/c attitude information and instantaneous rotation rates derived from the TASC tool information.

### 2.5.4 Media calibrations

#### *2.5.4.1 Solar Plasma*

For most of the recent deep space missions, the dispersive effect from the charged particles in the solar corona is calibrated using a multi-frequency link with coherent up-link and down-link [3]. This was not possible for the current analysis, since GAIA uses a single frequency link at X-band. However, the effect of Solar plasma is assumed to be small, considering that s/c is near solar opposition, with SEP values always below 170°. For this reason, no solar plasma correction was applied.

#### *2.5.4.2 Ionospheric delay*

Most of the recent radioscience analyses have used standard GNSS products, in the form of CSP cards, for ionospheric calibrations. However, these data products are not routinely generated by ESOC FD, which relies on the Jakowsky model [15] to estimate the Doppler and ranging errors during the OD process. The same model was used for this analysis to generate a time series of corrections for the scheduled passes.

Being GAIA only visible at night, the ionospheric induced Doppler error at X-band was expected to be small when compared to the variations of tropospheric delay, as confirmed by the computed values, which were often below the $10\ \mu m/s$ resolution of the Jakowsky model. After adding the computed calibrations to a series of selected tracking passes, no appreciable improvement was seen in the post-fit residuals. On this basis, it was decided not to include the ionospheric calibrations within the final OD analysis.

### 2.5.5 Count-time variations

Depending on the explored cases, different count times were used for the Doppler measurements. Since the raw TTCP measurement files have a default count time of $\tau_c = 1\ s$, this latter was increased using built-in MONTE routines. To preserve data quality in the presence of measurement discontinuities and to avoid border effects around the beginning and the end of the tracking arcs, tight restrictions were imposed for the data reduction. This means that to compress a series of Doppler observables from an initial count time $\tau_{C0} = 1\ s$ to a new count time of $\tau_{C1} = 60\ s$, all 60 data points within the interval $[t_{ref} - \tau_{C1}/2\ ,\ t_{ref} + \tau_{C1}/2]$, where $t_{ref}$ is the reference time-tag, should be available. If this is not the case, all data points within the interval are discarded.

### 2.5.6 Data reduction

The first filter iterations were used to perform a manual inspection of the Doppler residuals, highlighting the presence of signatures or discontinuities within the dataset. After this process, a series of automatic reduction procedures were performed, including:

- Removing Doppler observables around chemically propelled maneuvers to avoid discontinuities. Specifically, all observables falling within an interval $t_{man} \pm \tau_C/2$ from the maneuver (including both OTMs and RCS firings), where $t_{man}$ is the maneuver execution time, and $\tau_c$ is the Doppler count time, were removed.
- Removing the observables that were collected below a $15°$ elevation threshold, where the accuracy of the radiometric retrieval is progressively degraded. This is due to the fact that simulations used for determining the retrieval coefficients are done assuming a longitudinally homogeneous atmosphere. This assumption is valid at high elevation angles but at low angles the emission can come from parts of the atmosphere far from the MWR with very different atmospheric conditions. In addition, below 20º there is an increased amount of contamination due to ground and clutter emission. Considering that radiometric products below 10° are always discarded, this additional elevation threshold was

deemed as a reasonable) compromise between the production of larger data-sets and the reliability of the estimated tropospheric calibrations.

- Performing an automated removal of the outliers through the following iterative process:
    1. Mean value $\mu_i$ and standard deviation $\sigma_i$ of the valid post-fit Doppler residuals are computed at each arc for the current iteration.
    2. For each observable, the maximum allowable deviation is computed according to (2.5), where $N = 6$ is the selected scale factor and $\varepsilon$ is a small correction factor. The + and - sign in (2.5) are used respectively for observables that were discarded (outliers) or valid at the previous iteration (to avoid Hysteresis). All residuals lying outside the interval $[\mu_i \pm \Delta D_{max,i}]$ are removed.
    3. The first two steps are repeated until the current iteration produces no additional outliers or the maximum number of iterations is reached

$$\Delta D_{max,i} = N\sigma_i(1 \pm \varepsilon) \tag{2.5}$$

### 2.5.7 Data weights

Initial a-priori Doppler weights were computed using noise models developed in the framework of the ASTRA study [3]. After a first iteration, refined measurement weights for each tracking pass were computed as the mean RMS value of the post-fit residuals for that pass, corresponding to a single arc for the filter estimation. This 2-step process was repeated for each of the cases explored in Section 2.9. Depending on the applied calibrations and on the measurement pre-processing procedures, these cases may in fact present different outliers and characteristic noise values.

## 2.6 TDCS data processing

The main product of TDCS is represented by time series of tropospheric excess path length along the Zenith direction, provided using the conventional format of CSP cards, according to the definitions in [16].

Starting from the raw Brightness Temperature (TB) measurements collected by the MWR unit, the MWR External s/w generates a time-series of Slant Path Delay (SPD) measurements according to the retrieval algorithms defined in [9]. These are transmitted via TCP-IP to the CAPS s/w for additional processing and generation of the CSP cards. This section describes all the relevant processing procedures, some of which were applied to all datasets, while others were applied selectively as a part of the comparison between the different OD solutions.

### 2.6.1 Tropospheric wet delay

For the current analysis, SWD data was estimated using either the standard RPG Hatpro-G5 binary products, when available, or CAPS-generated binary products for the remaining cases (see Table 2-9 and Table 2-10). Data products generated internally by RPG's Hatpro-G5 s/w were preferred since they generally present slightly higher sampling frequencies with respect to their CAPS-generated counterparts, which were limited by the speed of real-time TCP-IP communications during operations. However, s/w issues encountered during the testbed campaign caused occasional data losses, forcing to rely on CAPS datasets for a few passes.

The following processing procedures were applied, in this order, to the input SWD data:

1. <u>Mapping</u>: SWD was mapped to Zenith using a simple sine function $ZWD = SWD \cdot \sin(E)$, where $E$ represents the instantaneous elevation value, in radians, as indicated by the ATS. Although more

complex mapping functions are available (e.g. the Niell mapping function [17]), this selection was made in order to be consistent with the procedures used by RPG during the NN retrieval training.

2. Automatic removal of the outliers: this is performed using a z-score technique to evaluate the deviation of each data point from a smoothed dataset, which is generated using a median filter with an adjustable time window. All data points showing a z-score higher than a given threshold are substituted by the corresponding filtered values. This process was fine-tuned by a visual inspection of the data, leading to the selection of the filter parameters shown in Table 2-5.

Table 2-5 Median filter settings

| Parameter | Value |
|---|---|
| Z-score threshold ($Z_{MAX}$) | $6$ |
| Filter time window ($\Delta T$) | $100\ s$ |

3. The integration time of the ZWD time series is increased from the original sampling rate of roughly 1s to 20 s to improve the signal-to-noise ratio. This is done, according to the definitions given in [17], by sorting the original data points in intervals of fixed length and averaging the measured values (provided that a sufficient number of points is available to be statistically representative).

4. The conventional reference value of ZWD at the Malargue complex is provided in [18] and reported in Table 2-6. This value is subtracted from the ZWD measured with the TDCS to obtain an instantaneous delay deviation $\delta ZWD = ZWD - ZWD_{ref}$.

Table 2-6 Reference delay values at the DS3 complex in Malargue

| Parameter | Value [m] |
|---|---|
| $ZWD_{ref}$ | $0.0527$ |
| $ZHD_{ref}$ | $1.9184$ |

5. CSP cards are generated from the $\delta ZWD$ time series using linear piecewise fit between consecutive data samples and according to the format described in [16].

It should be mentioned that no reliable scaling technique was available to map the measured ZWD data from the TDCS height to the DSN reference height. The same applies for GNSS based calibrations, which are referred to the height of the ground station receiver.

### 2.6.2 Selection of the ZWD integration time

To evaluate the influence of the ZWD integration time on the OD results, a sensitivity analysis was performed by generating several CSP calibration cards using different integration times at $\tau = [2, 10, 20, 30, 60]\ s$, and comparing the ASD curves for the corresponding post-fit residuals. To decouple this evaluation from the hydrostatic component of the tropospheric delay, only constant reference values for the ZHD calibrations were applied.

A comparison of the ASD curves for Doppler post-fit residuals is shown in Figure 2-8 for the arc corresponding to the 18th of July 2019. This particular tracking pass was selected since the effect induced by variations in the ZWD integration time is particularly pronounced.

Increasing the integration time is expected to improve the radiometric resolution by reducing the effect of gaussian thermal noise. However fast variations of atmospheric signals can be lost at longer integration times, in particular in the presence of clouds. This behavior is clearly reflected in Figure 2-8, where we observe that the ASD curve using a $2\ s$ integration time is significantly higher than the others at low stability intervals. Conversely, the ASD curve corresponding to $60\ s$ integration is higher than the others at intermediate stability intervals, where some of the underlying atmospheric variability is lost during the integration process.

The results presented in Figure 2-8 are consistent with the ones obtained for the remaining tracking arcs, albeit with some minor performance differences depending on the amount and properties of the atmospheric variability at each day. As a result, a single representative value of $\tau = 20\ s$ was selected to be used for the following analysis.

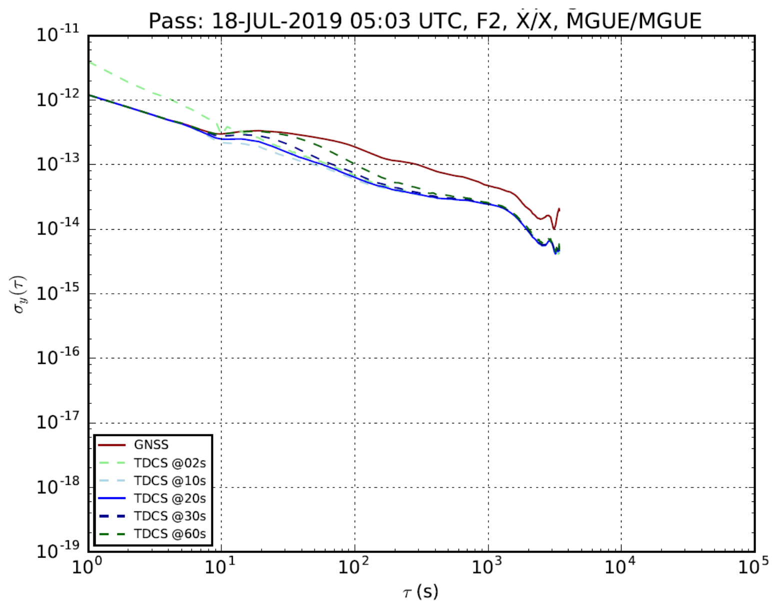

Figure 2-8 ASD comparison of post-fit residuals, using ZWD calibrations at different integration times.

### 2.6.3 Tropospheric Hydrostatic Delay

The ZHD was computed using the Saastamoinen model [19], from pressure and temperature readings coming from the following input sources:

- DSA meteo station: this data, which comes from the meteo station within the Malargue DS3 complex, was provided in form of TTCP files according to the definitions in [20], and using a sampling interval of 60 seconds.
- MWR meteo sensor: this data, which comes from the embedded sensors within the Hatpro-G5 MWR unit, was provided in form of either binary or ASCII file, according to the definitions in [21], and using a sampling interval of 1 second.

The following processing procedures were applied, in order, to the input meteorological data:

1. Local ZHD values were computed with Saastamoinen at the selected meteorological station, whose coordinates are given in Table 2-7. This could correspond to either the TDCS or the DSA meteo station, depending on data availability, as indicated in Table 2-9.
2. A corrective factor $\Delta ZHD$ was applied, to map the local ZHD values to the height of the DSA phase centre, according to (2.6), where $\Delta h$ is the height difference in meters between the meteo station and

the DSA phase center, and $P_{avg}$ and $T_{avg}$ are respectively the average pressure in mbar and the average temperature in kelvin at the meteo station. Since vertical profiles for pressure and temperature are not known, a reasonable approximation to (2.6) is given by substituting $P_{avg}$ and $T_{avg}$ with the corresponding instantaneous measurements provided by the meteo station.

$$\Delta ZHD \cong -0.0000776 \cdot \Delta h \left(\frac{P_{avg}}{T_{avg}}\right) \tag{2.6}$$

3. The reference value of ZHD at the Malargue complex, which is given in Table 2-6, is subtracted from the measured ZHD to obtain an instantaneous delay deviation $\delta ZHD = ZHD - ZHD_{ref}$.
4. The time series of $\delta ZHD$ values is smoothed using a gaussian filter with a 10 minute time window. The need for this additional processing step is evident when looking at Figure 2-9, which shows the ZHD time series for DOY 104. The limited resolution of data generated by the TDCS pressure sensor causes discontinuities between successive data points, which have an order of magnitude comparable with characteristic values for the short-term variability of the ZWD data. Using the raw values with no smoothing may therefore result in an increased Doppler noise when using hydrostatic delay calibrations.
5. CSP cards are generated from smoothed $\delta ZHD$ time series using linear piecewise fit between consecutive data points and according to the format described in [16].

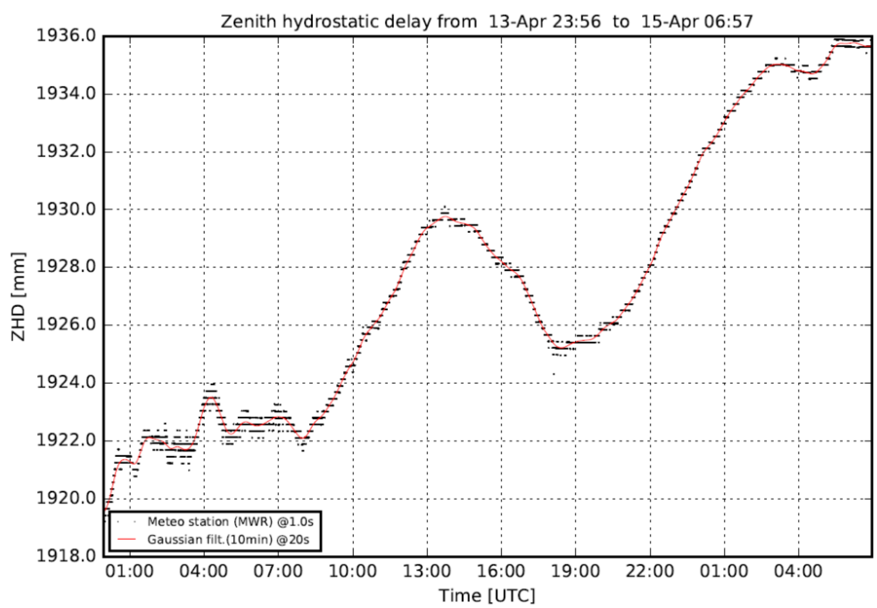


Figure 2-9 Raw ZHD measurements (black dots) and their corresponding filtered values (red line) for DOY 104.

Table 2-7 Mean Sea Level (MSL) altitude of the ground support equipment

| Instrument | MSL altitude [m] |
|---|---|
| TDCS | $h_{MWR} = 1552$ |
| DSA meteo station | $h_{DSA} = 1553$ |
| DSA phase center | $h_{ATS} = 1571.5$ |

## 2.7 Filter setup

Table 2-8 summarizes the solved-for parameters within the Sequential Root Information (SRI) batch filter and their associated a-priori uncertainties. A-priori values for the s/c state were taken from the online TASC tool [11], which were imported in MONTE using a Lagrange interpolating scheme (see Section 2.3.3.3).

Table 2-8 Estimated parameters within the OD filter and associated a-priori uncertainties

| Parameter | $N_{est}$ | A-priori σ | Notes |
|---|---|---|---|
| S/C position | 3 | $100\ km$ | Estimated locally within the single arcs. A-priori values are taken from the TASC tool [11]. |
| S/C velocity | 3 | $1\ m/s$ | |
| PAA phase center | 2 | $10\ cm$ | A-priori values are given in Table 2-2. The estimated coordinates are actually referred to the virtual antenna between the PAA (down-link) and the LGA (up-link). |
| OTMs $\Delta\vec{v}$ | $3 \cdot N_{OTM}$ | $10^{-1}\ m/s$ | A-priori values are given in Table 2-3. |
| RCS parasitic $\Delta\vec{v}$ | $3 \cdot N_{RCS}$ | $10^{-2}\ m/s$ | A-priori values are provided by ESCO FD |

It should be noted that the estimated coordinates for the PAA phase center are actually referred to the virtual antenna described in Section 2.3.3.4. Furthermore, only the y and z components of the antenna location are estimated. Being the x-axis of the body frame lying along the s/c spin direction, this coordinate is in fact not observable using Doppler measurements.

## 2.8 Testbed summary and data availability

Two successive testbed campaigns were conducted at DS3 in Malargue between February and July 2019, targeting a total of 44 tracking passes, out of which 32 were successfully analyzed.

Both hardware and software updates were performed through the course of these campaigns, in response to the test results or any issue that was addressed during the testing phase. As a result, availability of data products may vary between the different tracking passes.

Table 2-9 and Table 2-10 detail the schedule and output product availability for each of the tracking passes, where the following conventions are used:

- The 1st, 2nd, and 3rd columns indicate respectively the tracking pass ID number and its corresponding date and day of the year (DOY). Pass IDs labelled in grey represent tracking passes that were discarded due to the unavailability of key datasets required for the analysis. Pass IDs labelled in light blue indicate the ones that were selected for further evaluation in the following sections.
- The 4th and 5th columns represent the start and end times for the tracking passes. These correspond to the first and last time-tags of the raw Doppler measurements collected by ESOC, which do not coincide, in general, with the start and end times of the single arcs within the OD estimation. The simultaneous availability of all the key data products (Doppler data, GNSS-based calibrations, and TDCS-based calibrations) is in fact required for the performance analysis, so shorter arcs may be used depending on data availability. It should be noted that passes for which the observation start time corresponds to the previous day with respect to the one reported in the 2nd column, are marked with an (*) sign.
- The 6th, 7th, 8th, and 9th columns indicate the availability of TTCP Doppler data, TDCS-based tropospheric calibrations, meteorological data (either from the GS or the TDCS meteo station), and GNSS-based tropospheric calibrations. For each data type, dark green cells indicate full coverage over the tracking interval, while light green cells indicate a partial coverage. In particular, TDCS-based

calibrations were derived using either binary (*DLY*) files generated by the MWR-Host system (labelled as *Hatpro*) or binary (*L2*) data files generated by the CAPS system (labelled as *CAPS*). The selection of input files between these two sources was uniquely dictated by data availability (some of the *DLY* binary files were lost due to s/w issues), with the main difference consisting in slightly lower sampling times for the *L2* data files.

Table 2-11 summarizes the atmospheric conditions encountered during the subset of tracking passes that were eventually included in the OD analysis. In particular, the following convention was used:

- Similarly to Table 2-9, the 1st, 2nd, and 3rd columns indicate the tracking pass ID number and its corresponding date and DOY.
- The 4th column indicates the time interval covered by the OD arc corresponding to the tracking pass.
- The 5th and 6th columns indicate respectively the number of valid and ignored Doppler observables within the filter, at 60 seconds count time. Specifically, ignored observables account for both data reduction due to unavailability of complementary data products and for the processing procedures described in Section 2.5.6.
- The 7th column indicates whether the Rain Flag (RF) of the TDCS meteo station was triggered during the tracking pass.
- The 8th column contains the maximum Liquid Water Path (LWP) values estimated from TDCS radiometric measurements during the pass.
- The 9th column provides the range of ZWD values retrieved during the pass.
- The 10th column indicates the maximum wind speed measured by the TDCS meteo station. This can be considered as a proxy parameter for the presence of turbulent eddies in the atmosphere.
- The 11th and 12th columns report characteristic integrated values for the wind speed and the turbulence parameter $C_N^2$ derived from the ECMWF database [22] at the coordinates of the DS3 complex. Both wind intensity and turbulence strength are derived by averaging over time the vertical profiles in the ECMWF database that fall within the interval of valid observables (when available). The vertical profiles so obtained are then spatially averaged from ground level to a height of 1 km above the surface to obtain the characteristic values shown in Table 2-11.

Table 2-9 Schedule and data availability for the tracking passes of the first testbed campaign

| ID | Date | DOY | Start | End | Doppler | DLY data | Meteo | TropCal | Notes |
|---|---|---|---|---|---|---|---|---|---|
| **1** | 16/02/19 | 47 | 02:03:41 | 06:25:00 | OK | Hatpro | GS | OK | TDCS data available from 02:00 to 03:30 |
| **2** | 17/02/19 | 48 | 02:03:01 | 09:08:00 | OK | CAPS | GS | OK | TDCS data available from 02:00 to 03:32 |
| **3** | 21/02/19 | 52 | 02:00:24 | 09:27:05 | NO | CAPS | GS | NO | |
| **4** | 23/02/19 | 54 | 01:59:00 | 09:28:00 | OK | CAPS | GS | OK | TDCS data available from 02:28 to 03:38 |
| **5** | 24/02/19 | 55 | 01:58:18 | 09:30:00 | OK | CAPS | GS | OK | TDCS data available from 00:29 to 03:34 |
| **6** | 25/02/19 | 56 | 01:14:27 | 09:41:39 | OK | Hatpro | GS | OK | TDCS data available from 08:13 to 10:54 |
| **7** | 26/02/19 | 57 | 01:45:23 | 09:45:09 | OK | Hatpro | GS | OK | TDCS data available from 08:06 to 16:54 |
| **8** | 27/02/19 | 58 | 01:08:54 | 08:18:21 | OK | Hatpro | GS | OK | TDCS data available from 00:32 to 03:35.<br>OTM1 within the tracking pass. |
| **9** | 28/02/19 | 59 | 01:06:09 | 06:52:42 | NO | Hatpro | GS | NO | TDCS data available from 00:32 to 03:36 |
| **10** | 03/03/19 | 62 | 00:33:31 | 09:35:33 | OK | CAPS | GS | OK | TDCS data available from 00:32 to 03:40.<br>New version of Host-s/w was installed on 01/03/19 (9.23.2). |

Table 2-10 Schedule and data availability for the tracking passes of the second testbed campaign

| ID | Date | DOY | Start | End | Doppler | DLY data | Meteo | TropCal | Notes |
|---|---|---|---|---|---|---|---|---|---|
| **11** | 09/04/19 | 99 | 01:59:59 | 11:06:56 | OK | Hatpro | GS | OK | New version of Host-s/w was installed on 26/03/19 (9.25.1) |
| **12** | 10/04/19 | 100 | 00:07:06 | 11:07:06 | OK | Hatpro | GS | OK | |
| **13** | 11/04/19 | 101 | 01:37:47 | 11:07:14 | OK | Hatpro | GS | OK | |
| **14** | 12/04/19 | 102 | 00:07:20 | 11:07:20 | OK | Hatpro | GS | OK | At the end of the passage, TDCS elevation got stuck at 18° |
| **15** | 13/04/19 | 103 | 00:07:25 | 11:07:25 | OK | NO | GS | NO | |
| **16** | 14/04/19 | 104 | 01:39:13 | 11:07:29 | OK | Hatpro | GS | OK | |
| **17** | 16/04/19 | 106 | 01:07:24 | 08:39:09 | OK | Hatpro | GS | OK | |
| **18** | 17/04/19 | 107 | 01:40:33 | 08:32:38 | OK | Hatpro | GS | OK | Anomaly in MPS table accel |
| **19** | 18/04/19 | 108 | 23:48:14* | 10:28:48 | OK | Hatpro | GS | OK | Anomaly in MPS table accel |
| **20** | 19/04/19 | 109 | 23:46:07* | 09:37:40 | OK | Hatpro | GS | OK | |
| **21** | 20/04/19 | 110 | 23:43:58* | 09:18:36 | OK | Hatpro | GS | OK | |
| **22** | 21/04/19 | 111 | 23:41:47* | 08:23:29 | OK | Hatpro | GS | OK | |
| **23** | 22/04/19 | 112 | 23:39:34* | 07:31:58 | OK | Hatpro | GS | OK | |
| **24** | 23/04/19 | 113 | 00:52:18 | 08:31:50 | OK | Hatpro | GS | OK | |
| **25** | 25/04/19 | 115 | 23:32:38* | 06:57:55 | OK | NO | GS | NO | |
| **26** | 29/04/19 | 119 | 23:22:42* | 07:37:23 | OK | Hatpro | GS | OK | New version of CAPS s/w was installed on 26/04/19 (2.2) |

| ID | Date | DOY | Start | End | Doppler | DLY data | Meteo | TropCal | Notes |
|---|---|---|---|---|---|---|---|---|---|
| **27** | 30/04/19 | 120 | 00:45:00 | 05:57:00 | OK | Hatpro | GS | NO | No GNSS tropospheric calibrations available. Reference values are used |
| **28** | 01/05/19 | 121 | 23:17:27* | 04:59:16 | OK | Hatpro | GS | NO | |
| **29** | 04/05/19 | 124 | 23:09:16* | 04:43:24 | OK | Hatpro | GS | OK | TDCS data available from 03:04 to 04:43 |
| **30** | 11/05/19 | 131 | 22:49:39* | 06:11:39 | OK | CAPS | GS | OK | TDCS data available from 22:49 to 03:14 |
| **31** | 12/05/19 | 132 | 22:46:53* | 06:16:06 | OK | NO | GS | NO | |
| **32** | 18/05/19 | 138 | 22:30:49* | 05:43:22 | OK | NO | GS | NO | |
| **33** | 19/05/19 | 139 | 22:28:12* | 05:57:54 | OK | Hatpro | GS | OK | TDCS data available from 22:27 to 05:57 |
| **34** | 26/05/19 | 146 | 22:09:59* | 09:09:57 | OK | NO | GS | OK | Tracking pass not consistent with GAIA (discarded) |
| **35** | 14/06/19 | 165 | - | - | NO | NO | NO | NO | |
| **36** | 20/06/19 | 171 | - | - | NO | NO | NO | NO | |
| **37** | 29/06/19 | 180 | 21:09:50* | 05:41:34 | OK | Hatpro | GS | OK | |
| **38** | 30/06/19 | 181 | 21:09:16* | 06:02:56 | OK | CAPS | GS | OK | |
| **39** | 11/07/19 | 192 | 22:30:29* | 09:01:07 | OK | Hatpro | GS | OK | TDCS data available from 06:41 to 10:20 |
| **40** | 12/07/19 | 193 | 22:56:36* | 09:02:08 | NO | Hatpro | Hatpro | OK | Elevation gets stuck at 15° |
| **41** | 13/07/19 | 194 | 22:28:28* | 09:03:16 | NO | NO | NO | NO | |
| **42** | 15/07/19 | 196 | 21:46:56* | 08:02:56 | NO | NO | NO | NO | |
| **43** | 16/07/19 | 197 | 23:56:22* | 09:07:22 | OK | Hatpro | GS | OK | TDCS data available from 05:54 to 10:08<br>OTM1 within the tracking pass |
| **44** | 18/07/19 | 199 | 00:43:37 | 09:10:18 | OK | Hatpro | GS | OK | TDCS data available from 07:13 to 09:46 |

Table 2-11 Summary of data availability and main meteorological parameters affecting the OD results

| ID | Date | DOY | Observables From/to ≈ | Valid | Ignored | RF | $LWP$ $[g/m^2]$ | $ZWD$ $[mm]$ | $ws_{MWR}$ $[km/h]$ | $ws_{ECMWF}$ $[km/h]$ | $C_N^2$ $[m^{-2/3}]$ |
|---|---|---|---|---|---|---|---|---|---|---|---|
| **1** | 16/02/19 | 47 | [02:00, 03:30] | 82 | 174 | NO | <100 | [99, 104] | <10 | - | - |
| **2** | 17/02/19 | 48 | [02:00, 03:30] | 85 | 334 | NO | <200 | [132, 155] | <14 | - | - |
| **4** | 23/02/19 | 54 | [02:00, 03:30] | 94 | 349 | NO | <100 | [132, 155] | <10 | - | - |
| **5** | 24/02/19 | 55 | [02:00, 03:30] | 91 | 355 | NO | 0 | [24, 32] | <25 | - | - |
| **6** | 25/02/19 | 56 | [08:00, 09:30] | 76 | 426 | NO | <100 | [54, 62] | <15 | - | - |
| **7** | 26/02/19 | 57 | [08:00, 09:30] | 87 | 387 | NO | <100 | [43, 49] | <8 | - | - |
| **8** | 27/02/19 | 58 | [01:00, 03:30] | 141 | 283 | YES | 0 | [69, 84] | <10 | - | - |
| **10** | 03/03/19 | 62 | [01:30, 03:30] | 105 | 379 | NO | 0 | [73, 87] | <8 | - | - |
| **11** | 09/04/19 | 99 | [02:00, 11:00] | 531 | 10 | NO | <100 | [45, 65] | <15 | 9.86 | $5.34 \cdot 10^{-14}$ |

| ID | Date | DOY | Observables From/to ≈ | Valid | Ignored | RF | $LWP$ $[g/m^2]$ | $ZWD$ $[mm]$ | $ws_{MWR}$ $[km/h]$ | $ws_{ECMWF}$ $[km/h]$ | $C_N^2$ $[m^{-2/3}]$ |
|---|---|---|---|---|---|---|---|---|---|---|---|
| **12** | 10/04/19 | 100 | [00:00, 11:00] | 597 | 16 | YES | <100 | [58, 77] | <30 | 19.75 | $5.75 \cdot 10^{-14}$ |
| **13** | 11/04/19 | 101 | [02:00, 11:00] | 554 | 10 | NO | <100 | [47, 70] | <6 | 29.11 | $4.14 \cdot 10^{-14}$ |
| **14** | 12/04/19 | 102 | [00:00, 10:00] | 587 | 67 | NO | <100 | [38, 70] | <10 | 18.53 | $1.27 \cdot 10^{-13}$ |
| **16** | 14/04/19 | 104 | [02:00, 11:00] | 543 | 19 | NO | <200 | [13, 25] | <40 | 42.61 | $7.83 \cdot 10^{-14}$ |
| **17** | 16/04/19 | 106 | [01:00, 08:30] | 446 | 0 | NO | <100 | [50, 67] | <10 | 20.27 | $1.60 \cdot 10^{-13}$ |
| **18** | 17/04/19 | 107 | [02:00, 08:30] | 399 | 3 | NO | 0 | [27, 45] | <16 | 23.16 | $4.90 \cdot 10^{-14}$ |
| **19** | 18/04/19 | 108 | [00:00, 10:30] | 627 | 8 | NO | <100 | [54, 72] | <9 | 22.49 | $7.82 \cdot 10^{-14}$ |
| **20** | 19/04/19 | 109 | [00:00, 10:00] | 578 | 8 | NO | <400 | [62, 105] | <25 | 16.87 | $9.19 \cdot 10^{-14}$ |
| **21** | 20/04/19 | 110 | [00:00, 09:30] | 561 | 8 | YES | <2000 | [90, 170] | <9 | 16.34 | $4.83 \cdot 10^{-14}$ |
| **22** | 21/04/19 | 111 | [00:00, 08:30] | 506 | 10 | NO | <100 | [60, 73] | <9 | 17.79 | $8.73 \cdot 10^{-14}$ |
| **23** | 22/04/19 | 112 | [00:00, 07:30] | 459 | 8 | NO | <100 | [64, 75] | <9 | 20.91 | $5.66 \cdot 10^{-14}$ |
| **24** | 23/04/19 | 113 | [01:00, 08:30] | 454 | 0 | NO | <100 | [74, 96] | <8 | 5.37 | $1.40 \cdot 10^{-14}$ |
| **26** | 29/04/19 | 119 | [23:30, 07:30] | 481 | 8 | NO | <200 | [49, 98] | <15 | 28.16 | $9.18 \cdot 10^{-14}$ |
| **27** | 30/04/19 | 120 | [01:00, 06:00] | 306 | 0 | NO | <500 | [68, 86] | <8 | 16.24 | $6.22 \cdot 10^{-14}$ |
| **28** | 01/05/19 | 121 | [23:30, 05:00] | 326 | 10 | NO | <200 | [26, 61] | <15 | 24.77 | $1.35 \cdot 10^{-13}$ |
| **29** | 04/05/19 | 124 | [23:30, 05:00] | 321 | 8 | NO | <1200 | [100, 128] | <12 | 15.61 | $3.02 \cdot 10^{-14}$ |
| **30** | 11/05/19 | 131 | [23:00, 03:00] | 250 | 176 | NO | <200 | [32, 47] | <9 | 15.21 | $7.77 \cdot 10^{-14}$ |
| **33** | 19/05/19 | 139 | [23:00, 06:00] | 434 | 0 | NO | <200 | [54, 72] | <8 | 15.31 | $7.65 \cdot 10^{-14}$ |
| **37** | 29/06/19 | 180 | [21:30, 05:30] | 496 | 0 | NO | 0 | [54, 71] | <13 | 26.73 | $6.65 \cdot 10^{-14}$ |
| **38** | 30/06/19 | 181 | [21:30, 06:00] | 518 | 0 | NO | 0 | [23, 55] | <25 | 33.08 | $6.02 \cdot 10^{-14}$ |
| **39** | 11/07/19 | 192 | [06:30, 09:00] | 138 | 477 | NO | 0 | [24, 38] | <13 | - | - |
| **43** | 16/07/19 | 197 | [06:00, 09:00] | 111 | 424 | NO | 0 | [41, 46] | <14 | 18.36 | $1.19 \cdot 10^{-13}$ |
| **44** | 18/07/19 | 199 | [07:00, 09:00] | 115 | 376 | NO | 0 | [44, 74] | <25 | - | - |

## 2.9 Results

In the following sections, 6 of the 32 tracking passes that were analyzed within the OD filter will be characterized in greater detail. These represent passes of particular relevance in terms of TDCS performance characterization, since they correspond to specific atmospheric and operating conditions that may be encountered during nominal operations at the DS3 Malargue site. For each of these arcs, a side by side comparison of the filter performances, obtained when using either GNSS-based or TDCS-based tropospheric calibrations, will be produced. Specifically, filter performances will be evaluated through the following procedure:

- <u>Visual inspection of the Doppler post-fit residuals</u>: this process is essential to highlight the presence of major signatures within the data and to identify possible causes for these features.
- <u>Comparison of the ASD values as a function of the stability interval</u>. As pointed out in Section 2.1, the most critical performance requirement for MWRs is represented by the frequency stability of the calibrated Doppler signals. Therefore, comparison of the ASD curves provides a good indication of the overall quality of the tropospheric calibrations. By comparing the measured ASD values with the characteristic white noise curve (straight line with a -1/2 slope stemming from the same point at $\tau_S = 1$ stability interval) it is also possible to estimate the amount of uncalibrated atmospheric instability.
- <u>Comparison of the power spectra at characteristic frequencies</u>. Power spectra are useful to address the main contributors to the energy distribution of the Doppler residuals, and to identify eventual features, which might not be clearly noticeable from a visual inspection of the residuals. Specifically, the power spectra shown in the next sections are realized employing a Multi-Taper Spectral Estimation (MTSE), which uses a value of $NW = 5$ as time half-bandwidth parameter to reduce the variance by averaging the individual tapered spectrograms. This technique allows to obtain much clearer spectra (less noisy) at high/mid frequencies, with respect to single spectrograms, at the expense of sensitivity in the lowest part of the frequency spectrum.

### 2.9.1 Analysis of the selected cases

#### *2.9.1.1 DOY 54 (February 23rd)*

This arc was selected mostly as a representative case for the first February campaign session.

Due to technical issues with the ATS, data availability for this campaign was limited to the first couple of hours of each tracking pass (mostly having low elevation pointing), as indicated by the low number of measurements in Figure 2-10 and Figure 2-11. No relevant signatures can be observed within the data, with an appreciable noise reduction of roughly 45% when using TDCS-based calibrations in place of GNSS-based calibrations during the OD process.

Figure 2-12 shows a comparison of the ASD of the post-fit residuals as a function of the stability interval. It can be seen that both curves follow a characteristic white noise slope up to $\tau_S = 10\ s$ where they start to depart due to uncalibrated atmospheric scintillation. Most of the residual atmospheric instability is captured by the TDCS-based calibrations, showing consistently lower ASD values at all stability intervals. It should also be noted that the ASD becomes less statistically significant for large values of $\tau_S$ due to the reduces number of sampled data points.

Similar considerations can be drawn from the power spectra in Figure 2-13, where we observe that the atmospheric instability that is effectively calibrated by TDCS is mostly related to characteristic frequencies between $10^{-2}$ and $10^{-3}$ Hz, as expected.

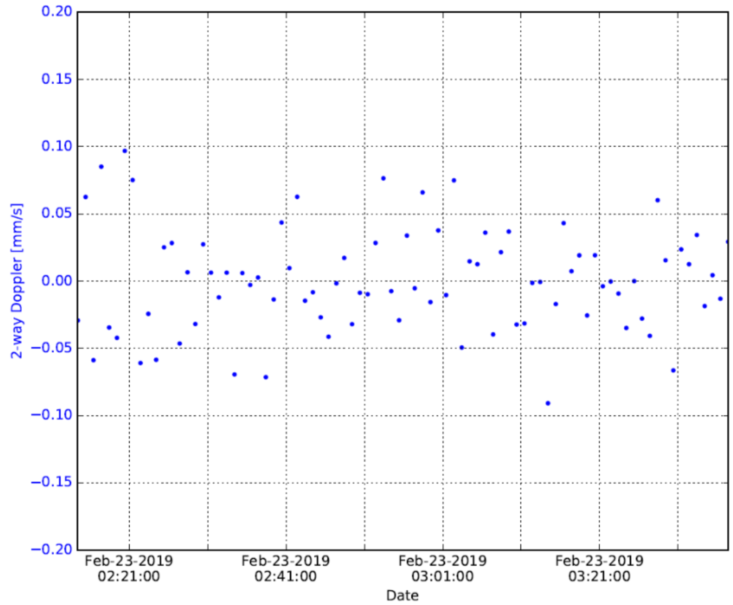


Figure 2-10 Postfit residuals for DOY 54 using GNSS-based calibrations. RMS: 3.85E-2 mm/s.

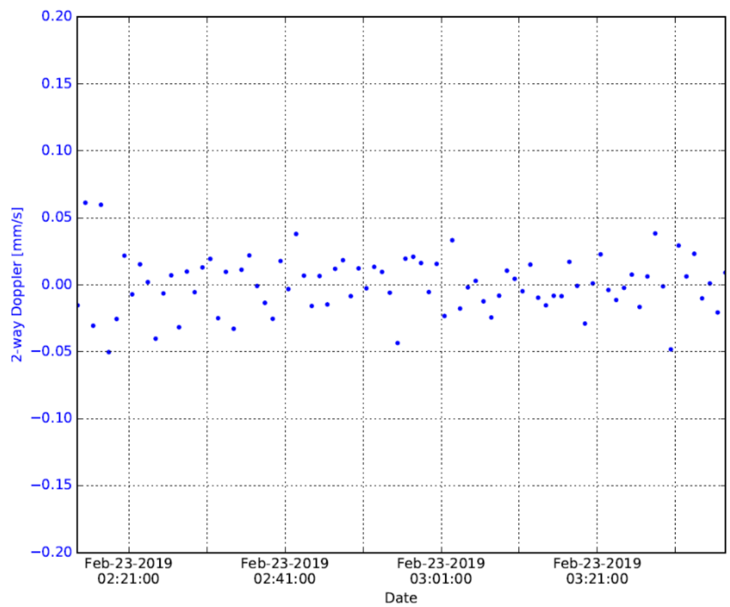


Figure 2-11 Postfit residuals for DOY 54 using TDCS-based calibrations. RMS: 2.11E-2 mm/s.

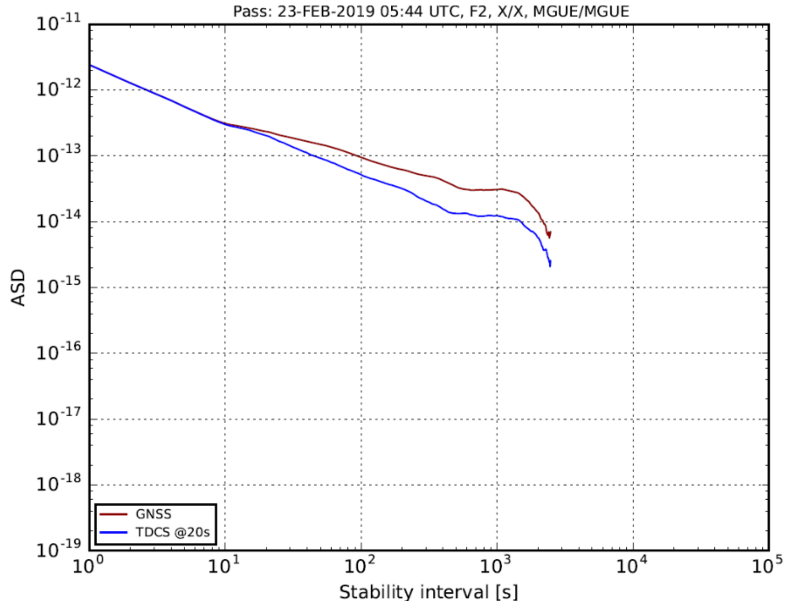


Figure 2-12 ASD of postfit residuals at DOY 54 using GNSS-based and TDCS-based calibrations.

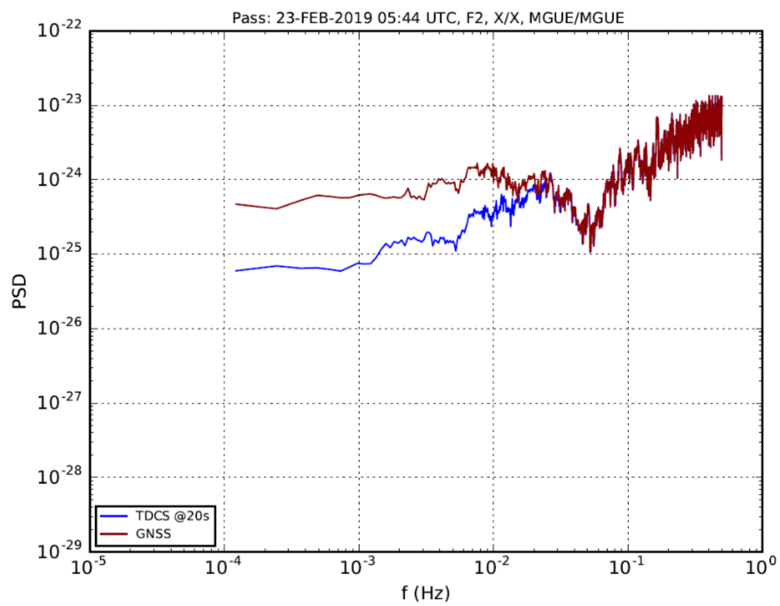


Figure 2-13 Multi-taper PSD of postfit residuals at DOY 54 using GNSS-based and TDCS-based calibrations.

#### *2.9.1.2 DOY 104 (April 14th)*

This arc was selected as representative of high wind conditions, which are often encountered at the DS3 complex in Malargue. High wind-speed values were recorded both by ground level measurements using the TDCS meteo station and high altitude measurements from the ECMWF dataset, as indicated respectively by the $ws_{MWR}$ and $ws_{ECMWF}$ parameters in Table 2-11.

By comparing Figure 2-14 and Figure 2-15, a relative noise reduction of roughly 31% is observed, with no apparent signature within the residuals.

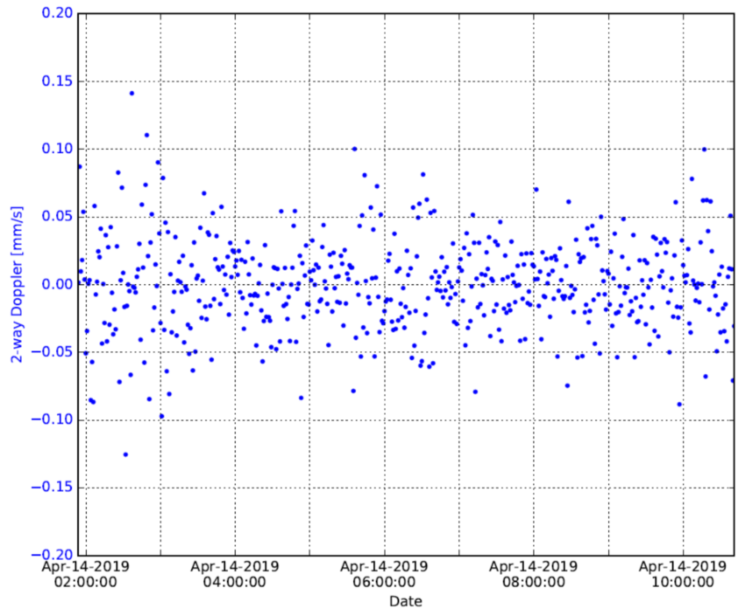


Figure 2-14 Postfit residuals for DOY 104 using GNSS-based calibrations. RMS: 3.36E-2 mm/s.

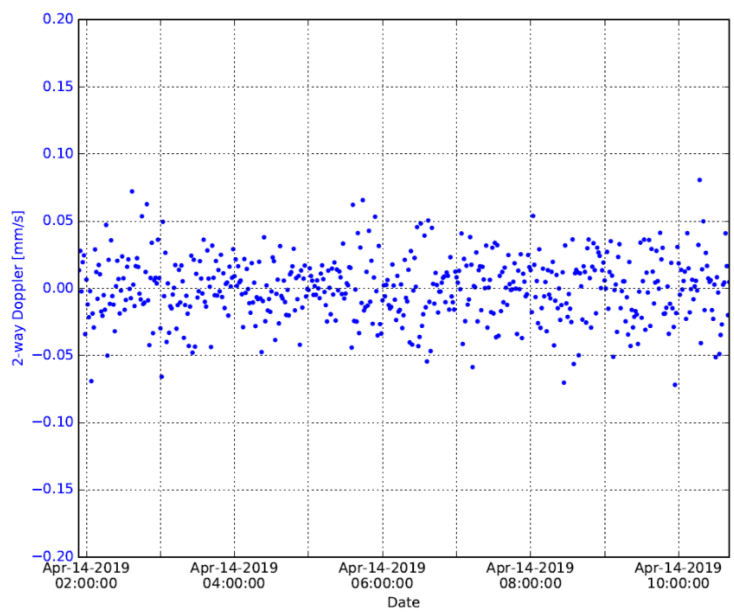


Figure 2-15 Postfit residuals for DOY 104 using TDCS-based calibrations. RMS: 2.32E-2 mm/s.

By looking at Figure 2-16, we can observed that the reduction of the ASD curve, when using TDCS-based calibrations, is less pronounced in this case with respect to the previous one. The same trend can be observed in Figure 2-17 for the power spectra, where we see that most of the noise reduction due to the TDCS-based calibrations is concentrated at characteristic time scales between the $[10^{-2}, 10^{-3}]\ s$ interval. It is difficult to pinpoint an exact cause for this reduction in performance. High wind speeds, in particular when acting along the DSA-TDCS baseline direction, might be responsible for an increased residual atmospheric instability due to the different air volumes observed by the ground station and the TDCS. Another possible explanation could be the reduced signal to noise ratio of the measured atmospheric variations, considering the low ZWD values observed throughout the pass (see Table 2-11). This effect, combined with induced vibrations on the large antenna reflector and ATS mounting structure, may cause the tropospheric noise to become negligible with respect to the other error sources.

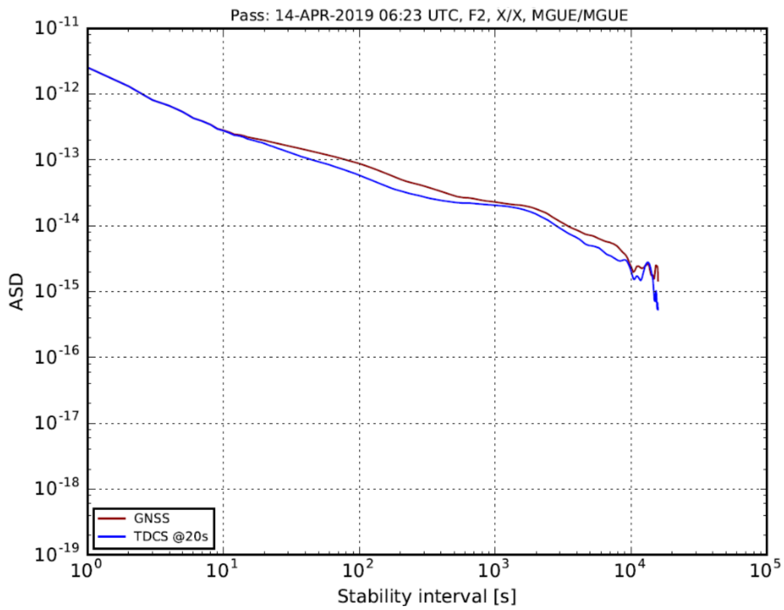


Figure 2-16 ASD of postfit residuals at DOY 104 using GNSS-based and TDCS-based calibrations.

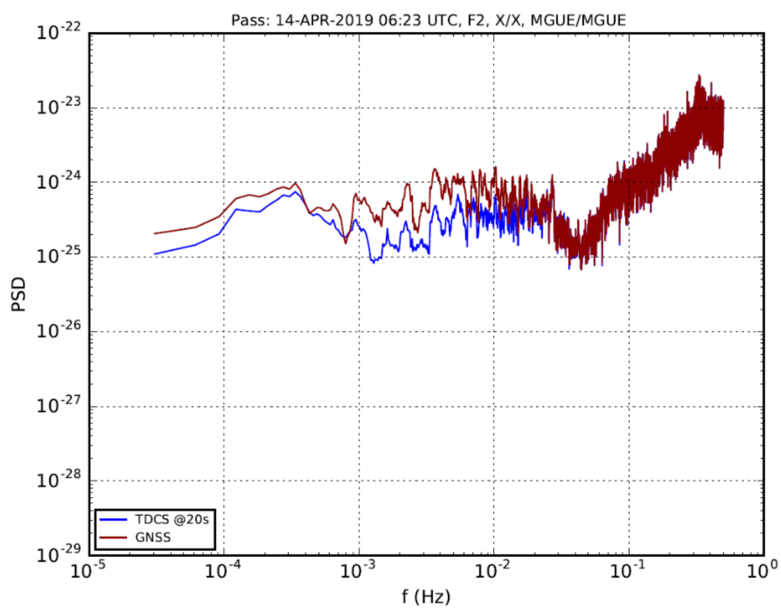


Figure 2-17 Multi-taper PSD of postfit residuals at DOY 104 using GNSS-based and TDCS-based calibrations.

#### *2.9.1.3 DOY 110 (April 20th)*

This arc was selected as representative of cloudy and rainy conditions. It can be seen from Table 2-11 that the rain flag was active during the session, with high peak values for the LWP and continuously high values for the ZWD.

This is reflected in both Figure 2-18 and Figure 2-19, which show higher noise values and several signatures within the data. Still, a noise reduction of roughly 46% is seen between the TDCS-based and the GNSS-based estimation, indicating the effectiveness of the NN retrieval training in dealing with cloudy or rainy conditions within the observed atmospheric scene. As a by-product of the overall noise reduction, additional outliers are flagged by the automatic outlier procedure described in Section 2.5.6 and thus removed from the statistics.

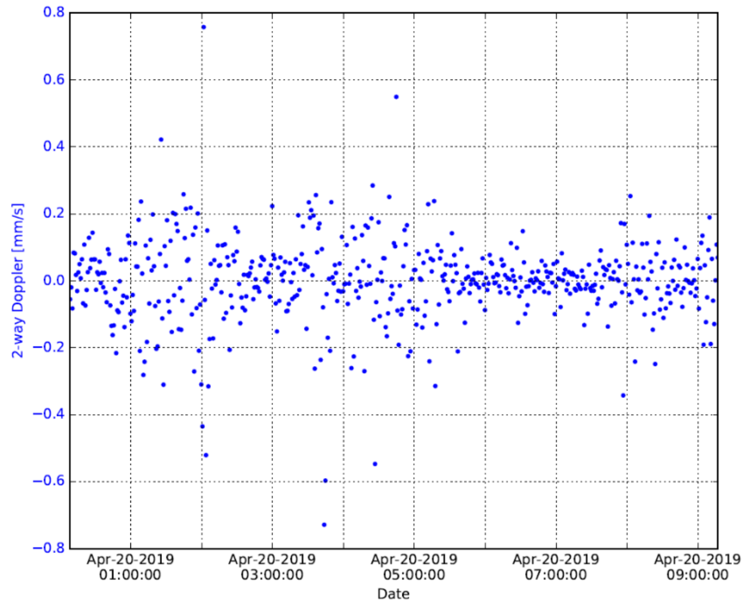


Figure 2-18 Postfit residuals for DOY 110 using GNSS-based calibrations. RMS: 1.23E-1 mm/s

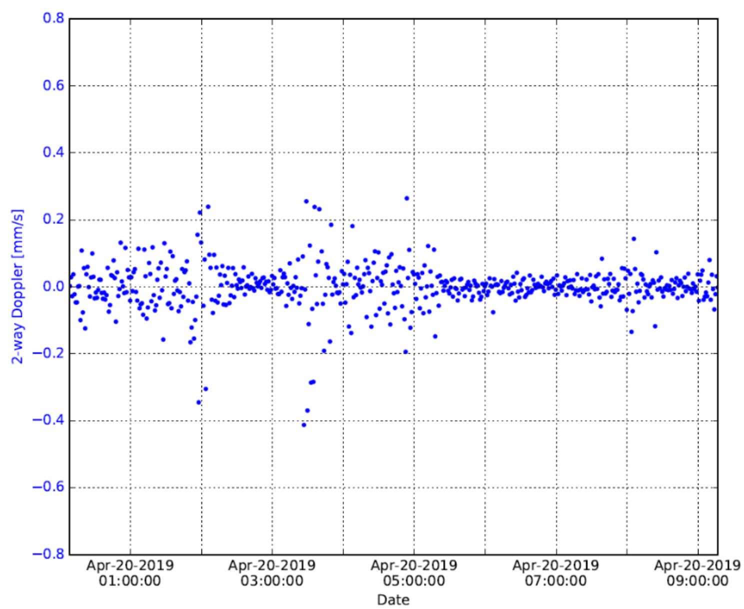


Figure 2-19 Postfit residuals for DOY 110 using TDCS-based calibrations. RMS: 6.62E-2 mm/s

The presence of adverse atmospheric conditions is reflected by the steepest departure of the uncalibrated ASD curve from a white noise slope, as seen in Figure 2-20. This is even more evident when looking at the power spectra in Figure 2-21, where we can see that the characteristic low-frequency plateau between $[10^{-4}, 10^{-2}]\ Hz$ is one order of magnitude higher than the corresponding values for the previous arcs, indicating a higher atmospheric instability at these frequencies. We can see from both these plots, that a significant portion of the underlying atmospheric instability is not calibrated by the TDCS, as expected by the highly variable atmospheric scene. However, residuals obtained with TDCS-based calibrations are still consistently better than GNSS-based ones at all time scales.

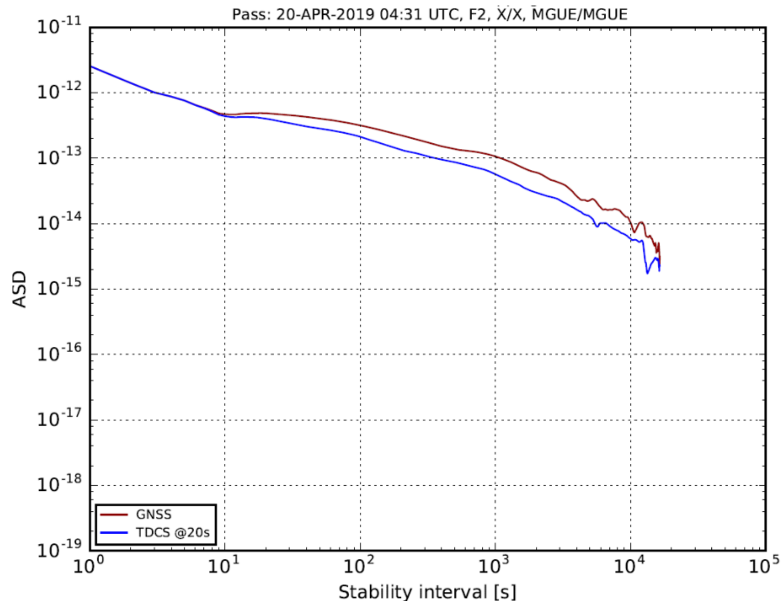


Figure 2-20 ASD of postfit residuals at DOY 110 using GNSS-based and TDCS-based calibrations.

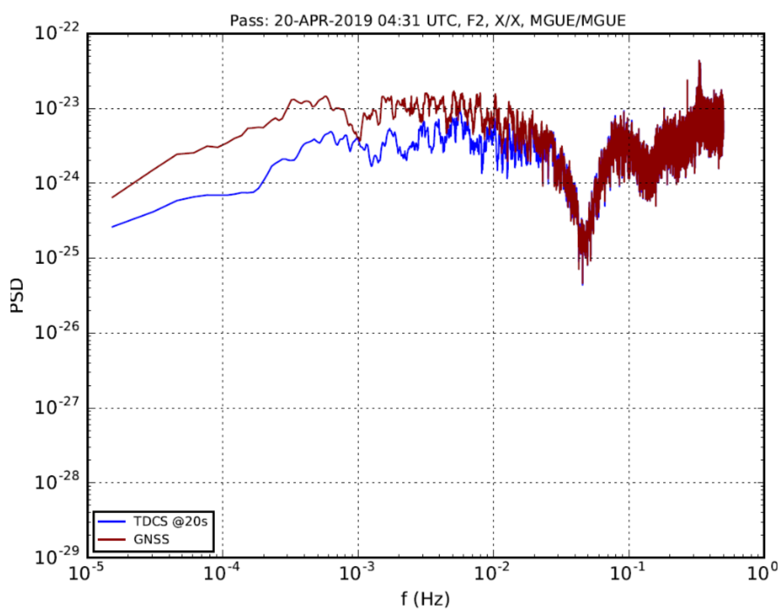


Figure 2-21 Multi-taper PSD of postfit residuals at DOY 110 using GNSS-based and TDCS-based calibrations.

#### *2.9.1.4 DOY 124 (May 4th)*

In terms of atmospheric conditions, this arc represents an optimal test case, having moderate to high values for the LWP and ZWD, but no rain and limited wind speed. This is reflected in the postfit residuals of Figure 2-23, which show no appreciable signature and produce a noise reduction of roughly 58% with respect to the residuals in Figure 2-22.

Similarly to DOY 110, the ASD plot in Figure 2-24 and the power spectra in Figure 2-25 indicate a pronounced atmospheric instability. However, in this case, TDCS-based calibrations are able to capture most of the atmospheric features at characteristic time scales between $10^{-2}$ and $10^{-4}$ seconds.

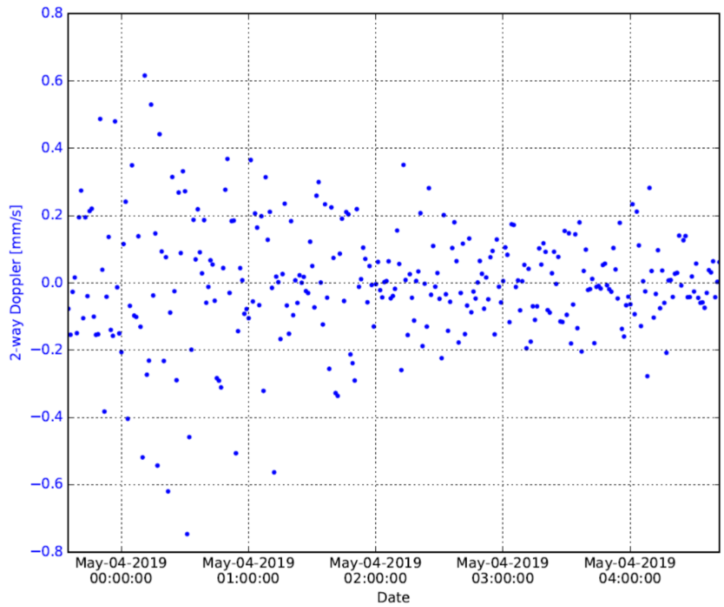


Figure 2-22 Postfit residuals for DOY 124 using GNSS-based calibrations. RMS: 1.78E-1 mm/s

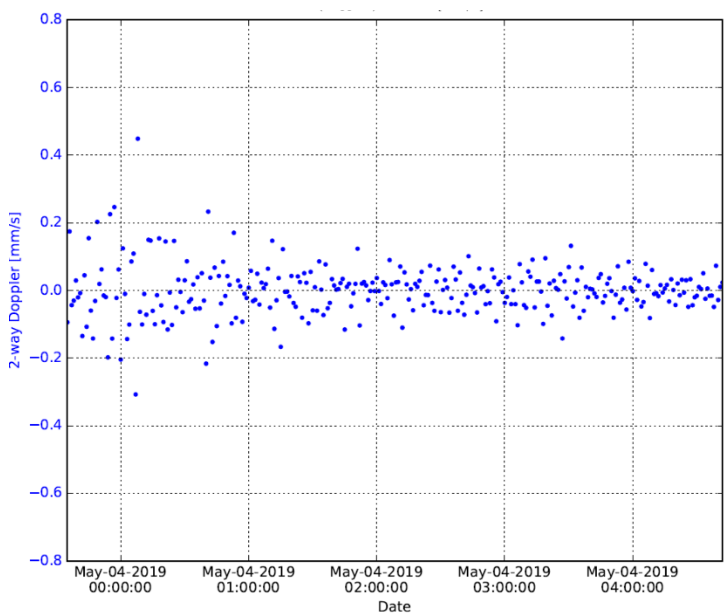


Figure 2-23 Postfit residuals for DOY 124 using TDCS-based calibrations. RMS: 7.49E-2 mm/s

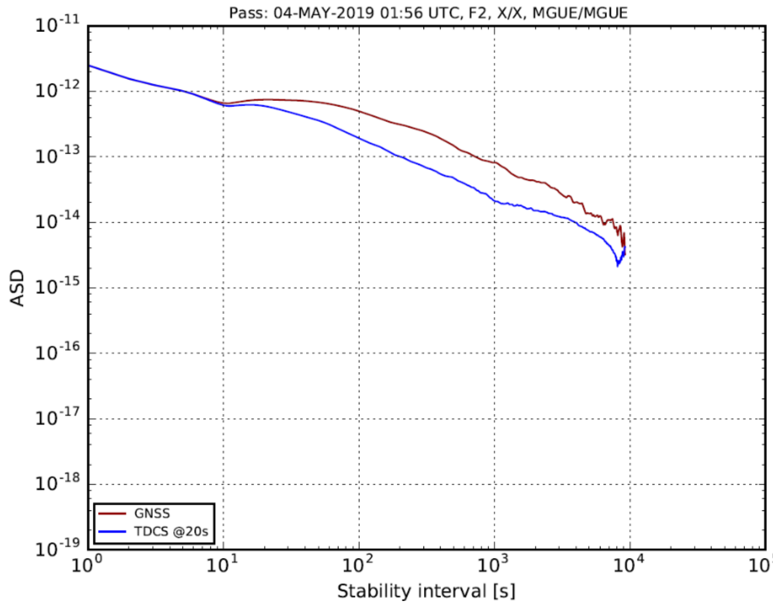


Figure 2-24 ASD of postfit residuals at DOY 124 using GNSS-based and TDCS-based calibrations.

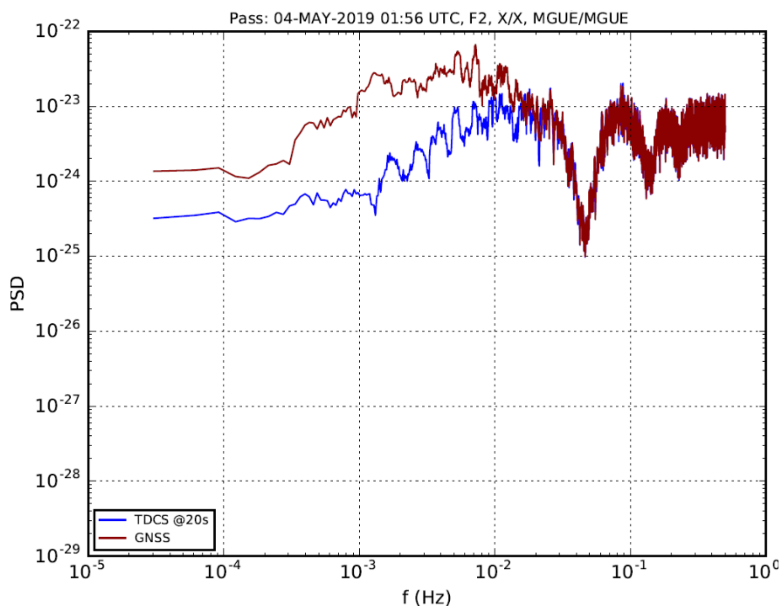


Figure 2-25 Multi-taper PSD of postfit residuals at DOY 124 using GNSS-based and TDCS-based calibrations.

#### *2.9.1.5 DOY 180 (June 29th)*

From the point of view of the atmospheric conditions, this arc represents a standard case, having moderate estimated values for the ZWD and wind speed as indicated in Table 2-11. However, it is worth reporting since it represents the first tracking session after a long hiatus between May and June 2019.

A significant noise reduction of roughly 50% is observed between the GNSS-based estimation in Figure 2-26 and the TDCS-based one in Figure 2-27, with most of the improvements occurring during the first half of the tracking pass. Most of the atmospheric variability is captured by the TDCS calibrations, as indicated by the smooth ASD curve in Figure 2-28 and by the power spectrum in Figure 2-29.

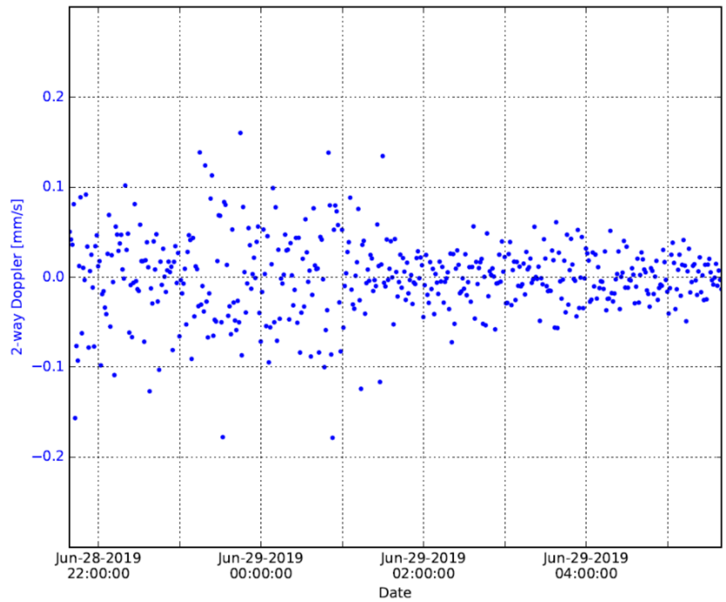


Figure 2-26 Postfit residuals for DOY 180 using GNSS-based calibrations. RMS: 4.29E-2 mm/s

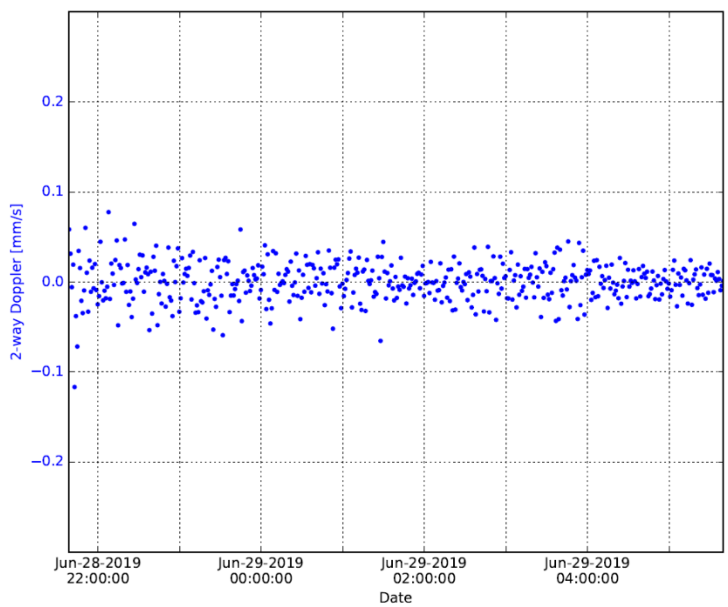


Figure 2-27 Postfit residuals for DOY 180 using TDCS-based calibrations. RMS: 2.16E-2 mm/s

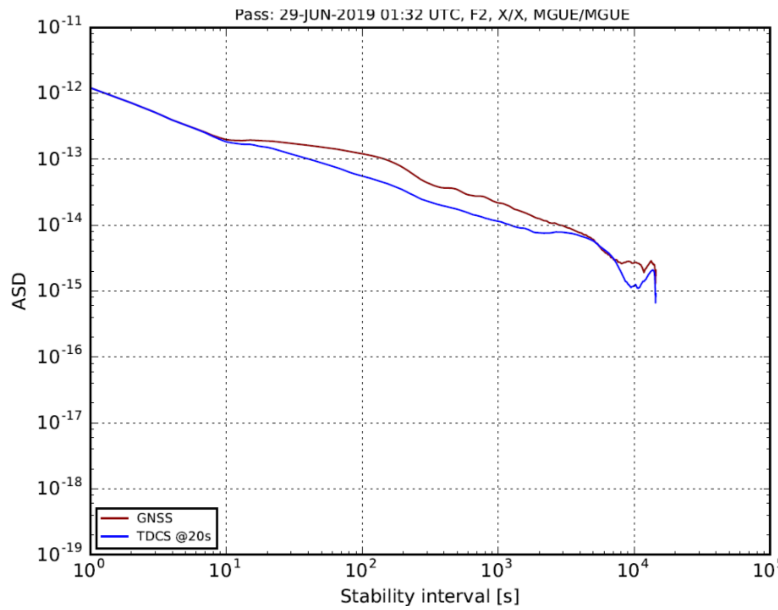

Figure 2-28 ASD of postfit residuals at DOY 180 using GNSS-based and TDCS-based calibrations.

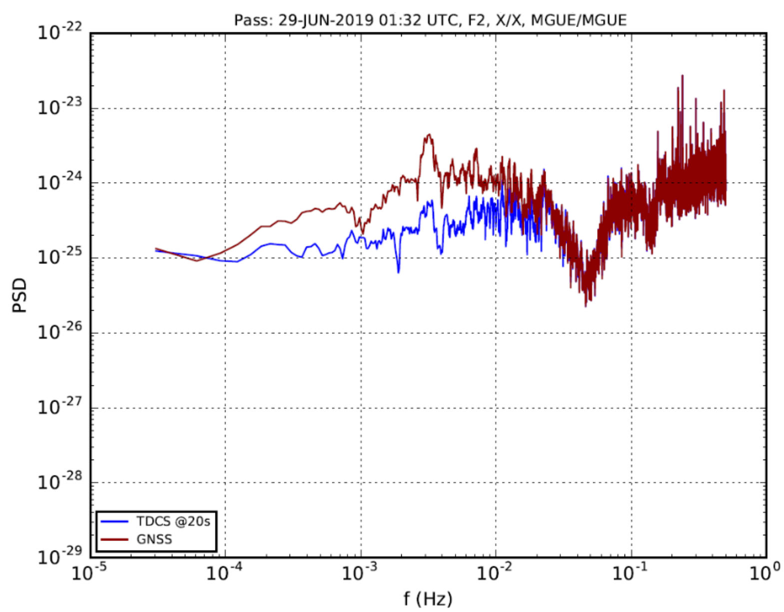

Figure 2-29 Multi-taper PSD of postfit residuals at DOY 180 using GNSS-based and TDCS-based calibrations.

#### *2.9.1.6 DOY 197 (July 16th)*

This arc was selected as representative of extreme dry conditions within the atmosphere, as indicated by the low ZWD values in Table 2-11. This is also confirmed by the ASD curves in Figure 2-32, which almost match a characteristic white-noise slope. Similarly, the power spectra in Figure 2-33 show characteristic values for low-frequency plateau that are at least one order of magnitude lower than the corresponding values for the previous arcs.

It should also be mentioned that a series of RCS impulsive maneuvers were performed during the course of the arc, introducing discontinuities in the data and several solve-for parameters that can potentially absorb atmospheric effects.

As a result, this arc is the one producing the worst performances in terms of noise reduction in the postfit residuals between the GNSS-based solution in Figure 2-30 and TDCS-based one in Figure 2-31 (a slight increase in the RMS of the residuals is actually observed).

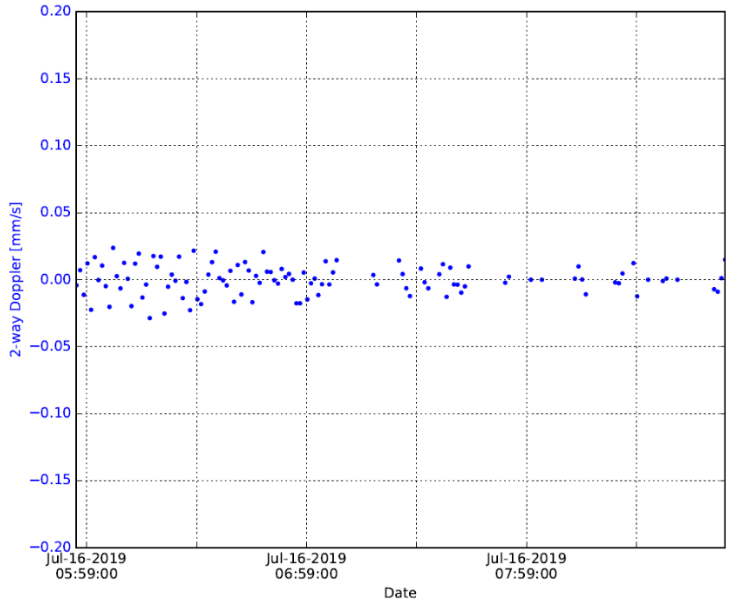


Figure 2-30 Postfit residuals for DOY 197 using GNSS-based calibrations. RMS: 1.11E-2 mm/s

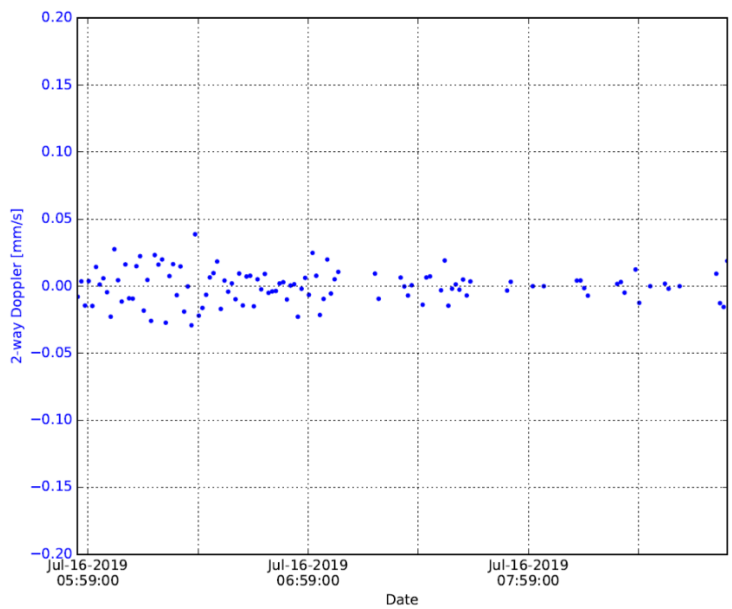


Figure 2-31 Postfit residuals for DOY 197 using TDCS-based calibrations. RMS: 1.24E-2 mm/s

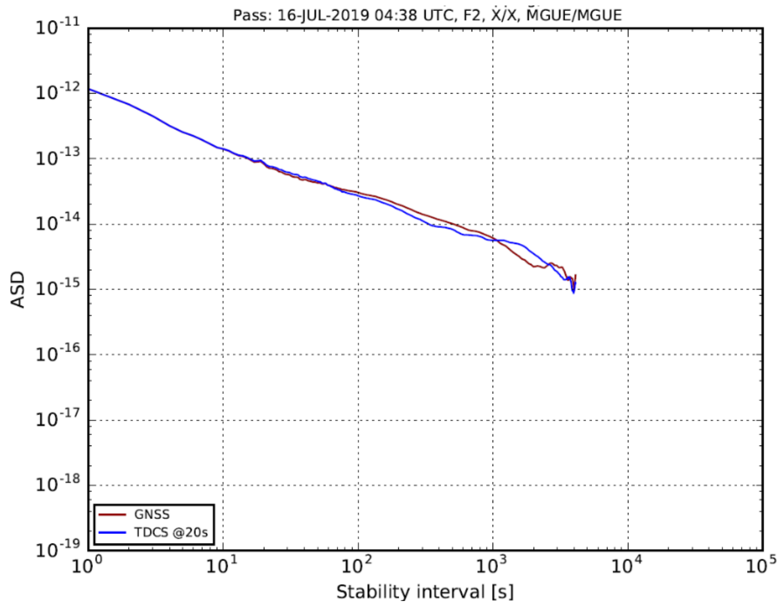


Figure 2-32 ASD of postfit residuals at DOY 197 using GNSS-based and TDCS-based calibrations.

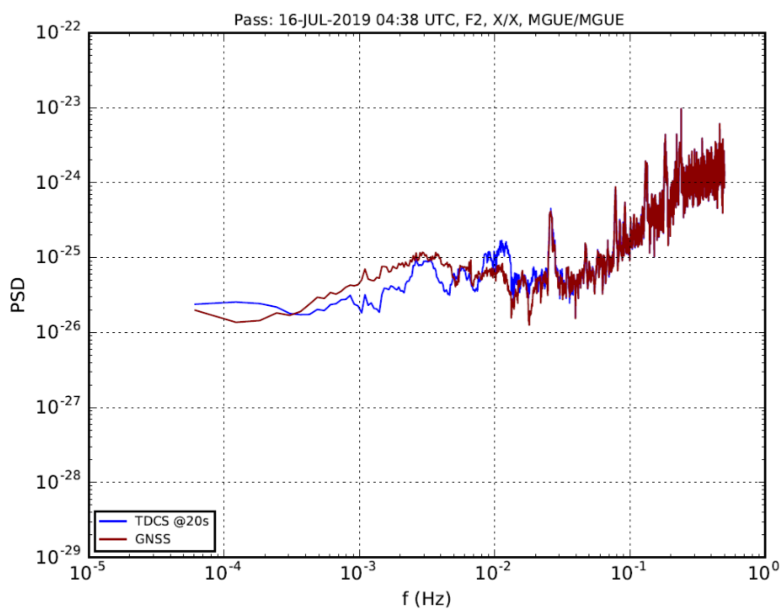


Figure 2-33 Multi-taper PSD of postfit residuals at DOY 197 using GNSS-based and TDCS-based calibrations.

### 2.9.2 Multi-arc summary

#### *2.9.2.1 Post-fit residuals*

A summary of the post-fit residuals for all tracking passes that were included in the OD analysis is given in Figure 2-34 and Figure 2-35.

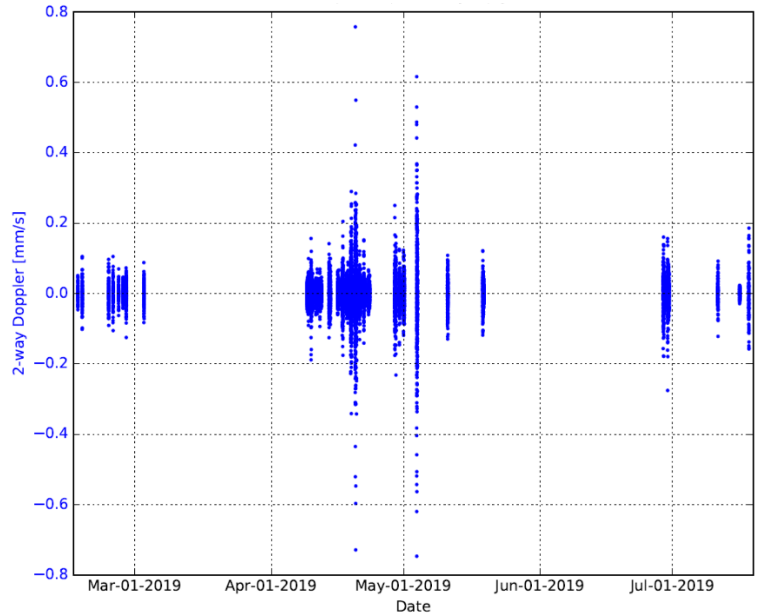


Figure 2-34 Postfit residuals for all tracking passes using GNSS-based calibrations. RMS: 5.39E-2 mm/s

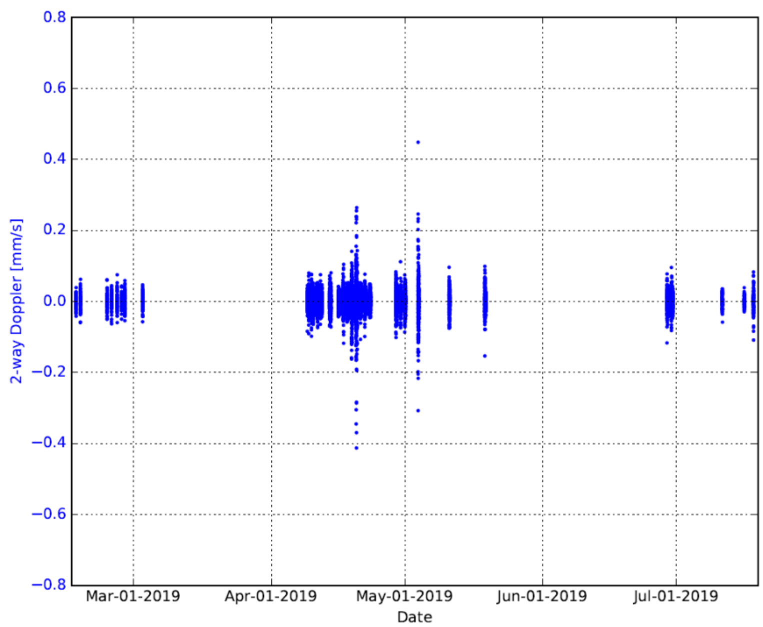


Figure 2-35 Postfit residuals for all tracking passes using TDCS-based calibrations. RMS: 2.91E-2 mm/s

Figure 2-36 and Figure 2-37, show the absolute and relative RMS values for the Doppler residuals as a function of the DOY for the tracking pass. The transparency factor $\alpha$ used for the filling colors, respectively red for the GNSS-based estimation, blue for the TDCS-based estimation, and black for the ratio between the two, is used to indicate the normalized number of valid observables $N_i/N_{max}$ within each arc. In other words, the full color, corresponding to a transparency vale of 1, is used when the number of valid Doppler observables $N_i$ is equal to the maximum number of observables from Table 2-11. The same RMS values are also reported in numerical form in Table 2-12.

Overall, we observe an average noise reduction of approximately 31% when using TDCS-based calibrations instead of GNSS-based ones.

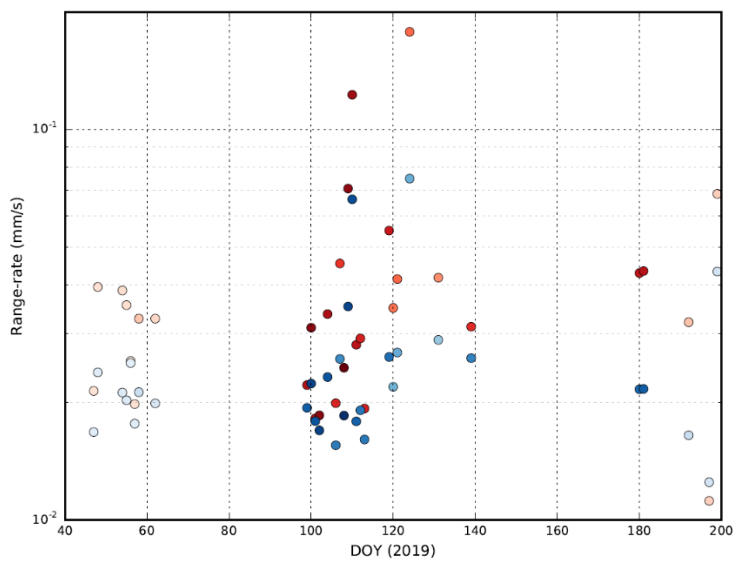


Figure 2-36 RMS of postfit residuals using GNSS-based (red) and TDCS-based (blue) calibrations.

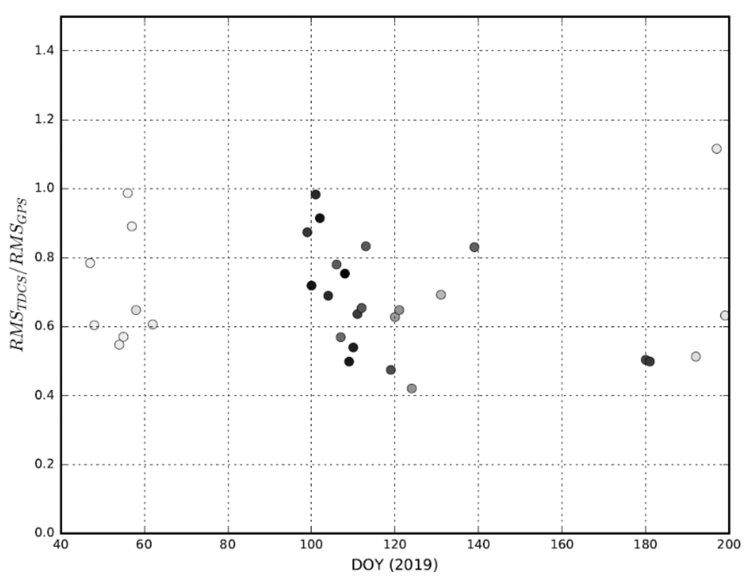


Figure 2-37 Ratio of RMS values between the TDCS-based and the GNSS-based OD solutions.

Table 2-12 Summary of RMS values and ratios for the Doppler residuals.

| DOY | $RMS_{TSAC}\,[mm/s]$ | $RMS_{TDCS}\,[mm/s]$ | $\frac{RMS_{TDCS}}{RMS_{TSAC}}$ |
|---|---|---|---|
| 47 | 2.14E-02 | 1.68E-02 | 0.78 |
| 48 | 3.95E-02 | 2.39E-02 | 0.60 |

| DOY | $RMS_{TSAC}\,[mm/s]$ | $RMS_{TDCS}\,[mm/s]$ | $\frac{RMS_{TDCS}}{RMS_{TSAC}}$ |
|---|---|---|---|
| 54 | 3.87E-02 | 2.12E-02 | 0.55 |
| 55 | 3.55E-02 | 2.03E-02 | 0.57 |
| 56 | 2.55E-02 | 2.52E-02 | 0.99 |
| 57 | 1.98E-02 | 1.77E-02 | 0.89 |
| 58 | 3.28E-02 | 2.13E-02 | 0.65 |
| 62 | 3.28E-02 | 1.99E-02 | 0.61 |
| 99 | 2.22E-02 | 1.94E-02 | 0.87 |
| 100 | 3.11E-02 | 2.24E-02 | 0.72 |
| 101 | 1.82E-02 | 1.79E-02 | 0.98 |
| 102 | 1.85E-02 | 1.70E-02 | 0.92 |
| 104 | 3.37E-02 | 2.32E-02 | 0.69 |
| 106 | 1.99E-02 | 1.55E-02 | 0.78 |
| 107 | 4.54E-02 | 2.59E-02 | 0.57 |
| 108 | 2.45E-02 | 1.85E-02 | 0.75 |
| 109 | 7.06E-02 | 3.52E-02 | 0.50 |
| 110 | 1.23E-01 | 6.62E-02 | 0.54 |
| 111 | 2.81E-02 | 1.79E-02 | 0.64 |
| 112 | 2.92E-02 | 1.91E-02 | 0.65 |
| 113 | 1.93E-02 | 1.61E-02 | 0.83 |
| 119 | 5.51E-02 | 2.62E-02 | 0.47 |
| 120 | 3.49E-02 | 2.19E-02 | 0.63 |
| 121 | 4.14E-02 | 2.68E-02 | 0.65 |
| 124 | 1.78E-01 | 7.49E-02 | 0.42 |
| 131 | 4.17E-02 | 2.89E-02 | 0.69 |
| 139 | 3.13E-02 | 2.60E-02 | 0.83 |
| 180 | 4.29E-02 | 2.16E-02 | 0.50 |
| 181 | 4.34E-02 | 2.17E-02 | 0.50 |
| 192 | 3.21E-02 | 1.65E-02 | 0.51 |
| 197 | 1.11E-02 | 1.24E-02 | 1.12 |
| 199 | 6.84E-02 | 4.33E-02 | 0.63 |

#### *2.9.2.2 Allan Standard Deviation*

Table 2-13 summarizes the ASD values at characteristic time scales for all tracking passes. ASD values at $10^4$ seconds are provided for a limited set of arcs, depending on the data availability and the length of the tracking pass. The same ASD values in Table 2-13 are also displayed graphically in Figure 2-38.

Table 2-13 ASD of postfit Doppler residuals using TDCS-based calibrations at 20 seconds integration time

| DOY | ASD @20s | ASD @60s | ASD @1000s | ASD @10000s |
|---|---|---|---|---|
| 47 | 1.462E-13 | 6.796E-14 | 8.615E-15 | |
| 48 | 1.638E-13 | 8.180E-14 | 1.011E-14 | |
| 54 | 2.028E-13 | 7.984E-14 | 1.238E-14 | |
| 55 | 1.727E-13 | 7.226E-14 | 1.710E-14 | |
| 56 | 1.694E-13 | 8.045E-14 | 1.291E-14 | |
| 57 | 1.533E-13 | 6.513E-14 | 1.409E-14 | |
| 58 | 1.739E-13 | 7.819E-14 | 1.983E-14 | |

| DOY | ASD @20s | ASD @60s | ASD @1000s | ASD @10000s |
|---|---|---|---|---|
| 62 | 1.737E-13 | 7.532E-14 | 1.500E-14 | |
| 99 | 1.483E-13 | 6.624E-14 | 2.156E-14 | 2.395E-15 |
| 100 | 1.707E-13 | 7.905E-14 | 2.920E-14 | 3.431E-15 |
| 101 | 1.449E-13 | 5.871E-14 | 2.634E-14 | 2.523E-15 |
| 102 | 1.447E-13 | 6.334E-14 | 2.020E-14 | 2.315E-15 |
| 104 | 1.779E-13 | 8.424E-14 | 2.057E-14 | 2.057E-15 |
| 106 | 1.443E-13 | 5.604E-14 | 1.543E-14 | 1.919E-15 |
| 107 | 1.884E-13 | 9.214E-14 | 1.826E-14 | 3.088E-15 |
| 108 | 1.464E-13 | 5.949E-14 | 2.492E-14 | 3.589E-15 |
| 109 | 2.544E-13 | 1.389E-13 | 1.712E-14 | 1.793E-15 |
| 110 | 4.044E-13 | 2.677E-13 | 5.666E-14 | 5.919E-15 |
| 111 | 1.574E-13 | 6.597E-14 | 1.677E-14 | 1.588E-15 |
| 112 | 1.468E-13 | 6.276E-14 | 1.791E-14 | 2.573E-15 |
| 113 | 1.458E-13 | 5.801E-14 | 1.373E-14 | 2.111E-15 |
| 119 | 2.039E-13 | 1.013E-13 | 2.358E-14 | 2.498E-15 |
| 120 | 1.747E-13 | 7.959E-14 | 8.739E-15 | |
| 121 | 2.026E-13 | 1.047E-13 | 1.965E-14 | |
| 124 | 5.965E-13 | 3.126E-13 | 2.118E-14 | |
| 131 | 1.850E-13 | 1.044E-13 | 1.474E-14 | |
| 139 | 1.648E-13 | 9.140E-14 | 1.491E-14 | 2.330E-15 |
| 180 | 1.522E-13 | 7.925E-14 | 1.139E-14 | 1.204E-15 |
| 181 | 1.638E-13 | 8.275E-14 | 1.384E-14 | 2.021E-15 |
| 192 | 1.043E-13 | 5.710E-14 | 1.993E-14 | |
| 197 | 8.719E-14 | 3.919E-14 | 5.643E-15 | |
| 199 | 2.245E-13 | 1.003E-13 | 1.976E-14 | |

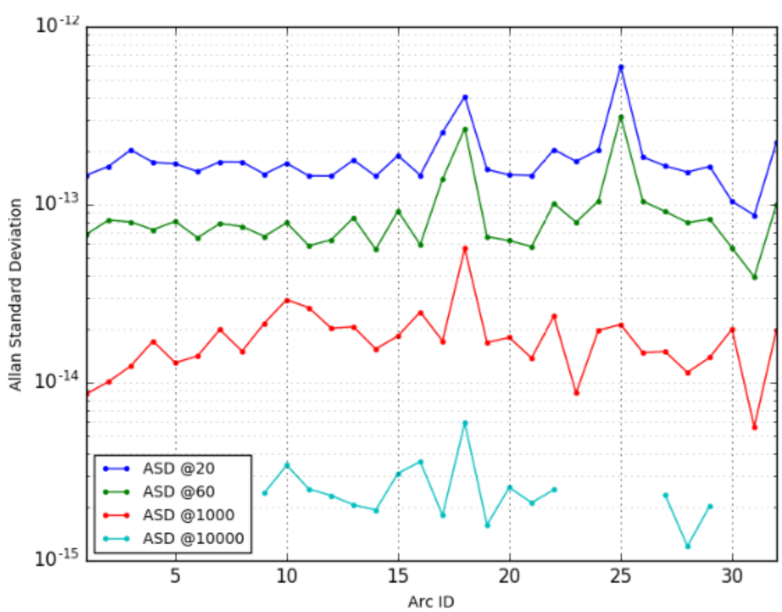


Figure 2-38 ASD of postfit residuals at characteristic stability intervals as a function of the arc ID (TDCS-based calibrations).

## 2.10 Interpretation

The main outcome of the results presented in 2.9 are the following:

- Using tropospheric calibrations generated by the TDCS, instead of standard GNSS-based calibrations, may reduce the residual Doppler noise by an amount that depends on the atmospheric conditions during the tracking pass. This improvement has been quantified in terms of reduction of RMS values and estimated to be on in the order of roughly 46 % for the analyzed test cases, with a maximum reduction around 60% under specific atmospheric conditions. A correlation was also hinted between relative noise reduction and absolute Doppler noise for the uncalibrated atmosphere, suggesting that this improvement could become more relevant for s/c tracking during daytime, when higher turbulence levels and integrated water content are generally expected (all GAIA passes occurred at night).
- A similar reduction was also observed for the ASD values of the calibrated Doppler residuals. Specifically, the highest improvements were observed for characteristic stability intervals between 100 and 1000 seconds.
- Power spectra of the doppler residuals, obtained using a MTSE technique, provide a valuable source of information regarding the relative frequency contributions to the atmospheric instability. Future work may focus on the identification of characteristic signatures within the spectra as markers of specific atmospheric conditions during the tracking passes.

It should be pointed out that the analysis performed for this study was not intended as a comprehensive OD exercise for the GAIA s/c but was meant as a testcase for evaluation of TDCS performances by direct comparison against GNSS-based calibrations. As such, the dynamical model used in the estimation process was kept as simple as possible, using mostly tabulated inputs for s/c accelerations and constants and limiting the number of solve-for parameters to a minimum.

# 3 Accurate ephemeris reconstruction for comet 67P/Churyumov-Gerasimenko from Rosetta data analysis

## 3.1 The Rosetta mission

The Rosetta mission was an ESA cornerstone mission whose main objectives were to rendezvous with comet 67P/Churyumov-Gerasimenko and to collect in-situ measurements of the comet while following its heliocentric trajectory.

### 3.1.1 Mission profile

Following its launch from an Ariane 5G+ on the 2nd March 2004, Rosetta endured a 10-year journey before reaching the comet. During this period, the s/c performed a sequence of four gravity assist maneuvers, three with the Earth [23] and one at Mars [24], to reduce its velocity-gap with respect to the comet.

After the second and third Earth gravity assists, Rosetta crossed the asteroid main belt, allowing to perform two asteroids flybys at 2867 Steins [25] and 21 Lutetia [26], respectively on the 5th September 2008 and 10th July 2010.

Between these major mission events and up to the rendezvous with comet 67P/CG, the s/c performed long interplanetary cruise phases, some of which were power critical due to the large heliocentric distances (up to 5.33 AU at aphelion). To reduce ground segment costs and avoid wear of components during these phases, the s/c was put in a "Deep Space Hibernation Mode" with minimal house-keeping functions and passive spin stabilization. The last hibernation, which lasted 31 months, ended with the s/c wake-up on the 20th of January 2014 and the beginning of the rendezvous maneuvers at the comet.

The main mission phases after reactivation are here summarized:

- <u>Rendezvous Maneuver</u> (RVM2): during this phase, the s/c had to slowly reduce its velocity in order to match that of the comet and improve the relative orbit reconstruction to adequate levels for proximity orbit insertion. Initially, the heliocentric states for the s/c and comet were estimated separately using radiometric measurements (Doppler, range, and occasionally ΔDOR) and ground-based astrometric data, respectively. As the s/c moved closer, the comet became visible within the OSIRIS and NAVCAMs field of views, first as point-like source against the background stars during the Near Comet Drift (NCD) phase, and eventually as an extended object during the Far Approach Trajectory (FAT) phase. A total of 7 OCMs were performed to reduce the relative velocity with respect to the comet, leading to the arrival at 67P/CG on August 6th, 2014.
- <u>Close Approach Trajectory</u> (CAT): this phase represented the transition from a centroid-based optical navigation to a landmark-based navigation. The s/c flew a series of pyramid-like hyperbolic orbits between 100 km and 60 km at low phase angles to ensure good illuminating conditions at the surface. A preliminary landmark database was created, along with a first estimation of the comet's shape and rotational state.
- <u>Global Mapping Phase</u> (GMP): during this phase, the s/c was flying bound circular orbits at 30 km, with larger phase angles to increase the surface coverage. It was also during this period that the landing site for Philae was selected.
- <u>Close Observation Phase</u> (COP): during this phase, the s/c was flying terminator orbits at 20 km and 10 km, allowing to improve significantly the knowledge of the comet's gravity field and COM, and providing higher resolution images of the selected site in preparation for Philae landing.
- <u>Lander Delivery Phase</u> (LDP): after transferring to a temporary parking orbit at about 30 km, the s/c was put in an almost collision course hyperbolic orbit, from which the Philae lander was deployed

towards the Agilkia region on the comet's smaller lobe. Touchdown was confirmed around 15:34 UTC on November 12th. However, Philae failed to anchor its harpoon to the comet surface and bounced several times before setting at its final landing site near a crater rim, where poor illuminating conditions prevented battery charging. The lander successfully performed the First Science Sequence (FSS) operating on its primary battery, right before going asleep on 15th November.

- Comet Escort Phase: Rosetta escorted the comet until perihelion and outwards again, with the objective of monitoring the evolution of the comet's activity. This escort phase was characterized by increasing comet activity, which forced the s/c to move towards progressively higher altitude orbits. After an initial period in circular terminator orbits between 20 km and 30 km, the s/c flew a series of hyperbolic orbits at variable distances, with occasional low-altitude flybys. A variation from this operational routine is represented by the far excursions to the comet's coma and to the nightside tail, respectively in October 2015 [27] and April 2016 [28], in support to scientific observations. Only around March 2016 the comet activity started to decrease to a point where close bounded orbits were again possible.
- End of Mission Phase: originally planned to end in December 2015, the mission was extended up to September 2016. At that point Rosetta would enter a period of superior solar conjunction with a prohibitive 4 AU heliocentric distance, making further operations impossible. At first, the s/c was put into dawn-dusk terminator orbits at 10 km and 7 km, followed by a series of circular orbits at 30 km with variable phase angles. Images collected by the NAVCAMs and by OSIRIS during this period were combined to build a new set of high-resolution landmarks over the comet's surface. In a second phase, the s/c flew a series of 15 elliptical orbits, or 'Flyover orbits' with a fixed period of 3 days and a progressively decreasing altitude of pericenter [29]. As distance decreased, these orbits were characterized by increasing navigation requirements but also allowed for scientific observations of unprecedented resolution and accurate estimation of the comet's gravitational field . Finally, the s/c orbit was raised to 23 km and set to a descent trajectory towards the comet's smaller lobe in the Ma'at region, where a soft touchdown occurred at 10:39 UTC on 30th September 2016, marking the end of the Rosetta mission.

Figure 3-1 gives an overview of the s/c cometocentric distance as a function of time for the comet proximity phase, covering all the mission phases from FAR to the EoM.

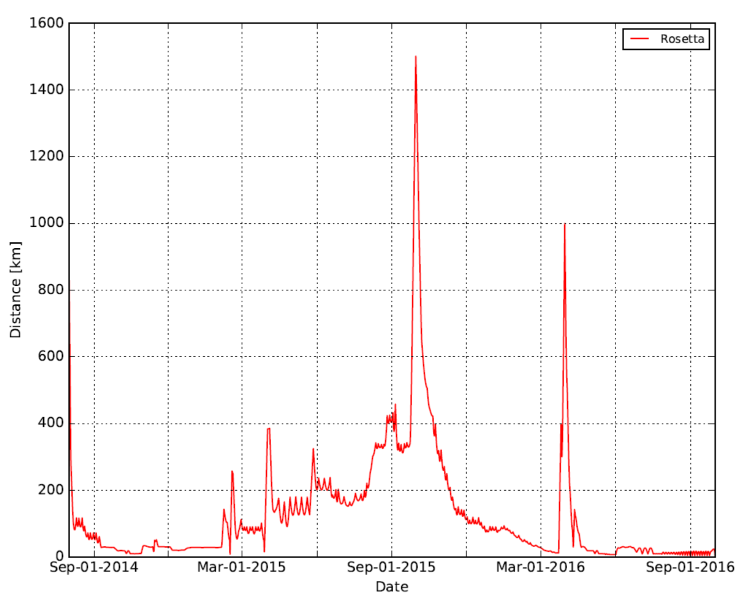


Figure 3-1 Rosetta's distance from the comet from August 2014 to September 2016

### 3.1.2 The Rosetta spacecraft

The Rosetta s/c is based on a box-type type structure ($2.8\ x\ 2.1\ x\ 2.0\ m$) on which all systems and payload equipment are mounted (see Figure 3-2). This structure is built around a vertical tube, which contains the propellant tanks and acts as main thrust interface with the Ariane-5 launcher.

The main elements composing the structure are:

- The Bus Support Module (BSM), which accommodates most of the platform and avionics equipment and is located in the lower section of the orbiter (-Z side).
- The Payload Support Module (PSM), which accommodates all the science equipment and is located in the upper section of the orbiter (+Z side).
- The High Gain Antenna (HGA), a two-axes steerable parabolic antenna located on the +X side of the s/c bus. Originally stowed against the side during launch, the HGA is deployed on a tripod assembly mounted in the lower portion of the bus, allowing more than hemispherical pointing range.
- Two Solar Arrays (SA), each comprising 5-panel wings folded against the +/-Y sides of the s/c bus. Once deployed, the two 14 m arrays, with a combined area of 64 $m^2$, ensure a minimum power output of 440 W at maximum distance from the Sun (5.3 AU).
- The Philae Lander, a 100 kg external module, mounted on the -X side of the s/c, which was deployed to the comet's surface in November 2015.

Rosetta is a three-axis stabilized s/c, relying on two Navigation Cameras (NAVCAM), 2 Star Trackers (ST), and 3 Inertial Measurement Units (IMU) for relative orbit reconstruction and attitude determination. Attitude control is achieved using a set of 4 Reaction Wheels (RW) and 24 10N thrusters, which are also used for orbital controls and RW desaturation. The propulsion system is a pressure-fed bipropellant type using Mono-Methyl-hydrazine (NNH) and Nitrogen-Tetroxide (NTO) for a total ΔV capacity of 2100 m/s.

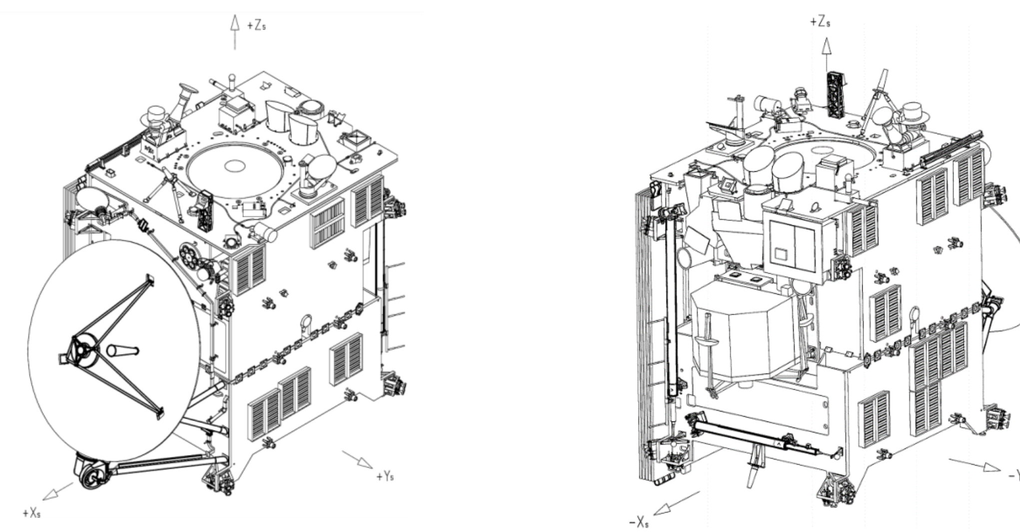


Figure 3-2 Rosetta schematics.

Rosetta PSM housed a total of 11 scientific instruments, which allowed to perform the most detailed study of a comet to date. A list of these instruments with their main components and objectives is given below:

- ALICE: an ultraviolet imaging spectrometer used to characterize the composition of the cometary nucleus and coma in the far ultraviolet and extreme ultraviolet spectral regions.
- CONSERT (Comet Nucleus Sounding Experiment by Radio wave Transmission): this experiment, composed of an orbital subsystem and a lander subsystem, aimed at establishing a radio link passing

through the cometary nucleus. By measuring the propagation delay, as the radio waves passed through different sections of the nucleus, it would allow to determine its dielectric properties, homogeneity, and internal structure.

- COSIMA (Cometary Secondary Ion Mass Analyzer): consisting of a dust collector, an optical microscope for target characterization, a primary ion gun for dust particles bombardment (using Indium ions), and a secondary ion time-of-flight mass spectrometer.
- GIADA (Grain Impact Analyzer and Dust Accumulator): this instrument measured the size, velocity and momentum of coma dust particles using an optical detector and a mechanical impact sensor.
- MIDAS (Micro-Imaging Dust Analysis System): this instrument used the technique of atomic force microscopy to perform textural and statistical analysis of the cometary dust particles.
- MIRO (Microwave Instrument for the Rosetta Orbiter): used to estimate the thermal and electrical properties of the comet by measuring its near surface temperature. The spectrometer portion of the instrument allowed to measure molecular abundances of selected species (water, carbon monoxide, ammonia and methanol) in the cometary coma.
- OSIRIS (Optical, Spectroscopic, and Infrared Remote Imaging System): consisting in two independent camera systems operating in the visible, near-infrared and near ultraviolet; a narrow-angle camera for high resolution imaging of the nucleus and a wide-angle camera for dust and gas imaging.
- ROSINA (Rosetta Orbiter Spectrometer for Ion and Infrared Remote Imaging System): a suite of sensors including two mass spectrometers and two pressure gauges to provide density and velocity profiles of the ejecta.
- RPC (Rosetta Plasma Consortium): a set of five sensors designed to characterize the plasma environment around the comet.
- RSI (Radio Science Investigation): this instrument makes use of the existing communication system infrastructure, both onboard the s/c and on ground, and of the s/c USO to retrieve information on the motion of the s/c, the perturbing forces acting on it, and the physical properties of the propagating medium.
- VIRTIS (Visible and Infrared Thermal Imaging Spectrometer): an imaging spectrometer combining three data channels, two committed to spectral mapping and one solely to spectroscopy.

Ten additional scientific instruments were carried onboard the Philae Lander, which was the first spacecraft ever to make a soft landing on the surface of a cometary nucleus. These instruments operated only for a few days as part of the FSS operations (see 3.1.1), which were run completely on battery.

### 3.1.3 Radio Science Investigation (RSI)

#### *3.1.3.1 Scientific objectives*

The RSI experiment had the following primary objectives:

- <u>Comet gravity measurements</u>: these measurements are strictly coupled with the OD problem. By processing range and Doppler radiometric measurements, the s/c trajectory can be determined and the gravity accelerations acting on the s/c can be inferred from line-of-sight velocity variations. Initial mass determination was performed using flybys in the comet approach phase, while higher order gravitational harmonics required low altitude bound orbits to be estimated. The reconstructed gravity model from comet shape (assuming uniform density) and the estimated model can then be compared to obtain information on the mass heterogeneity within the nucleus.
- Comet nucleus investigations

- Radar occultations: by measuring the accurate times of ingress and egress at the comet limbs over different occultation geometries, these measurements allow to constrain the nucleus shape. Depending on the refractive properties of the comet, the upper layers of the nucleus may be penetrable by microwaves, allowing to constrain the bulk refractive index.
- Bistatic Radar: Rosetta was the first s/c to use bistatic radar to study the scattering properties of the surface of a comet. In this configuration, the HGA is pointed towards the nucleus, a one-way dual link signal is transmitted from the s/c and reflected off the surface before being received by ground station. By measuring the strength and polarization of the scattered signal, it is possible to infer physical properties of the surface material, such as its dielectric constant and surface roughness on scales comparable to the signal wavelength.

- Coma investigation. Analysis of radio signals that have propagated through, or were scattered by, a target media, can be used to infer physical properties of the media. In particular, the following investigations were performed during the Rosetta mission:
  - Abundance of $[\mathrm{mm}, \mathrm{dm}]$ size cometary dust: by measuring the attenuation and near-forward scattering of X-band radio signals during coma occultations allows to constrain the distribution of dust grains in a size range comparable with the wavelength (3.5 cm for X-band).
  - Plasma content: by measuring the phase variation of radio signals as they pass through the cometary ionosphere, it is possible to estimate the plasma ion densities. Dual frequency observations are needed to separate dispersive contributions from the classical Doppler effect.

#### *3.1.3.2 Spacecraft segment*

The Rosetta RSI subsystem comprised several components in redundant pairs (except for the HGA):

- A High Gain Antenna (HGA) with a 2.2 m diameter parabolic dish, which provides receiving capabilities at S-band and X-band and transmitting capabilities at X-band.
- Two Low Gain Antennae (LGA) at S-band, mounted on the +/- Z faces of the bus structure to provide quasi omnidirectional coverage for any s/c attitude. These were used for telemetry downlink and telecommand uplink in near-Earth phases or during emergencies.
- Two Medium Gain Antennae (MGA). A flat patched array antenna operating at S-band, and an offset type 0.31 m reflector antenna operating at X-band. These were mostly used for downlink and telecommand uplink in near-Earth phases or as backup during emergencies.
- A Radio Frequency Distribution Unit (RFDU), switching the onboard RF hardware between the antennae.
- An Ultra Stable Oscillator (USO) providing a stable frequency reference for one-way links.
- Two Travelling Wave Tube Amplifiers (TWTA), providing 60 W power amplification for the X-band transmission (S-band transmitter power was generated within the transponders).
- Two transponders, each consisting of an S-band and X-band receiver and transmitter.

The RSI instrument operated in two alternative modes:

- Coherent two-way link: in this mode, the ground station generates an uplink signal, which is received by the s/c and used to generate the downlink signal using the constant transponder ratios shown in Table 3-1. This mode has the advantage of relying on the higher frequency stability of the ground station oscillator.

- One-way link: in this mode, the signal is generated onboard the s/c using as frequency reference the onboard USO and transmitting coherent downlink signals at S-band and X-band. This mode is mostly used for bistatic radar and occultation experiments.

Table 3-1 S/C transponder ratios

| Up/Down | S-band | X-band |
|---|---|---|
| **S-band** | 240/221 | 880/221 |
| **X-band** | 240/749 | 880/749 |

## 3.2 The scientific case for an ephemeris reconstruction

### 3.2.1 Scientific objectives

The reference heliocentric trajectory for comet 67P/CG is represented by the multi-arc orbital solution generated by ESOC's FD team, which is currently available in form of SPICE kernel (see Table 3-2). This solution was obtained by merging several long-arc and short-arc OD solutions obtained during Rosetta operations, which combined optical and radiometric measurements to estimate the relative s/c trajectory and a series of physical parameters including the comet's orbital parameters and rotation state.

Theoretically, one could estimate the magnitude of the non-gravitational accelerations acting on the comet by computing the second derivative of the measured heliocentric position and subtracting all gravitational accelerations [30]. However, it can be observed from Figure 3-3, that the reconstructed trajectory contains several position discontinuities, with magnitudes in the order of tens or even hundreds of km. Similar discontinuities are also observed for the comet velocity, with magnitudes in the order of a few cm/s.

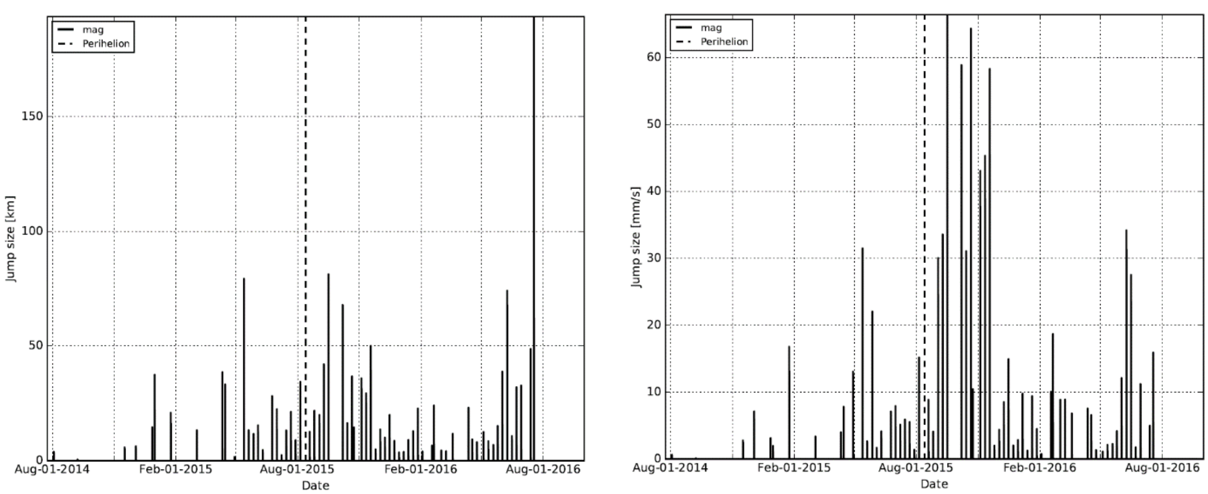


Figure 3-3 Heliocentric state discontinuities for comet 67P.

These discontinuities, which occur at the boundaries of the original short/long-arc integration segments that compose the reconstructed trajectory, are a product of the dynamical mismodelling for the comet state estimation, which did not include NGAs from surface outgassing.

The OD effort that is presented within this study was therefore motived by the following objectives:

- Provide a continuous ephemeris reconstruction for comet 67P/CG for the period between July 2014 and September 2016 during which Rosetta was in proximity of the comet.

- Reduce the uncertainty in the heliocentric state estimation for 67P/CG for the same time period.
- Provide an estimate of the NGAs acting on the comet due to surface outgassing.

As pointed out in recent works on this topic (see [30] and [31]), an improved reconstruction of the comet ephemeris and an accurate estimation of the NGAs acting on the comet as a function of time around perihelion, represent key steps towards understanding the physical processes acting on the surface. The availability of continuous radiometric measurements collected by the Rosetta s/c on its two-year long rendezvous with comet 67P/CG provide a unique opportunity to address these issues.

A new ephemeris solution for 67P/CG is also proposed in a recent study by JPL [32], which combines high-quality radiometric data collected during the Rosetta mission with ground-based astrometric measurements to reconstruct the comet's trajectory from 2012 to 2018. Although the overall goals of the JPL study and of the current investigation are similar, several key differences are present, which result in different (albeit compatible) trajectory reconstructions:

- Only a limited set of range observables is used for the JPL study. These measurements correspond to DSN range data collected during the months of September/October 2014 and August/September 2016, when the Rosetta s/c is sufficiently close to the comet to allow for an accurate relative orbit reconstruction with an uncertainty of less then 10 m.
- A rotating jet model [33] is used to represent the NGA due to comet outgassing, using globally estimated parameters with a-priori values informed by Rosetta scientific investigations.

This approach allows to obtain a robust orbit reconstruction and ephemeris prediction during the pre-perihelion and post-perihelion phases. However, the lack of observables in proximity of perihelion and the use of a global NGA model does not allow for the estimation of short time-scale variations of the NGA, which represents a key step towards linking the observed non-gravitational motion of the comet to the physical properties of its surface. Conversely, the current investigation uses all range measurements collected by DSN and ESTRACK stations throughout the Rosetta mission, including measurements around perihelion, for which the relative orbit reconstruction is degraded and a suitable weighting scheme is required. Moreover, short time-scale variations in the surface outgassing are addressed using stochastic NGA models within the filter.

### 3.2.2 High-level OD approach

The OD approach that is employed for this analysis has already been used for ephemerides reconstruction of planets and small bodies using deep-space probes [32], [33] and planetary orbiters [34]. This approach assumes the relative orbit between the deep space probe and its target to be known, along with an a-priori knowledge of its uncertainty. Range and ΔDOR radiometric observables, which are computed with respect to a reference location on the s/c frame (usually the phase center of the HGA), are then "mapped" to the center of the target body using the relative trajectory as a time-dependent offset. These mapped observables are then included within the filter to estimate the trajectory of the target body and a series of related physical parameters. The uncertainty of the mapped radiometric observables is now a function of the original measurement uncertainty, of the relative orbit uncertainty, and of the orbit geometry with respect to the Earth LOS direction. Depending on the particular mission phase, the uncertainty can be dominated by its measurement component (when the relative trajectory is accurately known) or by its orbit component.

For the case of Rosetta, two-way Range errors are dominated by the uncalibrated station and media delays, with magnitudes the order of 5 meters. The relative orbit uncertainty has accuracies that can vary up to two orders of magnitude, in the order of 5 to 500 meters, depending mainly on the relative distance from the comet. Hence, the measurement uncertainty of the mapped ranging observables is dominated by the uncertainty in the relative trajectory.

Conversely, the ΔDOR measurement show projected errors in the plane of the sky in the order of 3 to 6 km, causing the mapped ΔDOR error to be dominated by the measurement component.

In the current scenario, Rosetta's relative trajectory was estimated by ESOC FD in a series of long-arc and short-arc solutions during mission operations. After the end of mission, the single solutions were combined into SPK files containing the heliocentric positions of Rosetta and comet 67P/CG (see Table 3-2). Unfortunately, a consistent estimation for the uncertainty of the relative orbit reconstruction could not be provided by ESOC FD. Therefore, the proposed weighting scheme for the mapped radiometric measurements relies on an empirical formulation for the relative orbit uncertainty, as described in 3.5.7.

## 3.3 Dynamical model

To correctly estimate the trajectory of comet 67P/CG, all non-negligible forces acting on the comet were included within the implemented dynamical model. In this section we give a brief description of these forces. More details about their mathematical implementation can be found in [2].

### 3.3.1 Gravitational Accelerations

The dynamical model includes gravitational accelerations from the main Solar System bodies (the Sun, the planets and their satellites) and from the most massive small bodies within the main asteroid belt. In particular, the following effects are active:

- Relativistic point-mass gravity acceleration from the Sun, the planets, the Moon, and Pluto. With the exception of the Earth, all planets and their satellites are represented as a single body corresponding to the system's COM.
- Newtonian point-mass gravity acceleration from the 343 most massive bodies in the main asteroid belt.
- Gravitational $J_2$ perturbation from the Sun's oblateness.

State vectors and gravitational parameters for the Sun, the planets and their satellites are taken from JPL's DE438, with the exception of the Sun's $J_2$ and pole coordinates that are taken from DE430 [12]. State vectors and gravitational parameters for the main asteroid belt objects are taken from DE430.

### 3.3.2 Non-Gravitational Accelerations

The main NGA acting on a comet when it passes through the inner Solar System, is represented by the surface outgassing induced by the solar irradiance. When the comet comes closer to the Sun, surface temperatures start to grow, eventually leading to the sublimation of sub-surface ice volatiles such as water and carbon monoxide. As these gasses are accelerated through the surface, their momentum is transferred to dust particles and other small debris, which may reach escape velocity and contribute to form the characteristic comas around the comets' nuclei. After the early characterization by Whipple in the 1950s [35], a wide array of models have been proposed to describe this perturbing effect. Most of these models are very complex and based on poorly known parameters linked to the surface's chemical composition and thermo-optical properties [36] [30], or to the morphology of the comet's nucleus [37]. The approach that was used for this work involves simpler empirical models to obtain a baseline estimation of the NGAs acting on comet 67P/CG that is unbiased by the selection of a particular physical mechanism to explain the surface outgassing. More complex outgassing models can then be constrained with this baseline solution, or included within the OD itself as part of further studies.

Several test cases were explored for this analysis by using alternative NGA models with variable levels of complexity. A statistical analysis was then performed for each of these cases to identify which models are able to accurately fit the radiometric observables while minimizing the degrees of freedom. This process is critical when stochastic acceleration models are involved. An excess of degrees of freedom is often the cause of “over-fitting”, where unmodelled dynamical and observation effects are compensated for during the estimation of the stochastic parameters, eventually leading to non-physical NGA solutions.

The models used in the following analysis are hereby listed:

#### *3.3.2.1 Standard Model (SM)*

The SM represents one of the most successful models used to describe the NGA acting on a comet nucleus due to surface outgassing. This empirical formulation, described by Mardsen in [38], is based on the assumption that the three components of the comet’s NGA in the RTN dynamic frame can be expressed as in (3.1) as the product of a constant scale factor $A_i$ and a function $g$ that simulates the water ice sublimation rate. This latter is expressed as a function of the comet’s heliocentric distance in (3.2), where $m = 2.15$, $n = 5.093$, $k = 4.6142$, $r_0 = 2.808\ AU$, and the value of the normalization scale factor $\alpha = 0.1113$ is such that $g(1) = 1$. Using this formalism, the scale factors $A_i$ represent the acceleration components at a reference distance of 1 AU.

$$\vec{a} = g(r) \cdot (A_R \hat{e}_R + A_T \hat{e}_T + A_N \hat{e}_N) \tag{3.1}$$

$$g(r) = \alpha \left(\frac{r}{r_0}\right)^{-m} [1 + \left(\frac{r}{r_0}\right)^{n}]^{-k} \tag{3.2}$$

Typical values for the scale factors of short period comets lie in the range of $[10^{-8}, 10^{-6}]\ m/s^2$ [39]. More specifically, previous OD analyses for comet 67P/CG, using astrometric measurements from the last six comet apparitions, produced estimations for the scale factors in the order of $A_R \approx 10^{-8}\ m/s^2$ for the radial components and $A_{T,N} \approx 10^{-9}\ m/s^2$ for the tangential and normal components ( [31], [40] ).

While the $g(r)$ function described by Mardsen is based on a water isothermal sublimation model, alternative formulations have been proposed, employing power laws to express the acceleration dependence from the heliocentric distance [41]. In particular, the water production rate for 67P/CG was shown to be better approximated by a $g(r)\sim r^{-5}$ power law ( [43], [32] ).

#### *3.3.2.2 Extended Standard Model (ESM)*

The ESM is a generalization of the SM, which was originally proposed by Yeomans & Chodas to account for observed asymmetries in the comet outgassing around perihelion [41]. The acceleration components in the RTN frame are expressed as in (3.1), while the sublimation function is now expressed according to (3.3), where $\Delta T$ represents the time offset between the peak of the comet activity and the perihelion.

$$g(r') = g\big(r(t - \Delta T)\big) \tag{3.3}$$

Single values for the RTN scale factors $A_i$ and for the time offset $\tau$ are solved-for within the filter. Typical values for the time offset are in the order of a few weeks at the most. In particular, estimated values from previous OD analyses for 67P/CG, using astrometric measurements and assuming a $g(r')\sim r^{-2.15}$ power law, are in the order of 30 to 35 days [40].

#### *3.3.2.3 Rotating Jet Model (RJM)*

The Rotating Jet Model (RJM) is based on the assumption that the comet NGA can be described through a finite number of localized jets stemming from the comet’s surface.

The instantaneous acceleration induced by a single jet is expressed as in (3.4), where $A_J$ is the intrinsic jet strength, $z$ is the solar zenith angle at the jet source, $\hat{e}_J$ is the unit vector of the instantaneous jet direction, and $g(r')$ is the asymmetric sublimation function described in (3.3).

$$\overrightarrow{a_J} = -g(r') A_J \cos z\, \hat{e}_J \tag{3.4}$$

Using this formalism, the jet strength $A_J$ represents the acceleration that the jet would produce at an heliocentric distance of 1AU when the Sun is at the local zenith.

By averaging the instantaneous acceleration over a single comet rotation, it is possible to obtain the expression in (3.5), where $\hat{e}_S$ denotes the Sun's projection over the comet's equator, $\hat{e}_P$ denotes the rotation axis of the comet, $\hat{e}_Q$ is the cross product between these two unit vectors, and $\Delta\theta$ is the diurnal lag angle between the maximum activity of the jet and the solar meridian crossing. The parameters $J_S$ and $J_P$ account for variations of the daily insulation experienced by the jet assuming a spherical shape for the comet. These values, which depend on the subsolar latitude (seasonal variation) and on the colatitude of the specific jet location $\eta$, have different formulations depending on whether the jet is in the polar night regime ($J_S = J_P = 0$), polar day regime, or diurnal regime. The complete mathematical formulation for $J_S$ and $J_P$ (not reported here for brevity) can be found in [33] along with the derivation of (3.5) and of the partial derivatives of the acceleration with respect to the comet state and the model parameters.

$$\bar{a}_J = g(r')A_J\vec{J} = g(r')A_J(J_S\cos\Delta\theta\,\hat{e}_S + J_S\sin\Delta\theta\,\hat{e}_Q + J_P\hat{e}_P) \tag{3.5}$$

The RJM accounts for seasonal variations of the jet activity by exploiting the a-priori knowledge of the comet's spin axis and is therefore a higher fidelity model with respect to the ESM. Moreover, an arbitrary number of jets can be included through superposition, to obtain the more general expression for the acceleration give in (3.6).

$$\bar{a}_{RJM} = g(r')\sum_{i=1}^{N} A_{Ji}\vec{J}_i \tag{3.6}$$

#### 3.3.2.4 Constant Stochastic Model (CSM)

Acceleration components in the RTN frame are modelled as degree-zero polynomials (constants) for each of the $N$ stochastic time intervals. The $3N$ polynomial coefficients are solved-for within the filter.

$$a_i(t) = a_i|_k \quad for\ \ k \in [1, N] \tag{3.7}$$

#### 3.3.2.5 Linear Stochastic Model (LSM)

Acceleration components in the RTN frame are modelled as degree-one polynomials (linear functions) for each of the $N$ stochastic time intervals. The $6N$ polynomial coefficients are solved-for within the filter.

$$a_i(t) = a_i|_k + t\cdot j_i|_k \quad for\ \ k \in [1, N] \tag{3.8}$$

Additional constraints are included for the *Linear stochastic* case to enforce continuity of the acceleration values at successive stochastic intervals. The expression for this constraint is given in (3.9), where $j_i|_k$ is the estimated jerk at the $k^{th}$ stochastic interval, and $\varepsilon \ll 1$.

$$a_i|_{k+1} - (a_i|_k + \Delta T\cdot j_i|_k) < \varepsilon \quad for\ \ k \in [1, N] \tag{3.9}$$

## 3.4 Rosetta's relative trajectory

The ephemeris' reconstruction for comet 67P/CG requires the knowledge of the relative trajectory of Rosetta around the comet to map the s/c range measurements to the position of the comet's nucleus.

However, the latest SPICE kernels for the Rosetta mission, which are summarized in Table 3-2, only provide the heliocentric trajectories for the target bodies, which are therefore combined to obtain the relative trajectory. As a first step, these kernels were imported in MONTE and converted to a Chebyshev polynomial representation covering the duration of Rosetta's proximity phase. The reference center for the orbit is then switched by subtracting the corresponding trajectory arcs.

Table 3-2 Summary of the latest SPICE kernels for the Rosetta mission

| Target | File name | Start | End |
|---|---|---|---|
| Rosetta | RORB_DV_257_03___T19_00354.BSP | 01/01/2014 | 05/10/2016 |
| 67P-CG | CORB_DV_257_03___T19_00354.BSP | 01/01/2014 | 01/01/2017 |
| Planets | DE405.BSP | 01/01/1950 | 01/01/2050 |

A sensitivity analysis was performed by varying the time step and degree of the fitting polynomials, which were used during the trajectory conversion, to address how these parameters affect the accuracy of the fitted solution. The reconstructed relative orbit was sampled at periodic time intervals and compared with the reference heliocentric trajectory to compute the state error. A plot of the state errors as a function of time is given in Figure 3-4 for the selected degree 5 Chebyshev fit using time steps of 1 minute. It can be seen that the reconstructed relative position has accuracies below $cm$ level for the majority of the covered time interval, and always less than 3.5 $cm$.

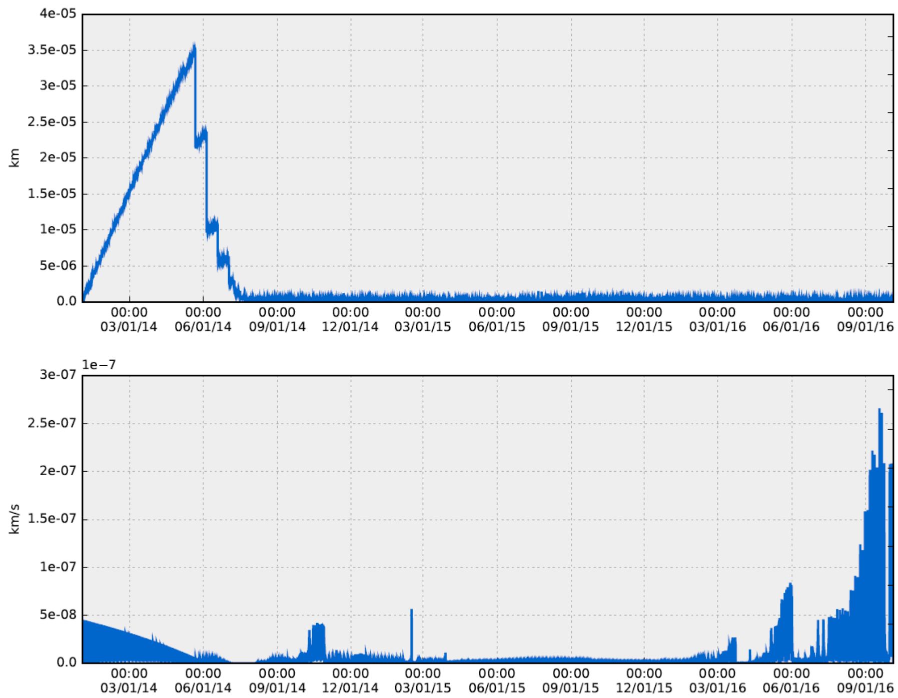


Figure 3-4 Position and velocity errors for the reconstructed Rosetta orbit with respect to 67P/CG.

## 3.5 Data selection and pre-processing

### 3.5.1 Data summary

During the proximity phase of the Rosetta mission, radiometric measurements at X-band (8.5 GHz) were acquired by ESA's ESTRACK complexes of Cebreros, Malargue and New Norcia, and by NASA's DSN antennae at the complexes of Canberra, Goldstone, and Madrid. Of the different radiometric measurements that were collected throughout the mission, only ranging and ΔDOR data were used for this analysis due to the information content that they provide for ephemerides reconstruction.

A list of range measurements collected at each station is given in Table 3-3. The total number of measurements included within the OD filter and the number of ignored measurements (indicated in 4th and 5th columns, respectively) refer to the reduced range dataset described in 3.5.5 and having approximate sampling intervals of 5 minutes.

A similar list for the ΔDOR measurements at the Cebreros/Malargue and Cebreros/New-Norcia baselines is given in Table 3-4.

Table 3-3 Summary of processed range observables

| Type | Complex | Antenna | Good | Ignored | Start | End |
|---|---|---|---|---|---|---|
| DSN | Goldstone | DSS 14 | 16352 | 257 | 16/07/2014 | 14/10/2016 |
| | | DSS 15 | 3704 | 1 | 09/07/2014 | 22/09/2016 |
| | | DSS 24 | 1952 | 18 | 17/07/2014 | 08/10/2016 |
| | | DSS 25 | 3138 | 4 | 12/08/2014 | 22/09/2016 |
| | | DSS 26 | 2375 | 11 | 20/07/2014 | 06/10/2016 |
| | Canberra | DSS 34 | 2407 | 13 | 19/10/2014 | 01/10/2016 |
| | | DSS 35 | 3248 | 41 | 18/05/2015 | 21/08/2016 |
| | | DSS 43 | 7296 | 18 | 19/08/2014 | 15/10/2016 |
| | | DSS 45 | 3546 | 33 | 25/02/2015 | 08/10/2016 |
| | Madrid | DSS 54 | 3557 | 5 | 24/11/2014 | 09/10/2016 |
| | | DSS 55 | 3672 | 2 | 10/04/2015 | 08/10/2016 |
| | | DSS 63 | 9087 | 4 | 15/07/2014 | 16/10/2016 |
| | | DSS 65 | 2539 | 4 | 05/06/2015 | 21/09/2016 |
| ESA | Cebreros | DSA 83 | 13136 | 0 | 01/02/2015 | 28/08/2016 |
| | Malargue | DSA 84 | 36629 | 363[2] | 13/07/2014 | 15/10/2016 |
| | New Norcia | DSA 74 | 39521 | 5 | 10/07/2014 | 13/10/2016 |

Table 3-4 Summary of processed ΔDOR observables

| Type | Complex 1 | Complex 2 | Good | Ignored | Start | End |
|---|---|---|---|---|---|---|
| ΔDOR | Cebreros | Malargue | 7 | 0 | 24/07/2014 | 26/02/2016 |
| | Cebreros | New Norcia | 7 | 0 | 24/07/2014 | 24/02/2016 |

Raw range observables collected at ESTRACK stations are provided by ESOC FD in IFMS format, following the naming convention and structure defined in [13]. Observables collected at NASA's DSN antennae are provided in TDM format according to the definitions in [42].

As a first step, ranging data files were converted to Binary Object Archive (BOA) format, which is compatible with MONTE OD software, and merged to single files covering the different tracking passes.

Then, a series of data editing routines were performed as part of the pre-processing activities to include relevant a-priori information on the measurements or to calibrate known error sources.

[2] From July 2015, data collected at Malargue include PN range measurements, which systematically show offset values at the beginning of the tracking pass. As confirmed by ESOC FD, this behavior is due to errors within the data and not due to importing or processing procedures.

### 3.5.2 Range calibrations

The s/c geometrical range is defined as the distance between a reference point on the receiving/transmitting antenna, conventionally located at the intersection of the azimuth and elevation axes, and the phase center of the s/c antenna.

As described in 1.1.2, ranging observables are a measure of the signal propagation delay between the receiving and the transmitting electronics of the tracking stations, so any propagation delays between the electronic hardware and the respective reference points should be accounted for in the light-time solution and in the computation of ranging observables. These delays, which are schematically represented in Figure 3-5, are conventionally separated in the following components:

- S/C transponder delay: this term represents the round-trip delay between reception of the ranging signal at the phase center of the s/c HGA and its transmission back to earth. For Rosetta, the value of this delay was estimated during the early commissioning phases to be around $2.152\ \mu s$.[3]
- Station delay: this delay is the sum of the uplink delay from the transmitting electronics to the reference tracking point and of the downlink delay from the reference tracking point to the receiving electronics. This value is configuration-dependent (e.g. depends on the channel band and polarization) and is measured, using a test configuration, before (pre-calibration) or after (post-calibration) the tracking pass. However, these measured calibrations also include the delay due to the electronics and cabling of the calibration system hardware, which is not part of the actual ranging path during tracking. Furthermore, the path between the calibration system and the antenna reference point is not measured in the pre-calibrations. Both these effects are accounted for by applying a correction factor (z-height correction) to the measured pre-calibrations.
- Antenna correction: this correction is required for particular mounting configurations for which the azimuth and elevation axes do not cross. For these cases, the station reference point is not fixed with respect to the Earth and depends on the elevation.

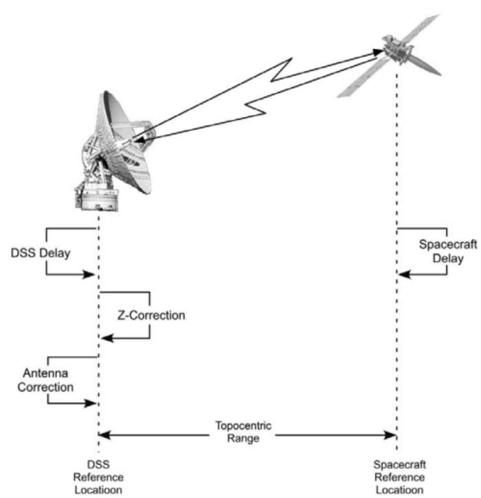


Figure 3-5 Range calibration scheme [43]

Station calibrations at each tracking pass are computed according to (3.10), where $\langle\Delta\rho_{obs}\rangle$ is the mean value of the unambiguous data points of the closest measured pre-calibration (or post-calibration when

[3] Personal communication with Frank Budnik (ESOC FD).

available) and $\Delta\rho_Z$ is the z-height correction for that particular station. Values for this correction at ESTRACK antennae are summarized in Table 3-5 for X/X tracking links.

DSN station calibrations are already accounted for within the TDM data files and no additional correction had to be applied.

$$\Delta\rho_{ST} = \langle\Delta\rho_{obs}\rangle + \Delta\rho_Z \tag{3.10}$$

Table 3-5 Z-height corrections for X/X tracking links at ESTRACK antennae

| Station | Correction |
|---|---|
| DSA 83 | -76.81 ns |
| DSA 84 | -70.71 ns |
| DSA 74 | -59.87 ns |

### 3.5.3 Media calibrations

Ionospheric calibrations were provided in form of monthly CSP cards [16] generated using GNSS dual-frequency measurements. These contain values for the total ionospheric delay at each tracking pass for the corresponding station of the ESTRACK and DSN complexes.

Tropospheric calibrations for DSN station complexes were similarly provided in form of monthly CSP cards from GNSS based measurements.

Tropospheric calibrations for ESTRACK complexes are computed for each tracking pass from IFMS atmospheric measurements collected by the local meteo station. Values for the ZHD and ZWD are estimated at the meteo station using the Saastamoinen model [19] and mapped to the height of the reference point for the antenna tracking station.

### 3.5.4 Solar Plasma

Another element that should be included within the model is the effect of charged particles from the solar corona on the propagation of radiometric signals. As a signal passes through the corona, free electrons in the plasma induce a group delay on the range and a phase advance on the Doppler measurements. This effect translates into increased noise levels for Doppler data and a variable bias in the range data, with magnitudes that can reach several hundred meters for low Sun-Earth-Probe (SEP) angles. Rosetta SEP angles during the proximity phase are shown in Figure 3-6, where we can see that the only solar conjunction (conventionally defined for $SEP < 10°$) occurs in the month of February 2015, with a minim SEP value of roughly 5°.

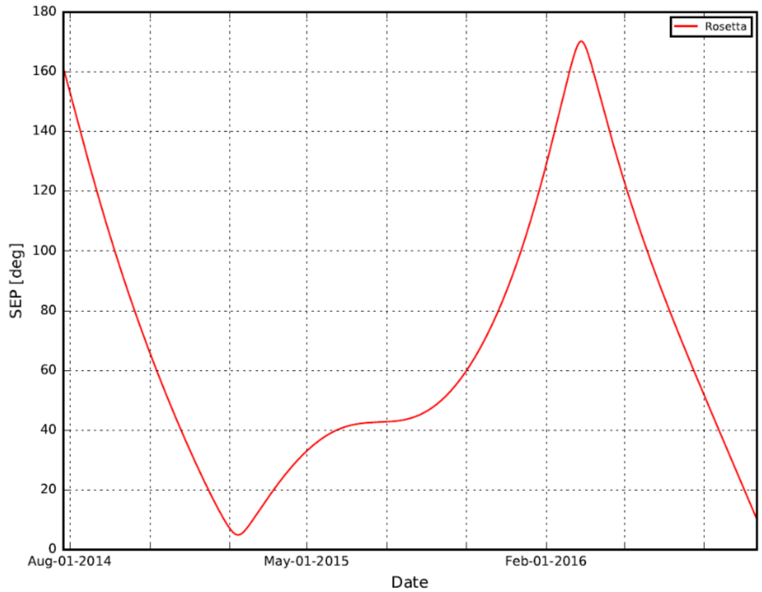


Figure 3-6 SEP angle during Rosetta's proximity phase

The expression that was used to model the two-way solar corona delay is the one described in [44] and shown in (3.11), where $c$ is the speed of light, $f$ is the frequency of the carrier signal, and the integration is carried out separately for the up-link and down-link contributions. The electron density distribution $N_e(r)$ is given in (3.12), where $r$ is the heliocentric distance, $R_\odot$ is the solar radius, and A and B are constant coefficients.

$$\Delta\rho_{cor} = \frac{40.3 \cdot 10^6}{cf^2}\left(\int_{r_1}^{r_2} N_e(r)\,dr + \int_{r_2}^{r_3} N_e(r)\,dr\right) \tag{3.11}$$

$$N_e(r) = A\left(\frac{r}{R_\odot}\right)^6 + B\left(\frac{r}{R_\odot}\right)^2 \tag{3.12}$$

As pointed out in previous studies, there is increasing evidence for a dependence of the electron density coefficients on the phase of the solar cycle [45], and on the heliocentric latitude, with local variations over active solar regions (CMEs and fast solar winds) [46]. For this reason, the coefficients A and B were estimated within the filter starting from the a-priori values determined for the 2006 Rosetta solar conjunction (see [45]) and using an a-priori uncertainty equal to the estimated a-priori value.

However, an initial assessment of the filter performances showed that the A coefficient could not be estimated with sufficient accuracy, possibly due to the relatively high SEP angles. For this reason, the contribution related to the A coefficient in (3.12) was neglected from the following analysis. The estimated value of $B = (7.52\ \pm 0.78) \cdot 10^5\ cm^{-3}$ for the final orbit reconstruction, which will be described in detail in Section 3.7.5, corresponds to a maximum range bias of $\Delta\rho_{SP} = (117 \pm 12)\ m$ during the solar conjunction of February 2015, as shown in Figure 3-7.

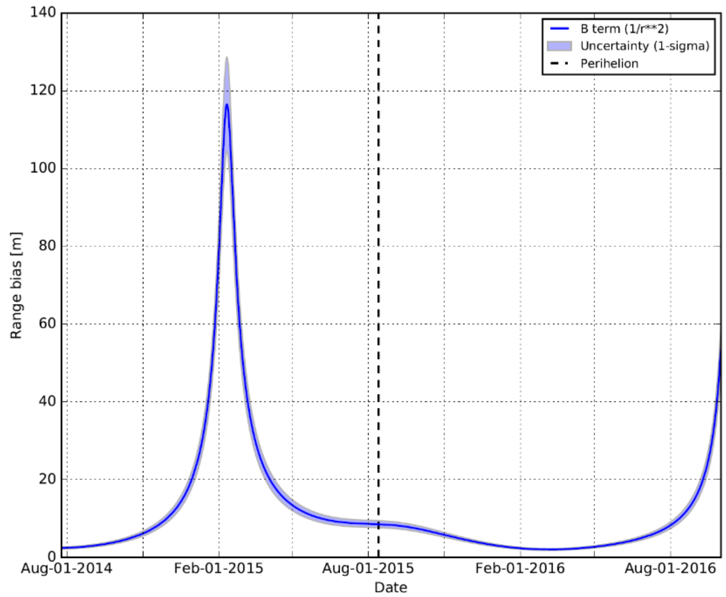

Figure 3-7 Estimated range bias due to the solar corona

### 3.5.5 Data reduction

Raw IFMS range measurements are provided at 1 Hz sampling frequency, while pre-processed TDM range data are provided with sampling intervals in the order of 250-300 s. To be consistent with TDM data and previous OD studies for Rosetta, IFMS measurements were reduced to 300 seconds intervals using a simple down-sampling procedure. This reduced dataset was used for the outlier removal procedure and for the initial model validation described in 3.5.6 and 3.5.8, respectively, while the final OD analysis was performed using the so called Normal Point (NP) measurements.

Reduction to normal points is a common practice for planetary ephemerides reconstruction (see for example [33] and [32]), and consists in reducing each tracking pass to a single range observable, which corresponded to the central range measurement for the current analysis. The standard deviation associated to the NP is the root square sum of the systematic (bias) and random (noise) errors. For the case of Rosetta, range biases represent the dominant contribution, with values in the order of 5-10 meters, as compared to the 50-70 cm noise values for a single arc. For this reason, a single measurement is considered to be representative of the whole pass. Smoothing of the dataset would only reduce the random component of the error by a factor of $\sqrt{N}$, where $N$ is the number of observables within the tracking pass. Since this component is negligible with respect to the bias, no smoothing was applied.

### 3.5.6 Removal of outliers

The pass-through described in 3.5.8 was used to perform a first inspection of the pre-fit residuals, to highlight the presence of signatures in the data and perform a manual removal of corrupted data points. After this first manual inspection, an automatic outlier removal procedure was performed through the following iterative process:

1. Mean value $\mu_{\mathrm{i}}$ and standard deviation $\sigma_{\mathrm{i}}$ of the valid post-fit range residuals are computed for the current iteration.
2. The maximum allowable deviation from the mean $\mu_{\mathrm{i}}$ is computed according to (3.13), where $N$ is the selected scale factor ($N = 5$ for the current analysis) and the factor $\pm\delta\sigma$ is used alternatively for residuals that are currently valid or discarded at the $i^{th}$ iteration (to avoid hysteresis). All residuals lying outside the intervals $[\mu_i \pm \Delta\rho_{max}]$ are then removed.

3. The first two steps are repeated until the current iteration produces no additional outliers or the maximum number of iterations is reached.

$$\Delta\rho_{max} = N\left(1 \pm \frac{\delta\sigma}{2}\right)\sigma_i \tag{3.13}$$

### 3.5.7 Data weights

When estimating the ephemeris of a target body that has been visited by a deep-space probe, the accuracy of the mapped range measurements, described in 3.2.2, depends on the magnitude of the uncalibrated range biases, on the accuracy of the relative orbit reconstruction between the probe and the target, and on the orbit geometry.

If the full covariance from the relative orbit reconstruction is known, formal uncertainties for the relative state vector can be mapped to the Earth LOS direction to obtain an initial guess for the range uncertainty. However, an estimation for the uncertainty of the relative orbit reconstruction could not be provided by ESOC FD, so an alternative weighting scheme had to be created.

A common approach for planetary orbiters is to define a single value for the weights of the mapped range measurements, which is consistent with the overall uncertainty of the relative orbit reconstruction over the period of interest. Typical values for two-way range weights vary between few meters and tens of meters depending on the mission profiles (see [33], [32], and [34]). Consistency with post-fit residuals is then checked to verify the soundness of the initial assumption. This approach works well for planetary orbiters, where the relative distance between the target and the probe is kept more or less constant for prolonged periods of time.

As shown in Figure 3-1, Rosetta's distance from the nucleus of comet 67P/CG varies up to three orders of magnitude during the course of the mission, significantly affecting the accuracy of the relative orbit reconstruction, which mostly relies on landmark optical measurements and Doppler data. As the s/c to comet distance increases, fewer landmarks can be identified, up to a point where it is not possible to resolve any surface feature and the optical navigation has to rely on Center-Of-Brightness (COB) measurements only (this distance corresponds to approximately 100 km for Rosetta[4]).

Another factor that can have a local influence on the accuracy of the relative orbit reconstruction is represented by the occasional anomalies observed in the AOCS system during the months around perihelion. As a consequence of the increased surface activity, the number of dust particles that were carried by the gas ejecta rose dramatically, degrading the performance of the star trackers (ST) with higher background signals and false star detections. Three ST failures were reported in correspondence of low-altitude flybys on February 14$^{th}$ [29] and 28$^{th}$ March [47], 2015, and May 28$^{th}$ [48], 2016 , during which the AOCS system had to rely solely on gyroscopes for several hours. During the March and May flybys, the prolonged duration of the anomalies induced the s/c to enter a Safe Mode, causing a risk for communication (and so mission) loss. It is difficult to assess the influence that these episodes might have on the accuracy of the orbit reconstruction by ESOC FD team, but a certain degree of degradation is expected around these periods.

For all these reasons, a different approach was employed for the definition of the mapped range measurement weights, which lies on the following assumptions:

- A lower limit for the LOS uncertainty of Rosetta's relative position is provided by the geocentric range discontinuities for comet 67P/CG, which are shown in Figure 3-8. This observation becomes evident when analyzing the initial pass-throughs generated using ESOC's ephemerides for both Rosetta and 67P/CG (see section 3.5.8). If the relative s/c position was accurately known, one would expect to

[4] Personal communication with Frank Budnik (ESOC FD)

observe the same discontinuities of Figure 3-8 in the pre-fit residuals. However, these features are not observed at the corresponding time-tags, suggesting that the geocentric range discontinuities for 67P/CG are compensated for by equal and opposite discontinuities in the s/c to comet relative geocentric range. This can only occur if the LOS uncertainty of the s/c relative position has a value that is comparable with the magnitude of the observed jumps.

- A constraint for the uncertainty of Rosetta's relative position for the months of September and October 2014 is provided by the long-arc OD solution in Figure 11 from [49]. Formal state covariances (3σ) are provided as a function of time for the RTN cometocentric frame. A conservative value for the 1σ uncertainty in the Earth LOS direction can be retrieved by selecting a reference comet distance and taking the highest component of the uncertainty in RTN frame.

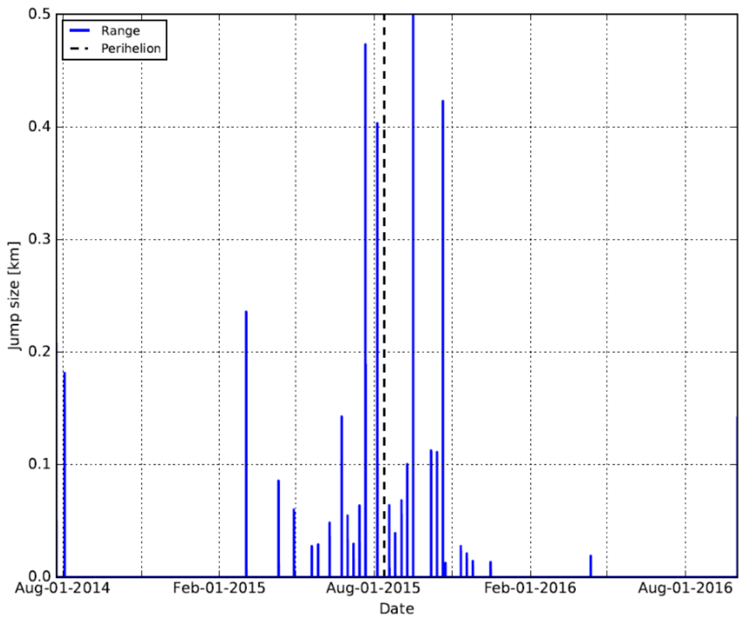


Figure 3-8 Geocentric range discontinuities for the reconstructed orbit of comet 67P (ESOC solution)

Then, we assumed to scale the one-way weight at different times only as a function of the cometocentric distance. Based on this assumption, the one-way range weights as a function of the s/c cometocentric distance at the time of observation are defined as in (3.14), where $R_{ref} = 10\ km$ is the reference distance corresponding to the s/c position uncertainty of $w_{min} = 5\ m$ from [49], $R_{max} = 1500\ km$ is the maximum s/c distance during the tail far excursion, and $w_{max} = 500\ m$ is the corresponding geocentric range discontinuity for comet 67P-CG.

Two-way range weights are then derived by simply doubling the one-way values.

$$w(R) = \begin{cases} w_{min} & R < R_{ref} \\ w_{max} + (w_{min} - w_{max}) \left[ \dfrac{(R/R_{max} - 1)}{(R_{ref}/R_{max} - 1)} \right]^k & for \quad R_{ref} \leq R \leq R_{max} \\ w_{max}\ (R/R_{max} - 1)^k & R \geq R_{max} \end{cases} \qquad (3.14)$$

According to (3.14), the selected weights depend on the assumed value for the exponential parameter $k$, which is varied as part of a sensitivity analysis in the following sections. Two-way Range weights as a function of time are shown in Figure 3-9 for the three alternative values of $k \in [0.5, 1, 2]$. As it can be seen from the figure, the weight varies between the same $w_{min}$ and $w_{max}$ when the distance changes, but at different rates (highest for $k = 2$, lowest for $k = 0.5$).

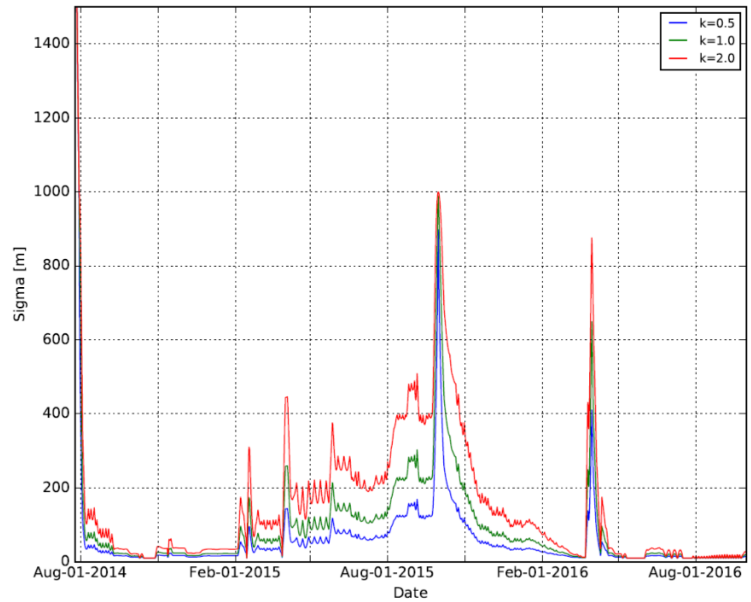


Figure 3-9 Two-way range weights as a function of time for three alternative values of the parameter k.

#### *3.5.7.1 ΔDOR measurements*

Uncertainties for the 1-way spacecraft and quasar VLBI measurement are included within the measurement files provided by ESOC and represent an output of the cross-correlator.

Uncertainties in the differenced ΔDOR measurements for the selected QSQ configuration (see 1.1.4.2) are computed according to (3.15), where $\sigma_{SC}$ is the uncertainty for the s/c VLBI measurement, and $\sigma_{Q-int}$ is the interpolated value of the quasar VLBI measurement uncertainty.

$$\sigma_{\Delta DOR} = \sqrt{\sigma_{SC}^2 + \sigma_{Q-int}^2} \tag{3.15}$$

Since the ΔDOR measurements are applied to the mapped comet state, instead of the s/c itself, the uncertainties computed in (3.15) can be used only if the relative orbit uncertainty in correspondence of the ΔDOR data is at least one order of magnitude smaller than the measurements uncertainties. A rough estimation of the Plane-Of-the-Sky (POS) position uncertainty $\sigma_{POS}$ as a function of the geocentric distance is given in (3.16), where $c$ is the speed of light, $B$ is the baseline distance between the two DOR receivers, and $\rho_{\oplus}(t)$ is the geocentric distance of the target at time t.

$$\sigma_{POS} \approx \frac{c \cdot \sigma_{\Delta DOR}}{B} \rho_{\oplus}(t) \tag{3.16}$$

The ΔDOR measurements used for this analysis are collected at the end of July 2014 and February 2016, when Rosetta is at geocentric distances of 2.7 AU and 1.5 AU, as shown in Figure 3-10. For the Cebreros/New-Norcia baseline $B_{CEB-NNO} = 11625\ km$, a ΔDOR uncertainty of $\sigma_{\Delta DOR} = 0.5\ ns$ corresponds to approximate values for the POS uncertainties of 5.2 km and 2.9 km for July 2014 and February 2016, respectively. In an analogous way, the Cebreros-Malargue baseline $B_{CEB-MAL} = 9511\ km$ gives approximate POS uncertainties of 6.4 km and 3.5 km.

These values are several orders of magnitude larger than the relative s/c uncertainty for the measurements taken in February 2016, when Rosetta in in close proximity to the comet. However, this is not the case for July 2014, when Rosetta is significantly far away from the comet, and the relative state uncertainty is probably in the order of several hundred meters or even a few kilometers.

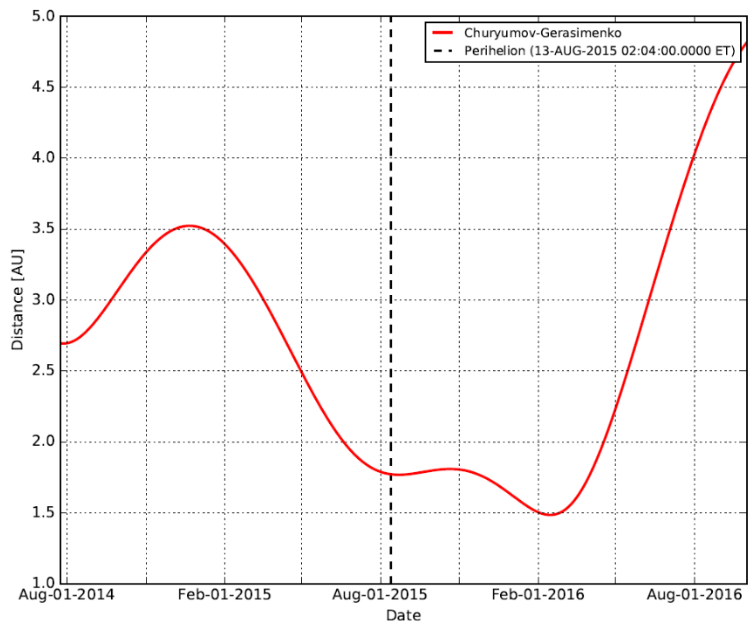


Figure 3-10 Comet geocentric distance during Rosetta's proximity phase

The ΔDOR measurements for this period were therefore de-weighted to be consistent with the assumed 1-way range uncertainty modelled in (3.14) and considering a value of $k = 0.5$ for the exponential factor. To compute the new weights, the 1-way range uncertainty was expressed in seconds and summed in quadrature with the original ΔDOR measurement uncertainty. Original ΔDOR uncertainties, derived from the correlator, and the corresponding augmented values for the July 2014 measurements are shown in Figure 3-11.

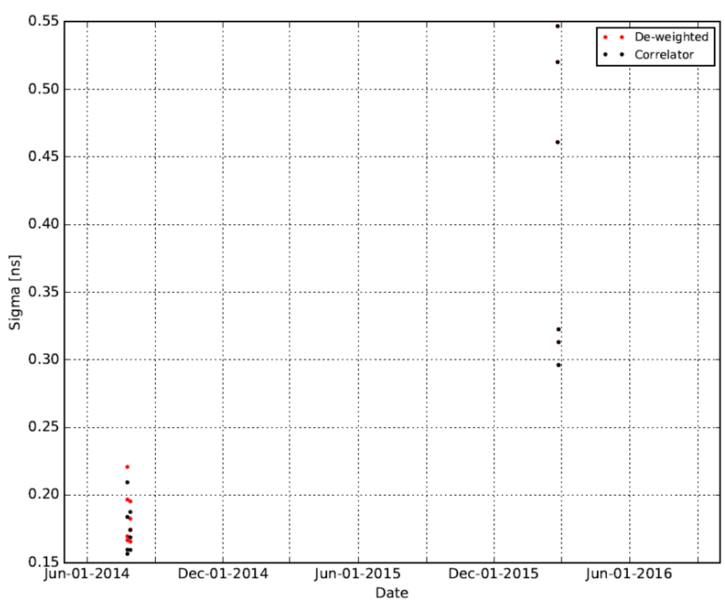


Figure 3-11 Original and modified ΔDOR uncertainties.

### 3.5.8 Model validation

To validate the data pre-processing and the measurement models, an initial OD run with a simplified filter setup is performed covering the time between the 3rd September and 28th October 2014, corresponding to the period of the long-arc OD solution derived in [49]. The rationale behind this procedure is that by using the ESOC OD solution as input and the same filter setup, similar results should be obtained in terms of range residuals and estimated parameters values.

The following setup was used for this analysis:

- The heliocentric trajectories of Rosetta and comet 67P/CG are taken from the latest orbit reconstruction from ESOC FD (see Table 3-2). Figure 3-12 shows the s/c relative trajectory in the EMO2000 reference frame and the s/c cometocentric distance for the analyzed time period.
- DE405 planetary ephemerides are used, instead of the most recent DE438, consistently with the ones used to generate the ESOC solution.
- Range measurements for DSN stations are imported from TDM files, while measurements for ESTRACK stations are derived from IFMS files and reduced to 300 s sampling intervals. Pre-processing procedures are the ones described in section 3.5.2 through 3.5.6 (no reduction to NP is performed).
- Initial a-priori range weights are computed with noise models developed in the framework of the ASTRA study [3]. After a first iteration, refined range weights for each tracking pass are computed as the mean RMS value of the post-fit residuals for that pass.
- A range bias per station per pass is included in the model and solved-for within the filter. A-priori values for these biases are set to zero with uncertainties of 10 m.

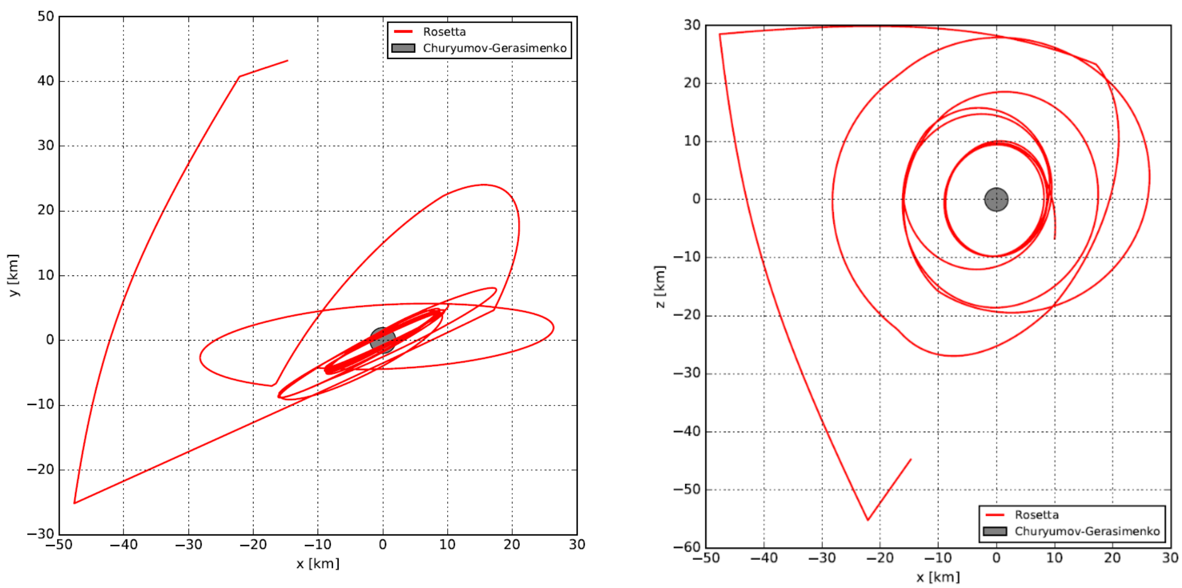

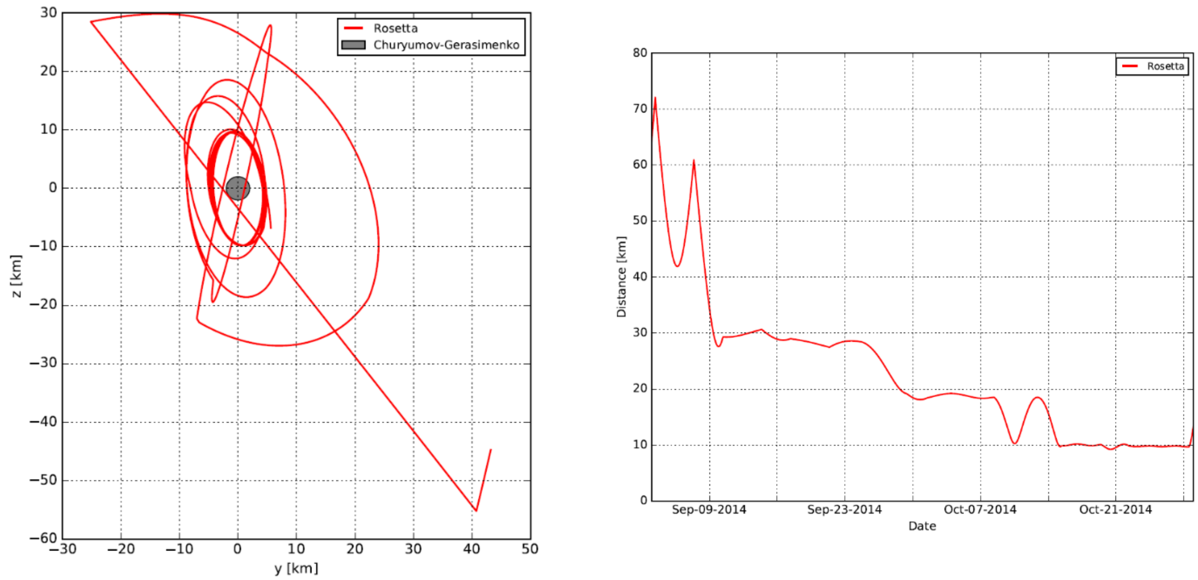


Figure 3-12 Rosetta's cometocentric trajectory in EMO2000 reference frame (top, bottom left) and cometocentric distance (bottom right) between the 3rd September and 28th October 2014.

Figure 3-13, which shows the obtained post-fit residuals for the current OD setup, is compared with the post-fit residuals from [49], which are reported in Figure 3-14. We can see that the overall RMS values for the post-fit residuals are consistent between the two analyses. Only a small difference of roughly 15 $cm$ can be observed between the two, which is mostly due to the different sampling times between the range observables. The DSN measurements, which have a lower uncertainty with respect to the ESTRACK ones, have a higher impact on the RMS value for the analysis of [49], where the ESTRACK sampling time was kept lower (resulting in fewer points).

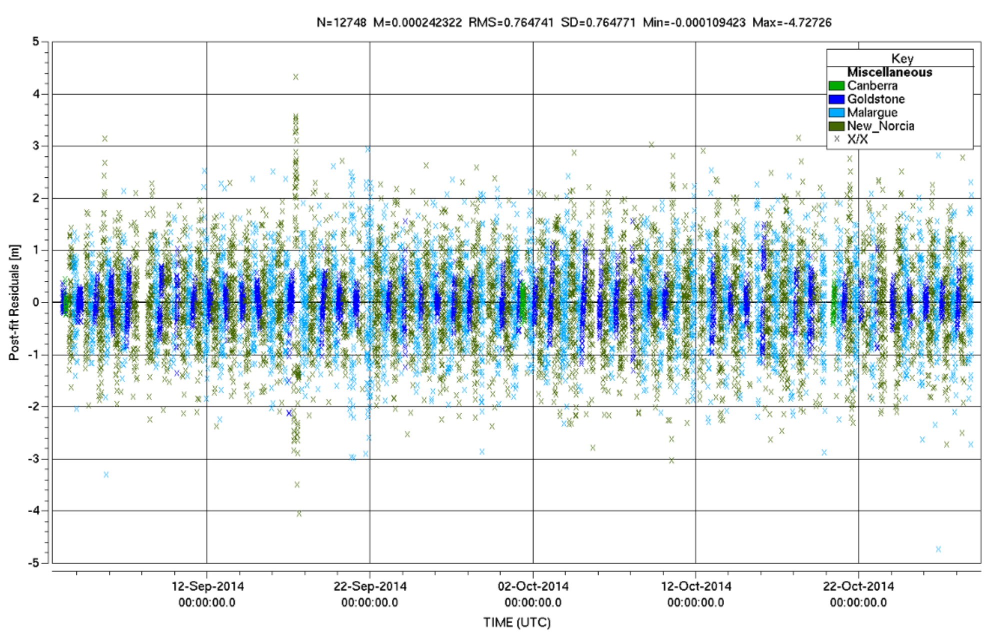


Figure 3-13 Two-way range post-fit residuals

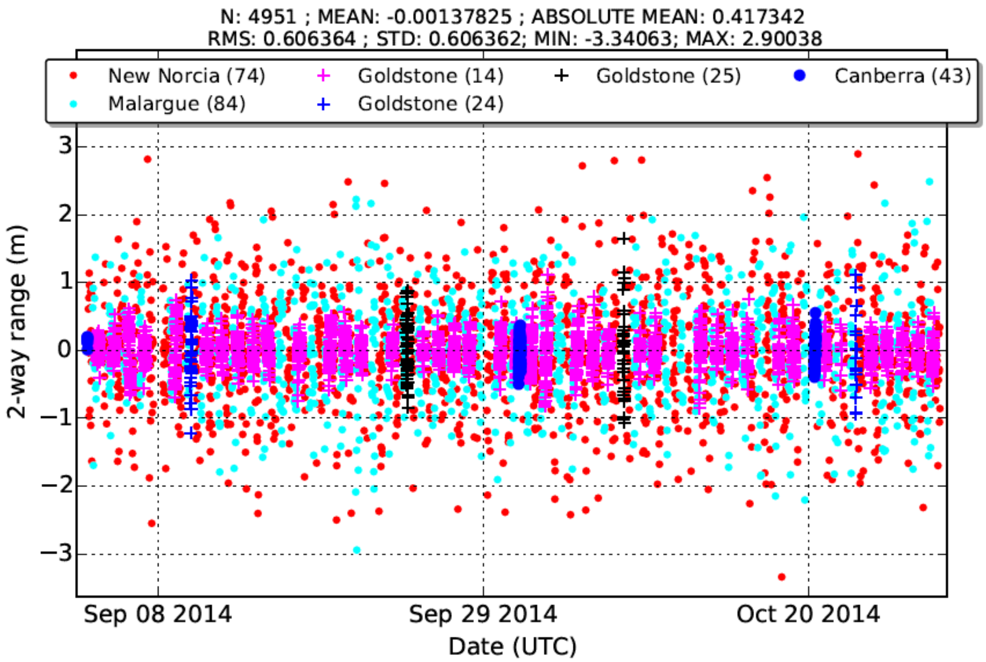


Figure 3-14 Two-way range post-fit residuals from [49]

Figure 3-15, shows a comparison of the estimated one-way station biases, per station, per pass, for the relevant ESTRACK and DSN complexes. We can see that the current estimated values (right figure) are perfectly consistent with previous estimation (left figure), confirming the overall consistency of the setup.

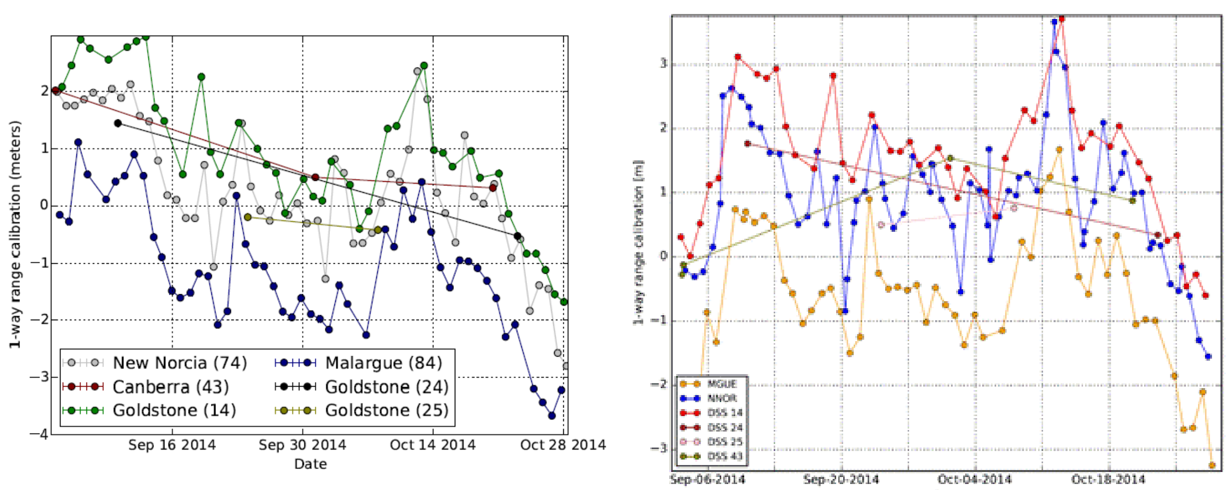


Figure 3-15 Estimated 1-way range biases, per station per pass (right figure) vs estimated values from [49] (left figure).

After validation of the data processing and filter setup, a pass-through was performed for monthly arcs covering the whole mission duration, in an effort to highlight inconsistencies in the processed datasets and perform a manual removal of the outliers. From the whole set of arcs, only the months of July and August 2015 are shown here, since they allow to highlight relevant information for the OD setup.

Figure 3-16 shows the pre-fit residuals for July 2015, corresponding to a period of intense surface activity. If we look at the geocentric range discontinuities for comet 67P/CG (see Figure 3-8), we would expect to find at least one major discontinuity in the Rosetta pre-fit residuals, with an order of magnitude of roughly 800 m for the two-way range. The expected discontinuity is not present in the pre-fit residuals of Figure

3-16, where only a small 6 m gap is observed at the corresponding time-tag. This supports the assumption that, during the operational OD reconstruction, comet discontinuities in the Earth LOS direction have been absorbed by equal and opposite discontinuities in the relative orbit of Rosetta around the comet. As pointed out in 3.5.7, this also means that the uncertainty in the relative orbit reconstruction for the corresponding interval should have at least the same order of magnitude of the one-way range discontinuities from Figure 3-8 (if not higher). This observation was therefore critical during the definition of the weighting scheme since it provided a lower limit for the relative orbit uncertainty during the period of maximum comet activity, where no other indication is available from literature.

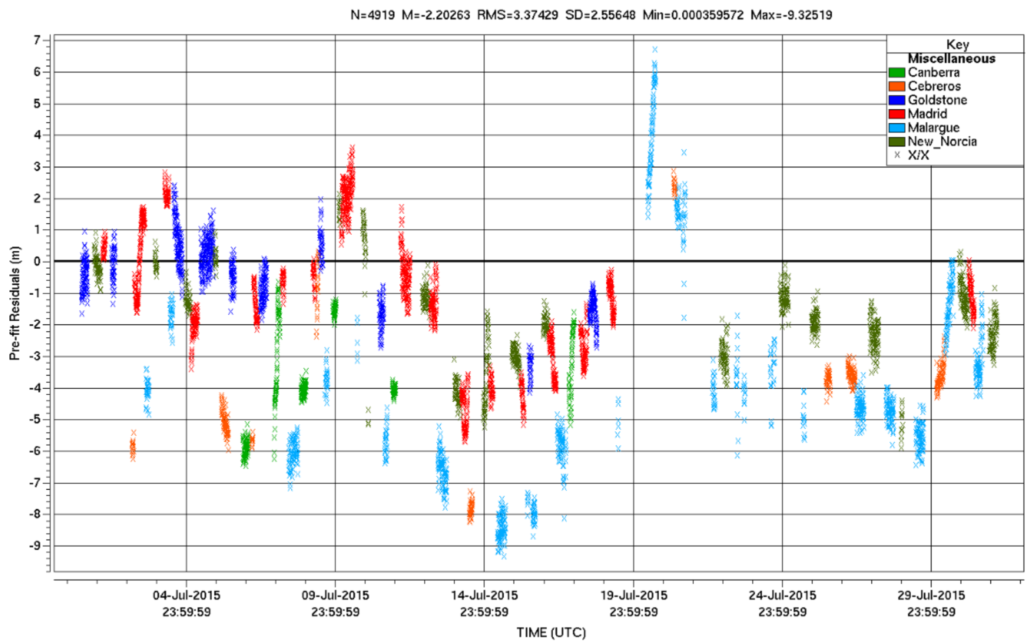


Figure 3-16 Pre-fit range residuals for July 2015

Figure 3-17 shows the pre-fit residuals for August 2015. It can be observed that starting from the $26^{th}$, a few tracking passes collected at Malargue show a range bias of roughly 25 meters with respect to the other stations. Further inspection of the IFMS input files showed that these measurements corresponded to PN range data, which started to gradually replace the sequential range, before becoming the only measurement type collected at Malargue after September of the same year. This transition did not represent an issue, per se, since PN range measurements can be converted to MONTE BOA format with only minor modifications to the IFMS processing procedures. However, the observed range bias needs to be included in the observation model and estimated within the filter.

A possible explanation for this modelling error could be related to the use of a different onboard transponder for the PN range with respect to the tone/code case. Nonetheless, the estimation of a single range bias to account for the uncalibrated transponder delay was not successful, with the pre-fit residuals showing a linear-like drift for the PN measurements over the period between August 2015 and September 2016, possibly indicating an error in the calibration procedures after the PN range transition.

To mitigate the effect of this variable station bias, a duplicate for the Malargue complex was introduced within the MONTE OD setup and used exclusively to model the PN range data. Range biases per arc (each having a duration of one month) were estimated separately for this station (referred to as MGPN) using a higher value for the a-priori uncertainty.

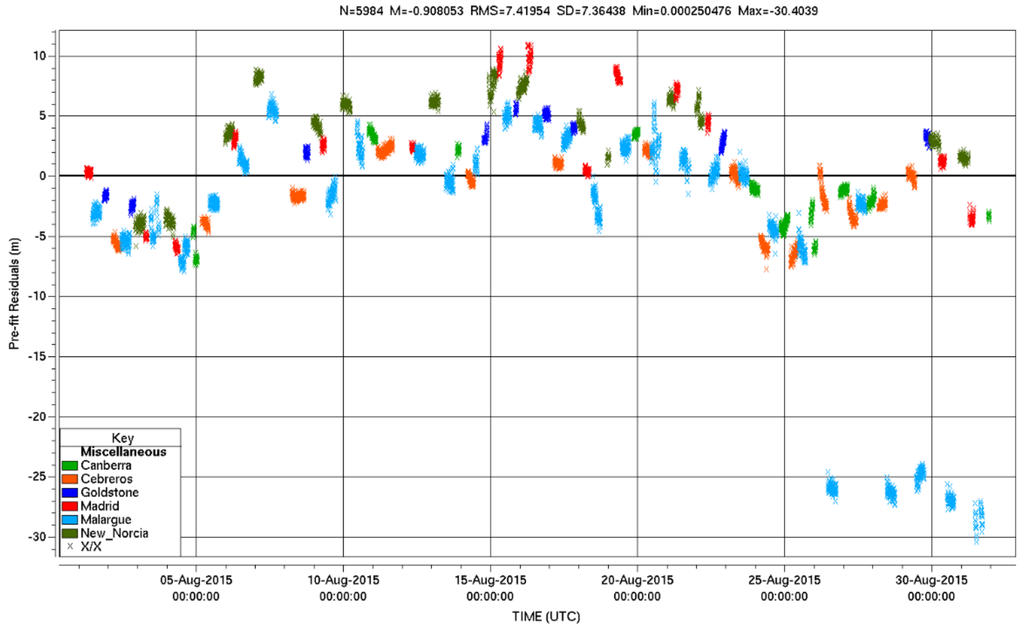


Figure 3-17 Pre-fit range residuals for August 2015

## 3.6 Filter setup

Several test cases were analyzed as part of the OD process by varying the selected model for the NGA representation, the a-priori uncertainties for the estimated parameters, and additional constraints to the estimated values. Table 3-6 summarizes the estimated parameters that are common to all the analyzed test cases. Additional solve-for parameters, specific for each NGA model, will be described in the following sections.

A-priori values for the comet's state are taken from the heliocentric trajectory from ESOC FD, while a-priori uncertainties represent conservative guesses.

Considering the slow variation of the range biases observed for PN range measurements (see 3.5.8), a single offset value is estimated locally for each filter arc, corresponding to a duration of 1 month. Therefore, a total of 14 range biases (one for each arc that includes PN measurements) are solved-for within the filter. A-priori values are computed as the average offset from the single arc pass-through solutions, while the a-priori uncertainty represents an upper limit to the standard deviation for the same solutions.

Table 3-6 Common estimated parameters within the OD filter and associated a-priori uncertainties

| **Parameter** | $N_{est}$ | **A-priori uncertainty** | **Notes** |
|---|---|---|---|
| Comet position | 3 | $10^4\ km$ | Reference values are taken from ESOC's solution at 1st August 2015. |
| Comet velocity | 3 | $100\ m/s$ | |
| MGUE PN bias | 14 | $10\ m$ | A-priori values from pass-through using ESOC solution. Uncertainty represents an upper limit to standard deviation of pass-through residuals |
| Solar plasma (B) | 1 | $4.1 \cdot 10^5\ cm^{-3}$ | A-priori uncertainty corresponds to the a-priori value (from [48]) |

## 3.7 Results

Several test cases were analyzed as part of the OD process by:

1. Varying the data weights through the parameter $k$ described in (3.14). It should be noted that a preliminary sensitivity analysis led to the selection of $k = 0.5$ for the weighting scheme, so all results presented hereafter are obtained using this value.
2. Changing the model to represent the NGA due to comet outgassing. Both global and stochastic models will be explored.
3. Changing a-priori values and uncertainties for the estimated parameters related to NGA modelling.
4. Changing parameters related to the stochastic interval definition or constraints between successive stochastic solutions (when applicable).

To evaluate the ability of a given model to fit the observed data, we used an approach similar to the one employed in [39], which relies on the evaluation of the reduced chi-square statistics. Out of the proposed test cases, only the ones for which $\chi_\nu^2 \cong 1$ are retained for further analysis.

### 3.7.1 Approach for the model selection

The chi-square ($\chi^2$) and reduced chi-square ($\chi_\nu^2$) statistics for the post-fit residuals are defined according to (3.17) and (3.18), where $N_{obs} = 2766$ is the total number of observables (assuming all range and ΔDOR measurements are used), $\sigma_i$ is the weight assigned to the residual $R_i$, and $\nu$ represents the degrees of freedom (DOF) in the estimation process, corresponding to $\nu = N_{obs} - N_{est}$, where $N_{est}$ is the number of estimated parameters.

$$\chi^2 = \sum_{i=1}^{N_{obs}} \frac{R_i^2}{\sigma_i^2} \tag{3.17}$$

$$\chi_\nu^2 = \frac{\chi^2}{\nu} \tag{3.18}$$

If we assume a perfect knowledge of the measurement errors, the following scenarios are possible:

- $\chi_\nu^2 \gg 1$: the model produces a poor fit and is not adequate to describe the system.
- $\chi_\nu^2 \sim 1$: the model is able to fit the data to a level which is consistent with the error variance.
- $\chi_\nu^2 < 1$: the model is “over-fitting” the data and should be adjusted.

However, since the error covariance is not known a-priori and heavily relies on the assumptions described in 3.5.7, values of $\chi_\nu^2$ slightly higher or lower than 1 could also mean that the variance has been poorly estimated. For this reason, a sensitivity analysis has been performed by running the OD filters with three different values of the factor $k$ which determines the observables’ weight.

### 3.7.2 Global NGA models

#### *3.7.2.1 Standard Model (SM)*

The first model to be evaluated is the SM, which represents a baseline for the dynamics of active cometary nuclei. Several test cases were explored by considering different power laws for the sublimation rate $g(r)$ and by including specific acceleration components in the heliocentric RTN frame.

Table 3-7 summarizes the statistics of the postfit residuals for the considered test cases, along with the estimated values of the model parameters. Formal uncertainties for the estimated parameters are not reported here since they are considered unreliable (due to the poor model fit).

It can be observed that by increasing the exponential factor from the original value proposed by Mardsen, both the post-fit residuals and the reduced chi-square values are reduced, in agreement with the assumption that the outgassing activity of comet 67P/CG is best approximated by an $r^{-5}$ power law ( [43], [32] ).

It should also be noted that adding an out-of-plane component to the estimated acceleration vector does not produce an improvement to the solution. Although, the reduced chi-square value is slightly reduced, the RMS values of both range and ΔDOR residuals are increased. Moreover, the estimated normal component of the acceleration is an order of magnitude higher then the radial and tangential components, contrarily to what is observed for most of the short-period comets is literature.

Table 3-7 Summary of postfit residual statistics and estimated parameters for the SM

| Case | Acc. | $k$ | $RMS_{range}$ $[m]$ | $RMS_{\Delta DOR}$ $[ns]$ | $\chi_\nu^2$ | $A_i$ $[10^{-8}\ m/s^2]$ |
|---|---|---|---|---|---|---|
| 1 | RT | 2.15 | $7.2715 \cdot 10^4$ | 44.81 | $2.507 \cdot 10^6$ | $[2.435, 0.239]$ |
| 2 | | 3 | $5.4936 \cdot 10^4$ | 44.53 | $1.427 \cdot 10^6$ | $[2.856, 0.343]$ |
| 3 | | 4 | $4.2582 \cdot 10^4$ | 44.23 | $8.229 \cdot 10^5$ | $[3.528, 0.497]$ |
| 4 | | 5 | $3.5089 \cdot 10^4$ | 43.30 | $5.266 \cdot 10^5$ | $[4.429, 0.695]$ |
| 5 | RTN | 5 | $3.9069 \cdot 10^4$ | 64.79 | $3.898 \cdot 10^5$ | $[2.535, 0.587, 15.910]$ |

Figure 3-18 and Figure 3-19 show, respectively, the post-fit residuals and weighted post-fit residuals of the reference filter solution for the SM, corresponding to Case 4 described Table 3-7. It is evident from these plots that the SM is not adequate to describe the motion of 67P/CG.

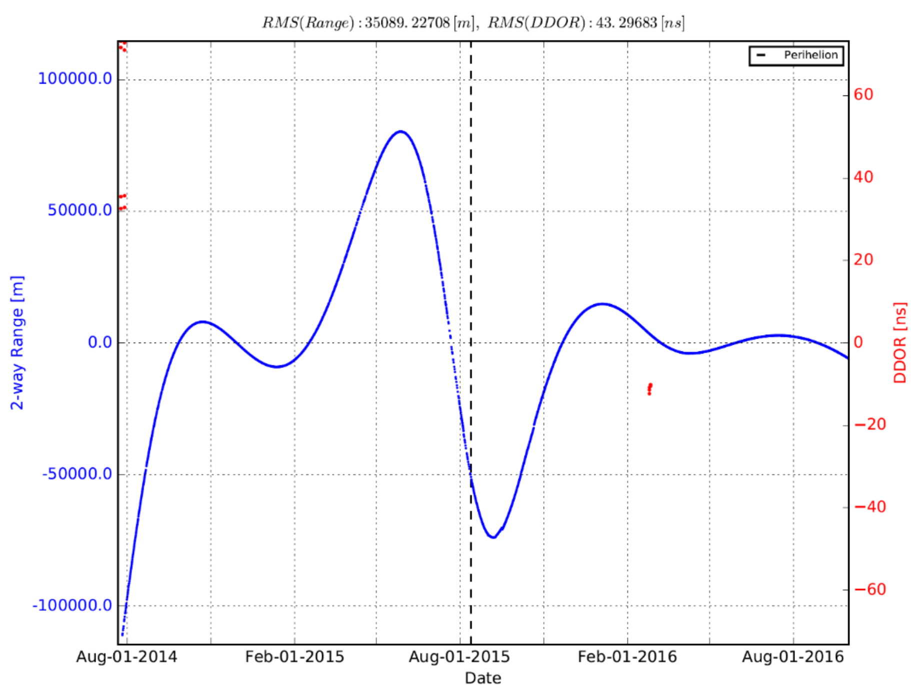


Figure 3-18 Post-fit residuals and statistics for the SM (Case 4).

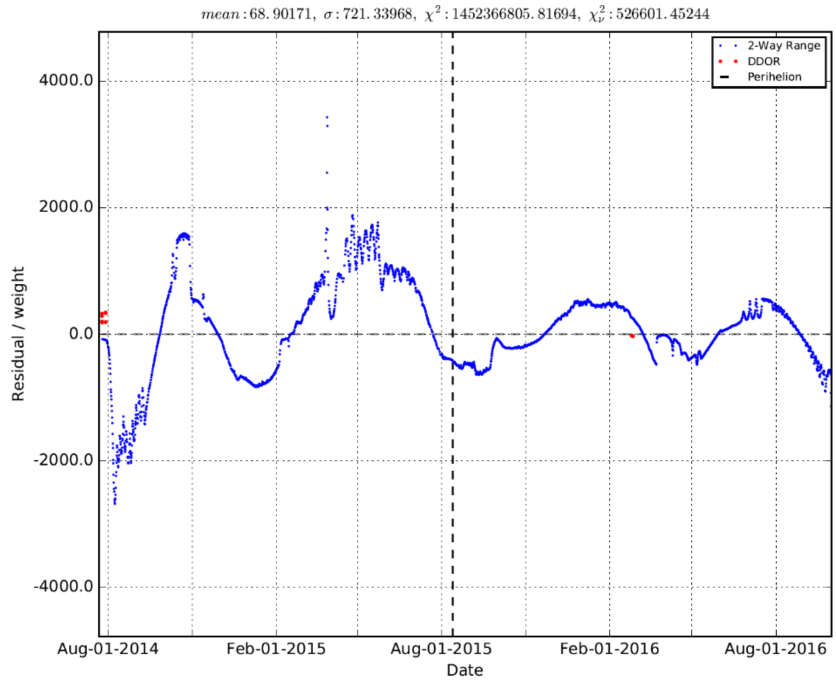

Figure 3-19 Weighted post-fit residuals and chi-square statistics for the SM (Case 4)

#### *3.7.2.2 Extended Standard Model (ESM)*

The second model to be evaluated is the ESM, which introduces a variable time offset $\Delta T$ between the perihelion and the peak of the comet's water-vaporization curve. To implement this model, we followed the formulation in [41], which allows to estimate the time offset $\Delta T$. Since the comet state and its partials are only known for previous times steps, when integrating the comet's trajectory the partial derivatives of $g(r')$ with respect to the comet's position $\partial r'/\partial \vec{r}$ and velocity $\partial r'/\partial \vec{v}$ are determined at each integration step using a two-body trajectory and the osculating orbital elements corresponding to the integration time $t$. This approach, which simplifies the mathematical formulation for the differential corrector, is justified by the observation that estimated time offsets are often small, in the order of a few weeks. For this particular case, the time offset was estimated to have a magnitude in the order of $\Delta\mathrm{T}{\sim}30\ days$, which is consistent with Earth-based photometric and astrometric measurements (see [40] and [31]).

Table 3-8 summarizes the statistics of the postfit residuals for the considered test cases, along with the estimated values of the model parameters. It can be seen that the introduction of a time offset allows to reduce both the RMS of the residuals and the reduced chi-square values with respect to the SM. Similarly to the SM, we can observe a significant reduction in the RMS of the residuals with an increase of the power-law exponential factor for the sublimation rate, which incidentally corresponds to a reduced value for the estimated time offset $\Delta T$. Adding the out-of-plane component to the estimated acceleration vector (Case 5) has the effect of increasing the RMS of the postfit residuals (even though the $\chi^2_\nu$ value is slightly reduced). Furthermore, the estimated value for the normal acceleration component is still higher than the radial one, suggesting that this might represent a not-physical solution. Formal uncertainties for the estimated parameters are not reported here since they are considered unreliable (due to the poor model fit).

Table 3-8 Summary of postfit residual statistics and estimated parameters for the ESM

| Case | Acc. | $k$ | $RMS_{range}\ [m]$ | $RMS_{\Delta DOR}\ [ns]$ | $\chi_v^2$ | $A_i\ [10^{-8}\ m/s^2]$ | $\Delta T[d]$ |
|---|---|---|---|---|---|---|---|
| 1 | RT | 2.15 | $5.8714 \cdot 10^4$ | 51.48 | $1.501 \cdot 10^6$ | $[2.646, -0.195]$ | 34.01 |
| 2 | | 3 | $4.0914 \cdot 10^4$ | 30.31 | $7.563 \cdot 10^5$ | $[3.094, -0.128]$ | 29.77 |
| 3 | | 4 | $2.7827 \cdot 10^4$ | 17.85 | $3.529 \cdot 10^5$ | $[3.818, -0.049]$ | 26.46 |
| 4 | | 5 | $1.9077 \cdot 10^4$ | 12.37 | $1.641 \cdot 10^5$ | $[4.793, 0.040]$ | 24.25 |
| 5 | RTN | 5 | $2.1290 \cdot 10^4$ | 22.07 | $1.589 \cdot 10^5$ | $[4.343, -0.137, 5.171]$ | 33.13 |

Figure 3-20 and Figure 3-21 show, respectively, the post-fit residuals and weighted post-fit residuals of the reference filter solution for the ESM, corresponding to Case 4 described Table 3-8. These plots clearly indicate that the ESM is not adequate to describe the motion of 67P/CG.

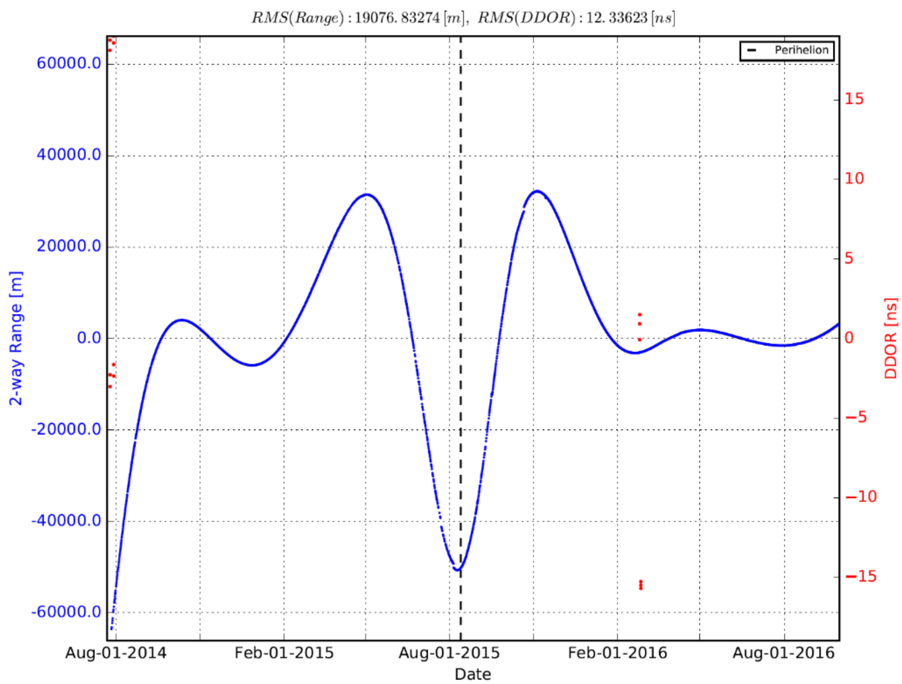

Figure 3-20 Post-fit residuals and statistics for the for the ESM (Case 4).

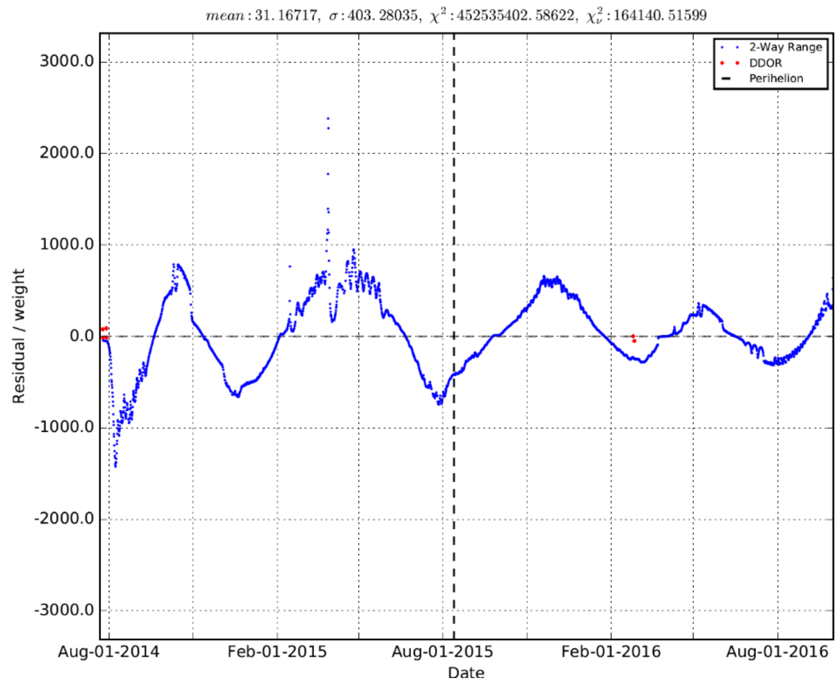


Figure 3-21 Weighted post-fit residuals and chi-square statistics for the for the ESM (Case 4).

#### *3.7.2.3 Rotating Jet Model (RJM)*

The RJM is a higher fidelity model with respect to the ESM and depends on several additional parameters, some of which may be hard to reliably estimate. For this reason, it was decided to rely on a few assumptions and previous characterizations of the dynamical environment of 67P/CG to restrict the parameter space:

- The orientation of the spin axis of the comet has been measured over the course of the Rosetta mission, with its North pole having almost constant values for the $RA = 69°$ and $DEC = 65°$ in the EME2000 reference frame. These values were kept constant and not estimated within the filter.
- In agreement with the observations made for the SM and ESM, a power law of the type $g(r) \sim r^{-5}$ was adopted to model the water isothermal sublimation rate.
- Only two jets are included within the model, one in the northern and one in the southern hemisphere. Each of the two jets captures the overall outgassing of their respective hemisphere averaged over a single comet rotation.

To narrow down possible value for the system parameters, we initially performed a broad grid search by varying the colatitude of the two jets (i.e. the angle that they form with the North pole) and the diurnal lag angle with constant steps of length $\delta\eta = 10°$ and $\delta\Delta\theta = 5°$, respectively. For this initial grid search, the time offset between the perihelion and the peak of outgassing activity was kept constant at $\Delta T \cong 24\ days$, which corresponds to the estimated value for the ESM reference case. The only parameters which were estimated for each filter run were the comet state at perihelion and the intrinsic strength of the jets $A_i$.

Figure 3-22 shows the reduced chi-square value of the postfit residuals as a function of the jets' colatitude using a color-coded logarithmic scale. Only the 2D grids corresponding to diurnal lag angles of $10°$ (left figure) and $15°$ (right figure) are reported here, which represent the ones producing minimum $\chi^2_\nu$ values.

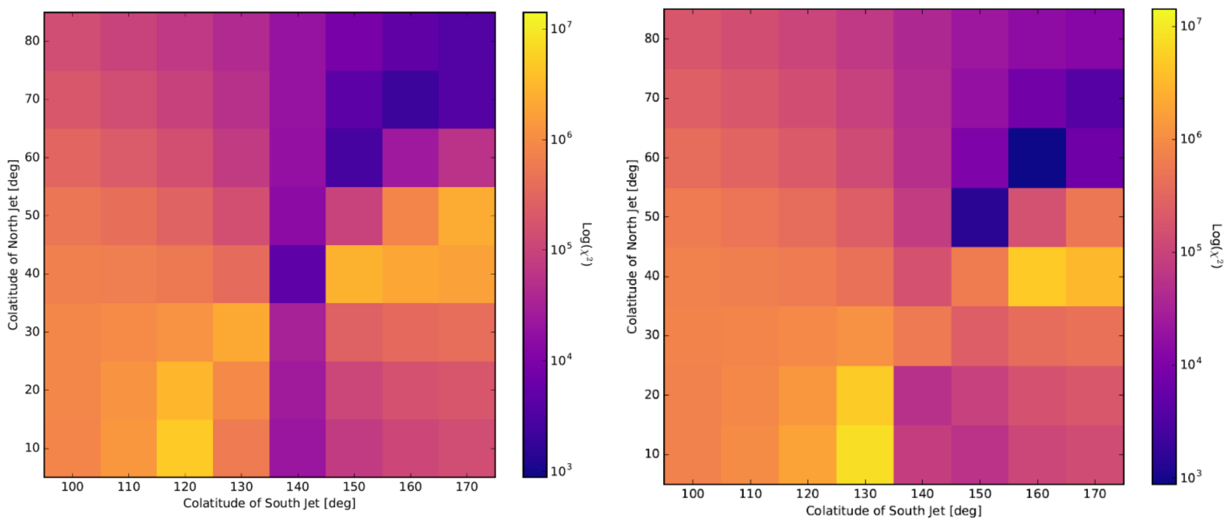


Figure 3-22 Reduced chi-square values of postfit residuals for the initial broad grid search.

A second grid search was then performed by restricting to colatitudes in the intervals $[40°, 80°]$ and $[130°, 170°]$, respectively for the North and South jets. In addition to the comet state and the jet strength, both the time offset of peak activity and the diurnal lag angle were estimated within the filter starting from a-priori values of $\Delta T \cong 24\ \pm 5\ days$ and $\Delta\theta = 15° \pm 5°$.

Figure 3-23 shows the reduced chi-square statistics for this second grid search. The solution providing the minimum $\chi_\nu^2$ value, corresponding to colatitudes of $45°$ and $140°$, was then used to perform a final filter run with the estimation of all parameters for the RJM including the jets' colatitudes, which are poorly observable due to the complex formulation for $J_S$ and $J_P$ (see [33]).

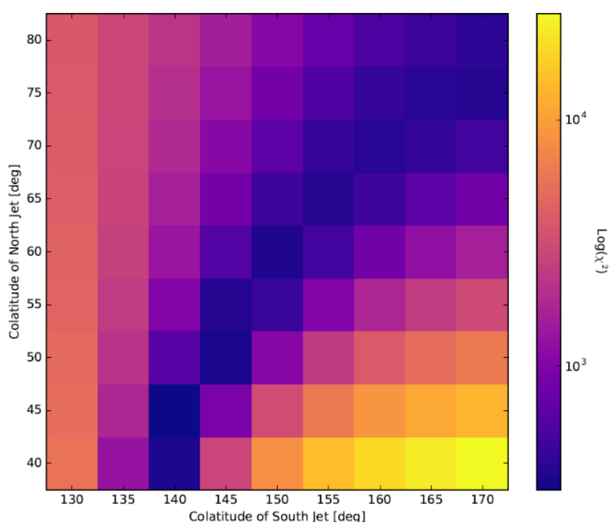


Figure 3-23 Reduced chi-square values of postfit residuals for the fine grid search

Table 3-9 summarizes the a-priori and estimated values for the model parameters of the converged filter solution. It is interesting to note that most of the estimated parameters are more or less compatible with the ones estimated in [32], with the exception of the diurnal lag angle, which is significantly smaller for the current analysis. Similarly to the SM and ESM cases, formal uncertainties for the estimated parameters are not reported here since they are not considered reliable (due to the poor model fit).

Table 3-9 A-priori and estimated parameters for the converged solution using the RJM

| Parameter | A-priori | Estimated |
|---|---|---|
| $A_N$ | $(5.26 \pm 2) \cdot 10^{-8} AU/d^2$ | $6.52 \cdot 10^{-8} AU/d^2$ |
| $A_S$ | $(4.59 \pm 2) \cdot 10^{-8} AU/d^2$ | $4.72 \cdot 10^{-8} AU/d^2$ |
| $\eta_N$ | $(45 \pm 5)°$ | $38.62°$ |
| $\eta_S$ | $(140 \pm 5)°$ | $138.34°$ |
| $\Delta T$ | $(20.03 \pm 5)\ d$ | $19.5\ d$ |
| $\Delta\theta$ | $(10.46 \pm 5)°$ | $10.2°$ |

Figure 3-24 and Figure 3-25 show, respectively, the post-fit residuals and weighted post-fit residuals of the converged filter solution for the RJM. We can see that the introduction of a higher fidelity model allows for a significant improvement of the filter performances, with an order of magnitude reduction for the RMS of the range postfit residuals and $\chi_v^2$ three order of magnitude lower. However, the model is still not able to produce an acceptable fit, indicating that shorter time-scale variations to the NGA values around perihelion might be required to produce a good fit of the observed measurements.

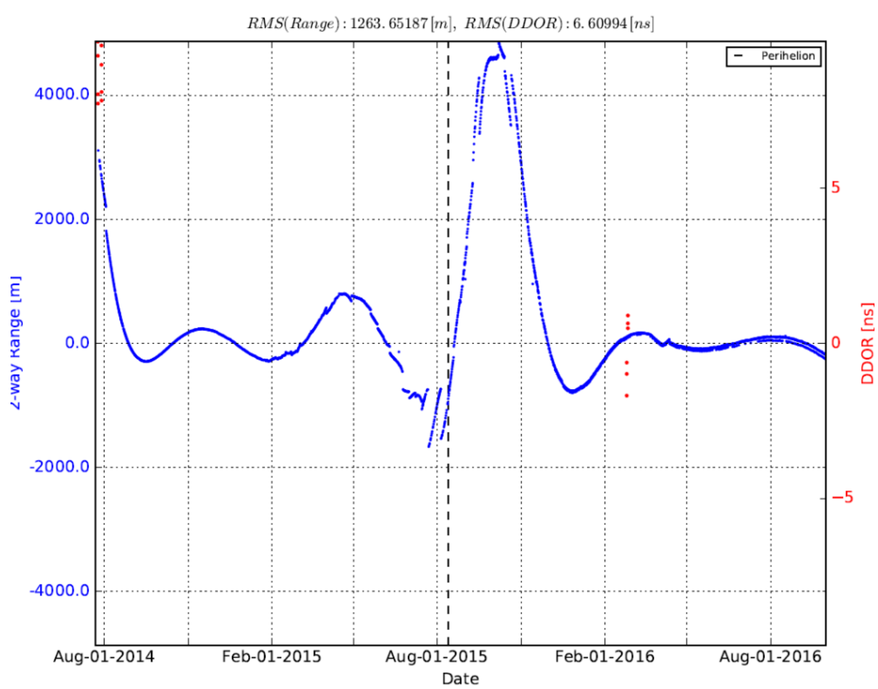


Figure 3-24 Post-fit residuals and statistics for the for the RJM.

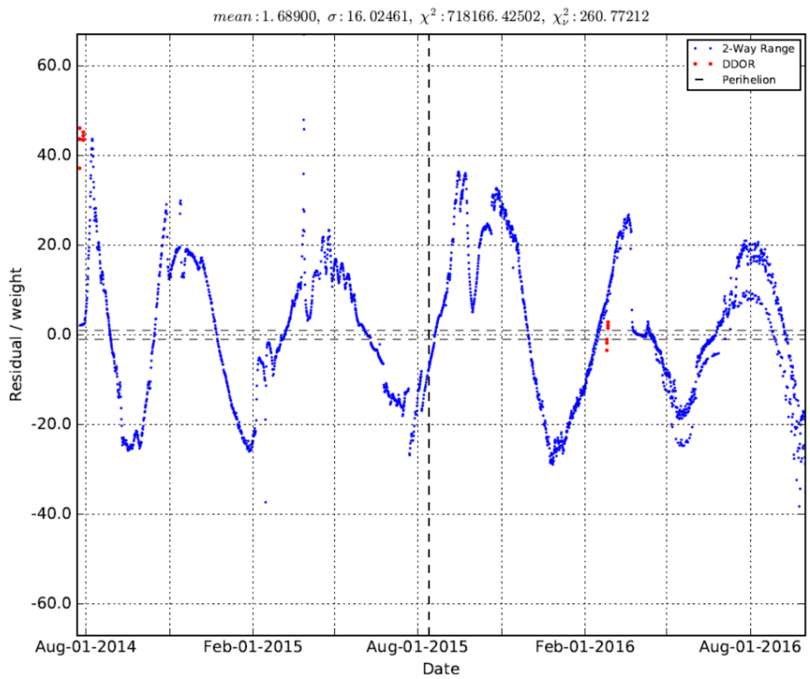

Figure 3-25 Weighted post-fit residuals and chi-square statistics for the for the RJM.

### 3.7.3 Stochastic NGA models

#### *3.7.3.1 Definition of stochastic intervals*

A key step towards the construction of a stochastic model is represented by the definition of suitable stochastic intervals during which the model's parameters remain constant. A straightforward approach could imply the use of fixed intervals for the whole duration of Rosetta's proximity phase. However, preliminary results using the ESM and the RJM suggest that both water vaporization curves and instantaneous NGA values follow an $r^{-5}$ power law and are highly dependent on the comet's heliocentric distance. Using the same time window at 3AU or around perihelion at 1.2 AU would result in sub-optimal performances.

The proposed definition is therefore based on a direct link between the stochastic interval length and the instantaneous heliocentric distance, according to the following procedure:

1. An initial epoch is selected, which corresponds to $t_0 = t_P - \Delta T$, where $t_P$ is the time of perihelion crossing, and $\Delta T \cong 20\ days$ is the estimated time offset between the perihelion and the peak of comet activity using the RJM.
2. A second epoch is stored, which correspond to $t_1 = t_0 + \Delta T_0$, where $\Delta T_0$ is the minimum stochastic interval length and represents a free parameter of the model.
3. A new stochastic interval is computed according to $\Delta T_1 = \min\left(60\ d, \Delta T_0 \cdot \left(\frac{R_1}{R_P}\right)^5\right)$, where $R_P$ is the comet heliocentric distance at perihelion and $R_1$ is the comet heliocentric distance at time $t_1 - \Delta T$. This way, the stochastic interval increases from the initial value of $\Delta T_0$ up to a maximum value of 60 days as the comet moves further away from the Sun.
4. Steps 2 and 3 are then repeated until the EoM is reached. A similar procedure is performed backwards in time from the perihelion to the arrival of Rosetta at 67P/CG. The collection of epochs defined with this procedure are then used as extremes for the array of stochastic intervals.

### 3.7.3.2 Constant Stochastic Model

The first stochastic model to be evaluated is the CSM, for which the acceleration components in the RTN frame are defined as constant values for each stochastic interval.

To make a consistent comparison between this model and the global ones, acceleration a-priori uncertainties were referenced to a common distance $R_{ref} = 1AU$, in line with the formulation of the ESM. By observing that NGAs follow, on average, an $r^{-5}$ power law, a-priori uncertainties for the $k^{th}$ stochastic interval are scaled according to (3.19), where $\sigma_{a_i}|_{ref}$ is the reference uncertainty at 1AU, and $R_k$ is the heliocentric distance at midpoint of the stochastic interval.

$$\sigma_{a_i}|_k = \sigma_{a_i}|_{ref} \cdot \left(\frac{R_{ref}}{R_k}\right)^5 \ for\ k \in [1, N] \tag{3.19}$$

While performing preliminary OD runs, it was observed that some of the estimated acceleration components were showing oscillatory behaviors which were not consistent with physical variations over the characteristic time-scale of the stochastic intervals. This trend was particularly pronounced for the test cases employing short stochastic time intervals (in the order of few days), suggesting that the estimated parameters might be trying to “absorb” other non-physical effects such as discontinuities of the s/c relative trajectory or uncalibrated range delays.

To avoid the risk of over-fitting and produce realistic estimations of the acceleration components, a series of loose constraints were added between the successive stochastic accelerations. The expression for these constraints is given in (3.20), where $C$ represents a variable constraint factor, and $\sigma_{a_i}|_{k+1/2}$ is the acceleration a-priori uncertainty at the boundary between the stochastic intervals, which is determined according to (3.19). A value of $C = 1$ means that the acceleration can change between two adjacent stochastic intervals by an amount equal to the same a-priori sigma used in the estimation: in practice the acceleration is relatively free to change. On the opposite, $C \gg 1$ means that the acceleration can change slowly between successive intervals, making the estimated values less susceptible to short scale variations in the measurement residuals (e.g. from trajectory discontinuities).

$$a_i|_{k+1} - a_i|_k < \frac{1}{C} \cdot \sigma_{a_i}|_{k+1/2}\ \ for\ \ k \in [1, N] \tag{3.20}$$

Each of the test cases presented hereafter includes a sensitivity analysis with respect to the values of the constraint factor $C$, in an effort to produce an estimation of the NGA components that closely matches the physical processes involved, while avoiding to over-constrain the results.

Figure 3-26 shows the $\chi_\nu^2$ values of the post-fit residuals as a function of the stochastic interval length at the pericenter $\Delta T_0$, ranging between 5 and 29 days, and of the constraint factor $C$, which is varied between 1 (i.e. no constraint) and 30. It can be seen that there is a short range of stochastic interval lengths between 9 and 13 days for which the $\chi_\nu^2$ are close to 1. For stochastic intervals shorter than 7 days, the models systematically over-fit the data. Conversely, intervals over 15 days are not able to produce a proper fit. This strong dependency of the solution from the selection of arbitrary parameters such as $\Delta T_0$ and $C$, indicates that the proposed model is not perfectly suited for the NGA representation, and that a higher level of complexity is needed.

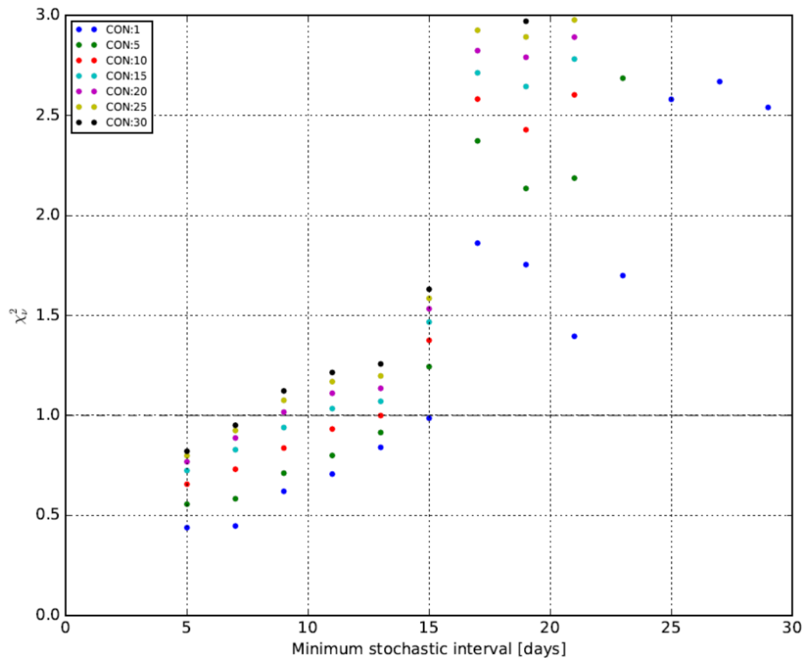


Figure 3-26 Reduced chi-square values for the CSM.

#### *3.7.3.3 Linear Stochastic Model*

The second stochastic model to be explored is the LSM, for which the acceleration components in the RTN frame are defined as linear piecewise continuous accelerations for each stochastic interval, as in (3.8).

Similarly to the CSM, a-priori uncertainties for the degree-zero coefficient at the $k^{th}$ stochastic interval are defined according to (3.19).

Having no a-priori information on the actual values for the derivative of the acceleration components (jerks), the a-priori uncertainty for the degree-one coefficient $j_i|_k$ is obtained dividing the local acceleration uncertainty by the length of the stochastic interval.

$$\sigma_{j_i}|_k = \frac{\sigma_{a_i}|_k}{\Delta T_k} \; for \; k \in [1, N] \tag{3.21}$$

To avoid over-fitting, loose constraints between successive stochastic intervals are applied here as well, except this time the constraint is applied to the derivative of the acceleration between adjacent intervals, according to (3.22). Continuity of the degree-zero parameter is already ensured by the much tighter constraint given in (3.9). Finally, the estimated value of the jerks at the first and last stochastic intervals are constrained to be null, to ensure zero acceleration values at high heliocentric distances ($R > 3.5\ AU$).

$$j_i|_{k+1} - j_i|_k < \frac{1}{C} \cdot \sigma_{j_i}|_{k+1/2} \;\; for \;\; k \in [1, N] \tag{3.22}$$

Figure 3-27 shows the $\chi_\nu^2$ values of the post-fit residuals as a function of the stochastic interval length at the pericenter $\Delta T_0$, ranging between 5 and 27 days, and of the constraint factor $C$, which is varied between 1 (i.e. no constraint) and 30.

It should be pointed out that the $\chi_\nu^2$ values for the LSM were computed by subtracting the number of tight constraints, given in equation (3.9), from the number of estimated parameters, bringing the effective number of parameters from $6N$ to $3N + 1$.

The most notable difference from the CSM is represented by a reduction of the $\chi_\nu^2$ values and of the constraint factor dependency at longer stochastic intervals, with values that remain close to 1 for intervals up to 4 weeks long. This suggests that the LSM might be adequate to model NGA for the problem at hand, having several combinations of $\Delta T_0$ and $C$ values that result in acceptable fits. These solutions have been further analyzed in the next sections, leading to the selection of a reference trajectory solution.

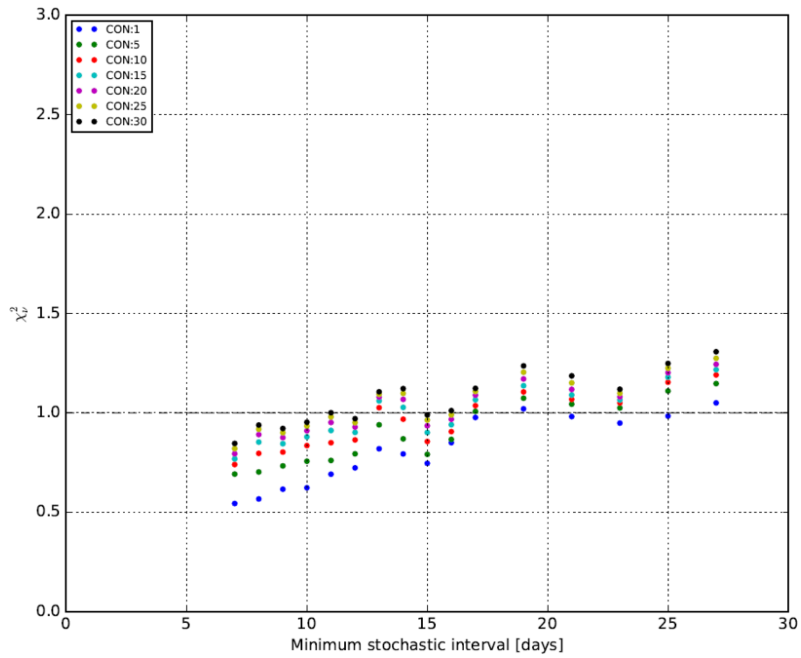


Figure 3-27 Reduced chi-square values for the LSM

### *3.7.3.4 Influence of the constraint factor on the NGA estimation*

To evaluate the influence of the constraint factor on the OD solution, we consider as example the LSM with a minimum time interval $\Delta T_0 = 14\ days$ and compare the estimated NGAs for increasing values of $C$. Figure 3-28 shows respectively the RTN acceleration components and modulus obtained with constraint factors of 1 (no constraint) and 10.

Earth-based astrometric measurements collected during the first six apparitions of comet 67P-CG (up to 2004) indicate the radial acceleration to be the highest NGA component, with non-negligible (but smaller) values for the transverse and normal components [40]. Similar findings are also confirmed in literatures by a wide array of cometary observations (e.g. in [38], [41], [50] ). This seems to be in contrast with the estimated values of the transverse acceleration for the unconstrained case (Figure 3-28), which has the same order of magnitude of the radial component. Moreover, we can observe abrupt changes in the magnitude and sign of all three acceleration components around perihelion, which are reflected in the modulus as well. While this behavior cannot be ruled out a-priori for the normal and tangential components, there is no evident physical mechanism that could explain negative values for the radial acceleration component, suggesting that the unconstrained solution is non-physical.

As stated in 3.7.3.2, the constraint factor was initially introduced with the aim of mitigating the amount of over-fitting at short stochastic intervals, which was producing non-physical NGA solutions. This effect is observed in Figure 3-28, where we see that the introduction of a constraint factor $C = 10$ induces a reduction of both formal uncertainties, which is particularly evident for the normal component, and acceleration magnitudes, with the effect of smoothing out most of the short scale variations for the radial component.

Although the introduction of this factor and its implementation are somewhat arbitrary, it is shown in the next sections that all the candidate solutions obtained with various combinations of $\Delta T_0$ and $C$ values are statistically consistent with each other and with the original solution from ESOC FD.

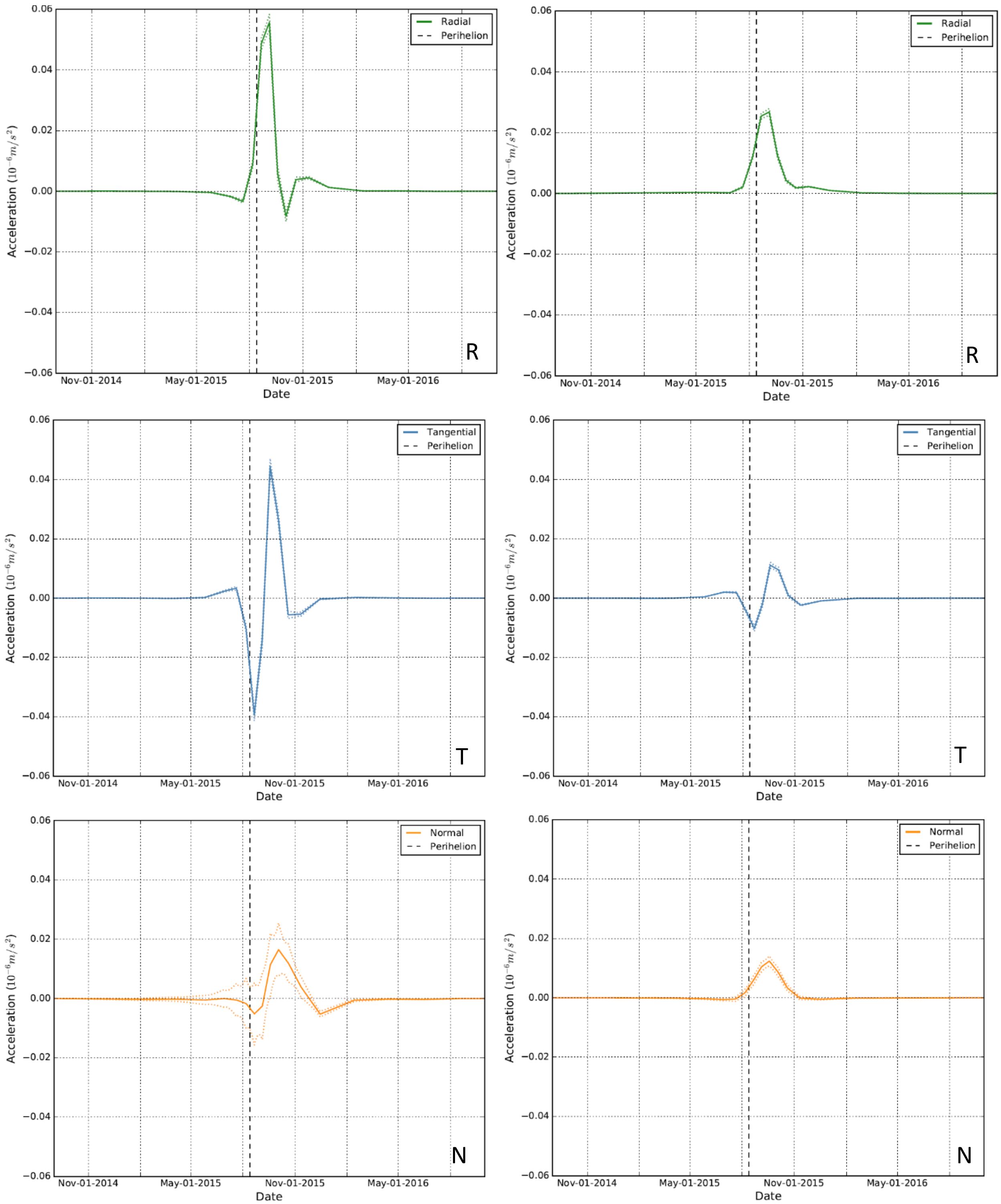

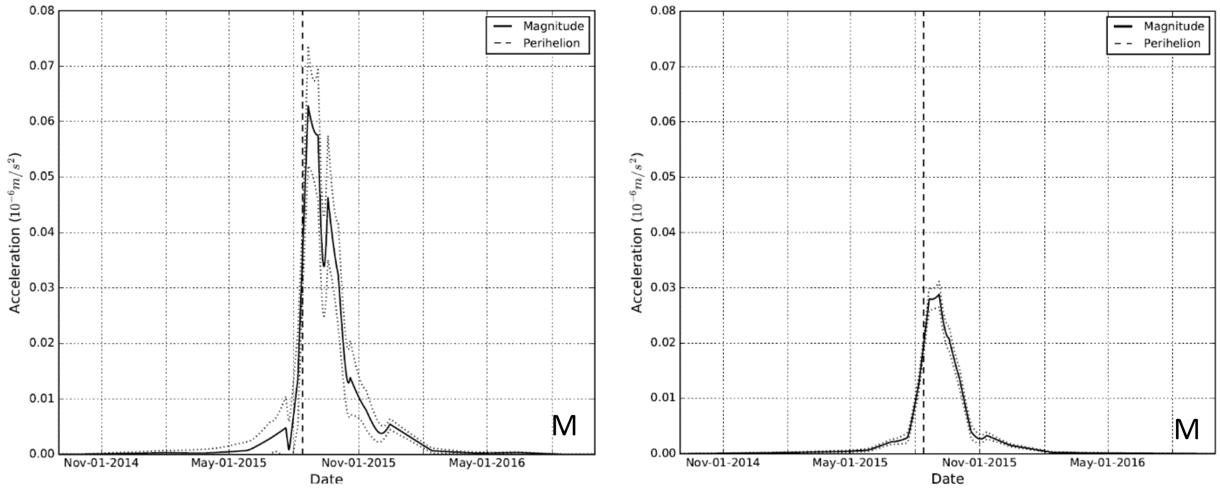


Figure 3-28 Estimated values for the radial and normal NGA components using C=1 (no constraint).

### 3.7.4 Comparison of the down-selected cases

Based on the analysis in 3.7.3, a preliminary selection of the suitable test-cases is performed by keeping only the LSM filter solutions for which the reduced chi-square statistics are close to 1. Moreover, only the test cases for which $C > 1$ were retained, as a preventive measure against non-physical NGA estimation.

Table 3-10 gives a summary of the filter performances for each of the down-selected test cases by providing the statistics of their postfit residuals. It can be seen, that all solutions have comparable results in terms of RMS of the residuals and reduced chi-square statistics. Therefore, the final selection of the filter setup to be used for the trajectory reconstruction of 67P/CG mostly relied qualitative observations.

Table 3-10 Statistics of the postfit residuals for the selected test cases

| ID | $\Delta T_0[d]$ | $C$ | $RMS_{range}$ $[m]$ | $RMS_{\Delta DOR}$ $[ns]$ | $\chi^2$ | $\chi^2_v$ |
|---|---|---|---|---|---|---|
| 1 | 11 | 25 | 89.23 | 0.53 | 2630 | 0.98 |
| 2 | 11 | 30 | 89.49 | 0.58 | 2686 | 1.00 |
| 3 | 13 | 10 | 92.94 | 0.35 | 2760 | 1.03 |
| 4 | 13 | 15 | 93.74 | 0.42 | 2852 | 1.06 |
| 5 | 13 | 20 | 93.89 | 0.49 | 2904 | 1.08 |
| 6 | 14 | 15 | 92.09 | 0.67 | 2767 | 1.03 |
| 7 | 14 | 20 | 92.44 | 0.78 | 2876 | 1.07 |
| 8 | 16 | 20 | 88.06 | 0.51 | 2608 | 0.97 |
| 9 | 16 | 25 | 88.85 | 0.57 | 2669 | 0.99 |
| 10 | 17 | 5 | 89.74 | 0.26 | 2716 | 1.01 |
| 11 | 17 | 10 | 89.80 | 0.34 | 2794 | 1.04 |

A first assessment of the consistency between the proposed solutions was performed by comparing the estimated comet ephemerides with the original trajectory from ESOC FD.

Figure 3-29 shows the position differences between the various test cases and the reference solution (corresponding to the zero axis) in the RTN frame. This particular solution, which corresponds to ID 5 in

Table 3-10, was selected as the one best approximating the geometrical center of the bundle of trajectories.

Overall, we can observe a good agreement between the proposed solutions and the ESOC reference, with residuals between the most extreme trajectories in the order of 10-20 km for the radial and transverse components and of roughly 100 km for the normal component.

Another key step in the validation of the proposed solution is represented by the comparison between their estimated position uncertainties. Figure 3-30 shows the formal uncertainties (1-sigma) of the estimated trajectory for the down-selected test cases in the RTN frame. Overall, we observe similar trends between the different solutions, with maximum position uncertainties occurring around perihelion and roughly a factor of two difference between maximum and minimum uncertainties for the various solutions. However, peak values for the uncertainty at perihelion, which are in the order of roughly 3 km for the radial and transverse components, and 20 km for the normal components, are systematically lower than the corresponding magnitudes of the position differences in Figure 3-29, suggesting that the formal covariances might be overly optimistic. As a safety measure, the position uncertainty of the reference trajectory reconstruction is taken as 5 times the estimated formal uncertainty, so that all trajectory solutions within the bundle are  contained within ±5σ if the reference solution.

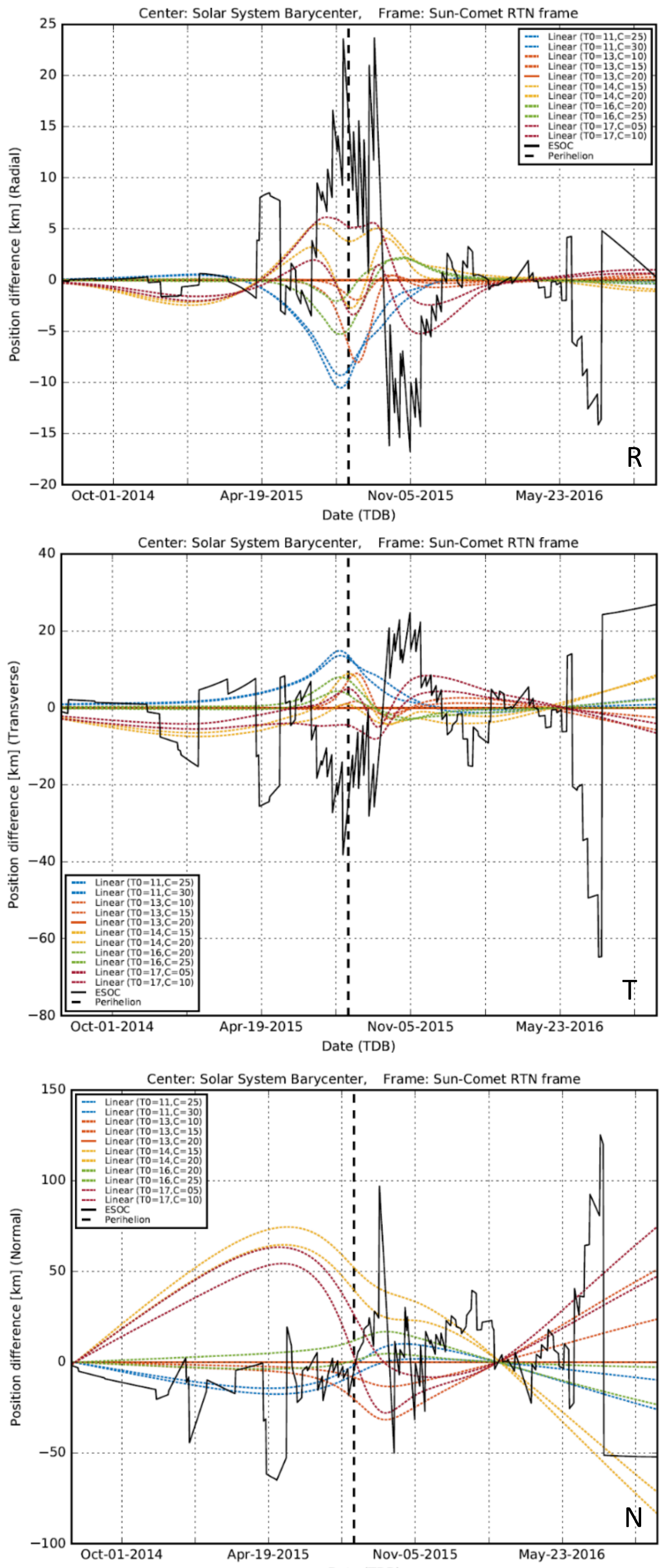


Figure 3-29 Position differences between the selected trajectories in the RTN frame.

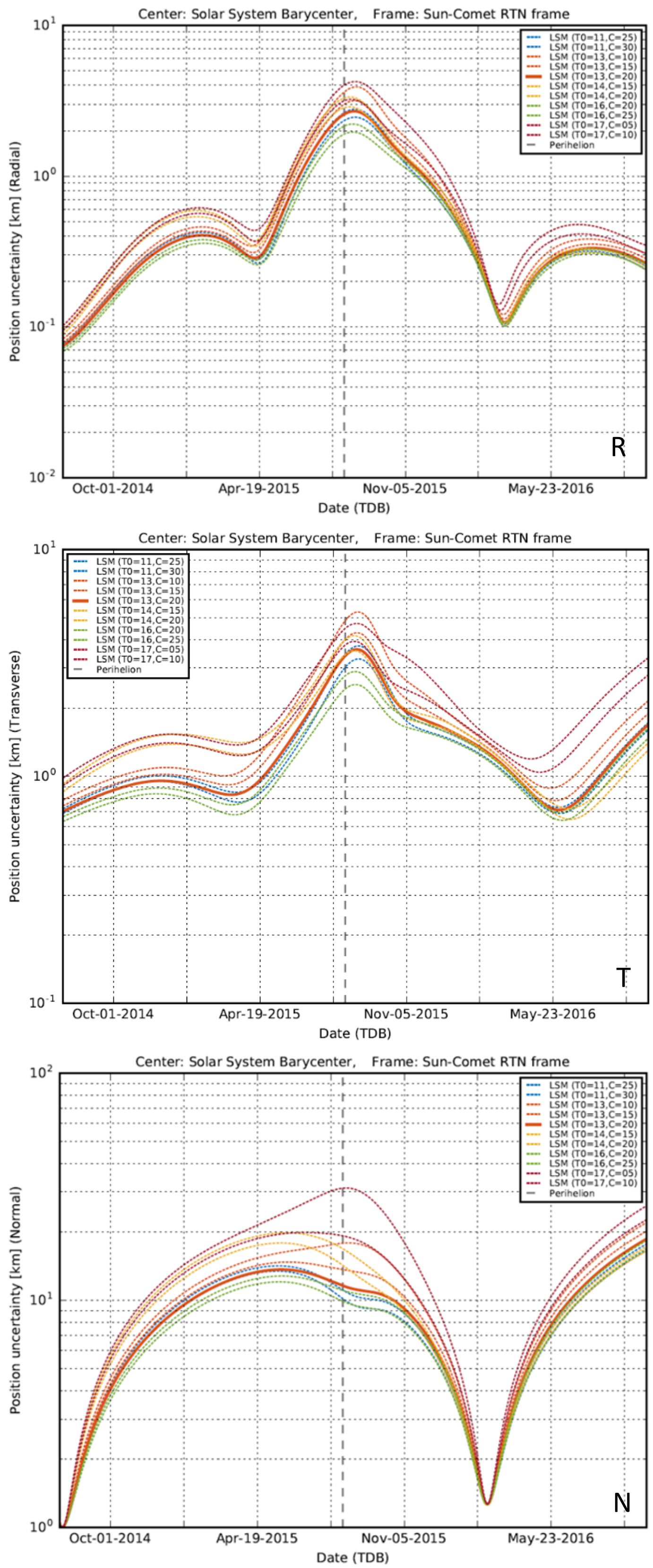


Figure 3-30 Formal uncertainties of the estimated position (1σ) in the RTN frame for the selected test cases.

Finally, Figure 3-31 shows the estimated values of the NGAs in the RTN frame for the selected test-cases. Overall, we observe a good agreement between the different solutions, with estimation differences that are higher as we get closer to perihelion due to the increased uncertainty in the mapped ranged measurements. Moreover, we see that the biggest differences are observed in the transverse and normal components, which are generally less observable than the radial one.

Similarly to what observed for the position, the estimated formal uncertainties for the NGA components (not reported here for brevity) are deemed as overly optimistic if compared to the variations observed in the solution bundle. For this reason, the final uncertainty for the reference solution will correspond to 5 times the estimated formal uncertainty. With this safety factor, all estimated NGA values within the bundle are contained within ±5σ if the reference solution (represented by the thick orange line in figure).

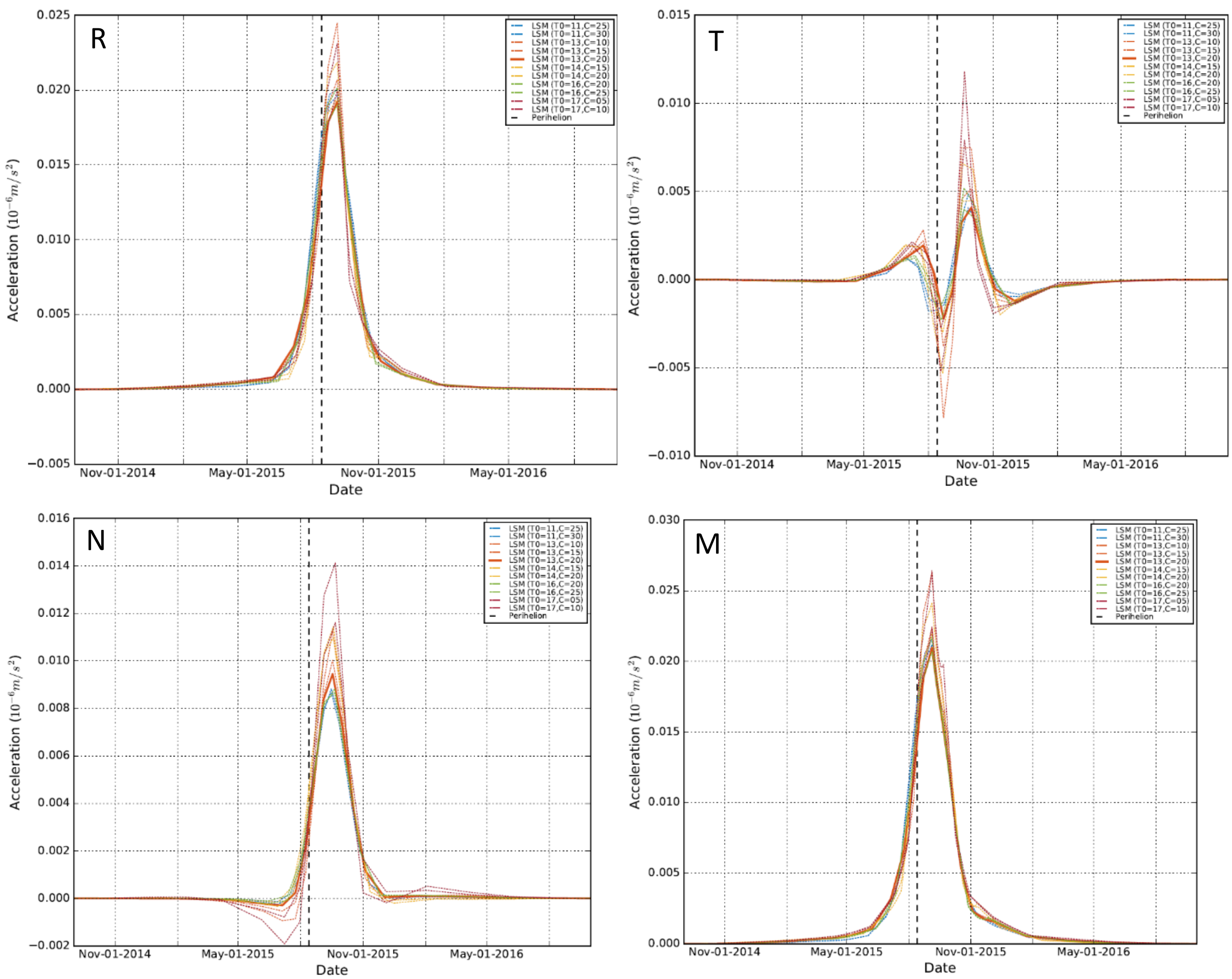


Figure 3-31 Estimated NGA components (RTN frame) and acceleration magnitude for the selected test cases.

### 3.7.5 LMS reference solution ($\Delta T_0 = 13$ days, C = 20)

#### *3.7.5.1 Post-fit residuals*

Figure 3-32, show the post-fit residuals and statistics for the LSM reference solution. It can be seen that the residuals remain more or less constant before February 2015 and after March 2016 (with the exception of the tail excursion and the initial FAT phase), where the NGAs are small and have a limited influence on the accuracy of the relative orbit reconstruction from ESOC FD. Between these values, the residuals start to degrade, with piecewise continuous blocks that are separated by small jumps in correspondence of the relative orbit discontinuities shown in Figure 3-4, and magnitudes that reach a maximum after the perihelion (indicated by the vertical dashed line), where the peak of NGA is expected.

Figure 3-33 shows the weighted post-fit residuals for the same test-case, where the data weights are computed according to (3.14) and using a value of $k = 0.5$ for the exponential scale factor. It can be seen that the weighted residuals remain confined within the ± 1 threshold for most of the displayed time interval, indicating an overall agreement between the post-fit residuals and the selected weighting scheme. However, a significant departure is observed close to the perihelion. Having no a-priori information on the relative orbit uncertainty it is difficult to identify whether the source for this discrepancy actually lies within the weighting scheme or the dynamical model for the NGA representation.

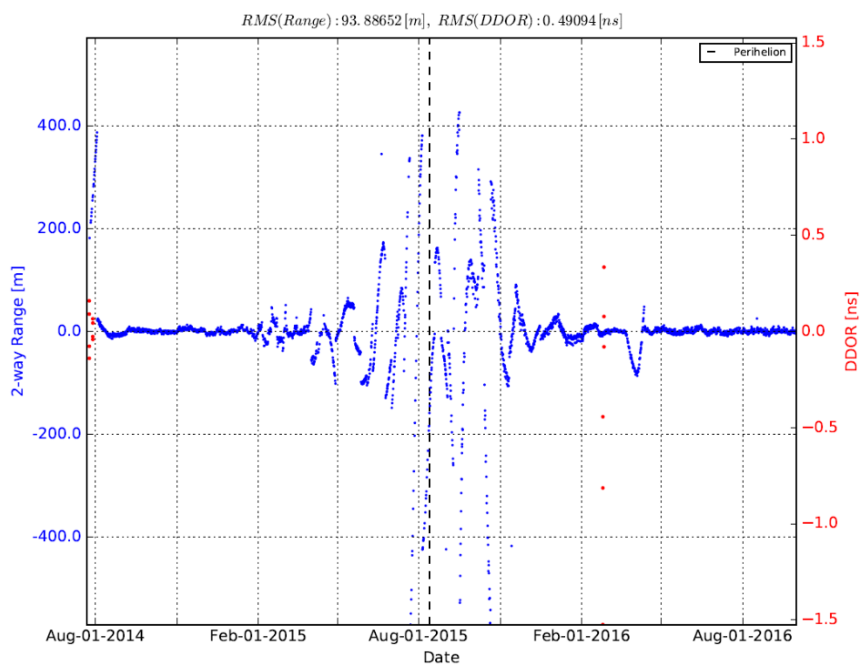


Figure 3-32 Post-fit residuals and statistics for the reference LSM solution ($\Delta T_0 = 13$ days, C = 20).

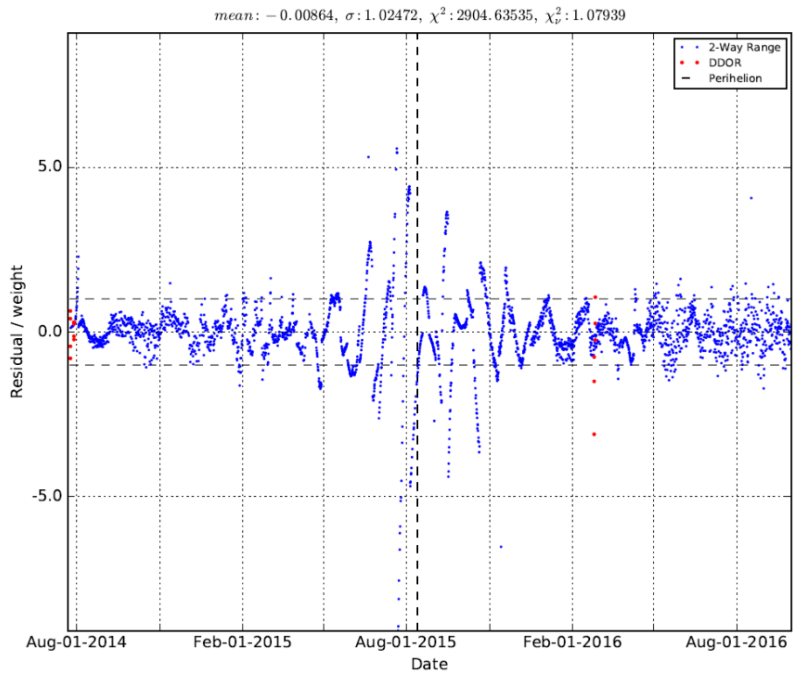


Figure 3-33 Weighted post-fit residuals and chi-square statistics for the LSM reference solution ($\Delta T_0$ = 13 days, C = 20). Horizontal dashed lines represent weighted residuals of ±1.

#### *3.7.5.2 Estimated NGA values*

Figure 3-34 shows the estimated values and uncertainties for the stochastic NGA components in the RTN frame. It can be seen that the acceleration is dominated by the radial component, with a peak value of $a_R = (1.922 \pm 0.369) \cdot 10^{-8}\ m/s^2$, which is nearly double that of the normal component $a_N = (0.945 \pm 0.094) \cdot 10^{-8}\ m/s^2$.

Both of these components remain positive for the whole duration of the comet's active period and have their maxima occurring after perihelion, with an offset that is more or less consistent with the value of $\Delta T$ estimated with the ESM or RJM. However, peak values for the normal acceleration occur slightly after the ones for the radial component.

The transverse component is generally smaller in magnitude with respect to the other two, reaching peak absolute values of $a_T = (0.408 \pm 0.058) \cdot 10^{-8}\ m/s^2$. Unexpectedly, this component changes sign during the comet's active period, with an abrupt variation occurring around the same time of the peak acceleration for the other two components.

It should be stressed out that the acceleration uncertainties shown in Figure 3-34 already include a safety margin of 5 with respect to the estimated formal uncertainties of the respective accelerations. This ensures that the estimated values, which were obtained with a data-driven approach with limited assumptions on the physical mechanism behind the surface outgassing, should represent a good approximation of the actual NGAs.

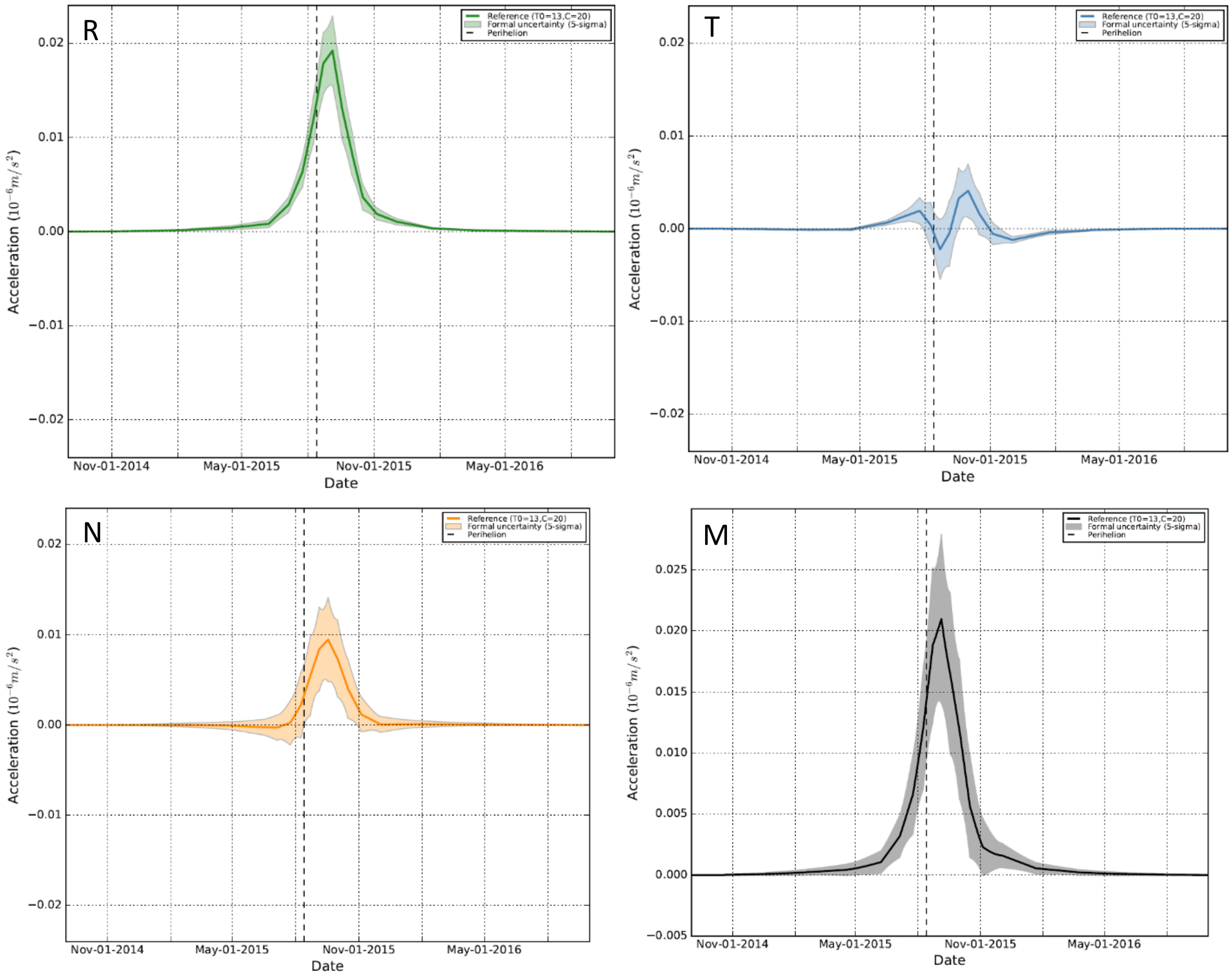


Figure 3-34 Estimated NGA components and module in the heliocentric RTN frame. Shaded areas represent the 5σ formal uncertainties from the complete covariance matrix.

#### *3.7.5.3 Ephemeris reconstruction uncertainty*

For a complete characterization of the reference orbit reconstruction, it is interesting to compare this solution with the original ESOC trajectory in a reference frame which is more consistent with the information content provided by the range and ΔDOR observable.

Specifically, Figure 3-35 shows the position differences in the Earth-Comet LOS frame, where the first axis is the Earth-Comet LOS direction, the third axis is the comet orbit-normal direction, and the second axis completes the right-handed orthogonal frame.

Most of the information content for the 2-way range is provided in the LOS direction, as shown by the position differences and uncertainties in Figure 3-35 (plot **L**), which are much smaller with respect to the other components, with maximum differences in the order of a few hundred meters. It is also interesting to note that discontinuities in the ESOC trajectory appear more or less as zero-mean white noise around the estimated trajectory, with oscillations that are generally higher than the LOS position uncertainty, suggesting that the current orbit reconstruction provides a significant reduction in the orbit uncertainty along this direction. An exception to this white noise appearance is represented by a few offsets during Rosetta's FAT phase (July 2014) and far tail excursion (March 2016), during which the relative orbit trajectory was poorly known. Another offset is observed in correspondence of the February 2015 solar conjunction. This is expected since the original ESOC estimation did not include the effect of solar plasma, which is estimated to produce a range bias in the order of roughly 120 m (see section 3.5.4), which is compatible (albeit smaller) with the observed offset.

The information content for the ΔDOR observables is provided along a direction that is perpendicular to the s/c LOS and to the baseline between the receiving stations. Each measurement will therefore provide different information depending on the instantaneous geometry of the station baseline with respect to the comet, which is difficult to predict. However, we know that ΔDOR provides most of the information content for the normal component of the comet's orbital motion, which is poorly observable using range due to the low declination values occurring during the Rosetta proximity phase. This is clearly shown in Figure 3-35 (plot **N**), where we observe a direct correlation between the ΔDOR measurements in July 2014 and February 2016 and a reduction of the normal position uncertainty. However, we can observe from the same plot that the discontinuities in the original ESOC trajectory have an order of magnitude that is comparable with the uncertainty of the estimated solution, suggesting that the current reconstruction provides a limited improvement (if any) to the position uncertainty along this direction.

Position difference and uncertainty along the cross axis direction (plot **C**) somewhat represent an intermediate case with respect to the previous two, having a small but consistent reduction in the position uncertainty.

In a similar fashion, Figure 3-36 provides position differences and uncertainties in the RTN frame.

Overall, we can observe a good agreement between the estimated trajectory and the original solution, which oscillates around the former with almost zero mean, except for limited time periods during the far tail excursion and around perihelion. Position offsets for the radial and transverse components around perihelion seem to indicate that some of the underlying NGA dynamics are not perfectly captured by the proposed stochastic model. However, it should be kept in mind that the current analysis was motivated by the objective of producing a continuous and more accurate reconstruction for the orbit of 67P/CG, so strict adherence to the original ESOC solution is not necessarily a guarantee of highest quality.

Finally, Figure 3-37 and Figure 3-38 summarize the estimated position uncertainties for the LOS and RTN frames, respectively, using a logarithmic scale.

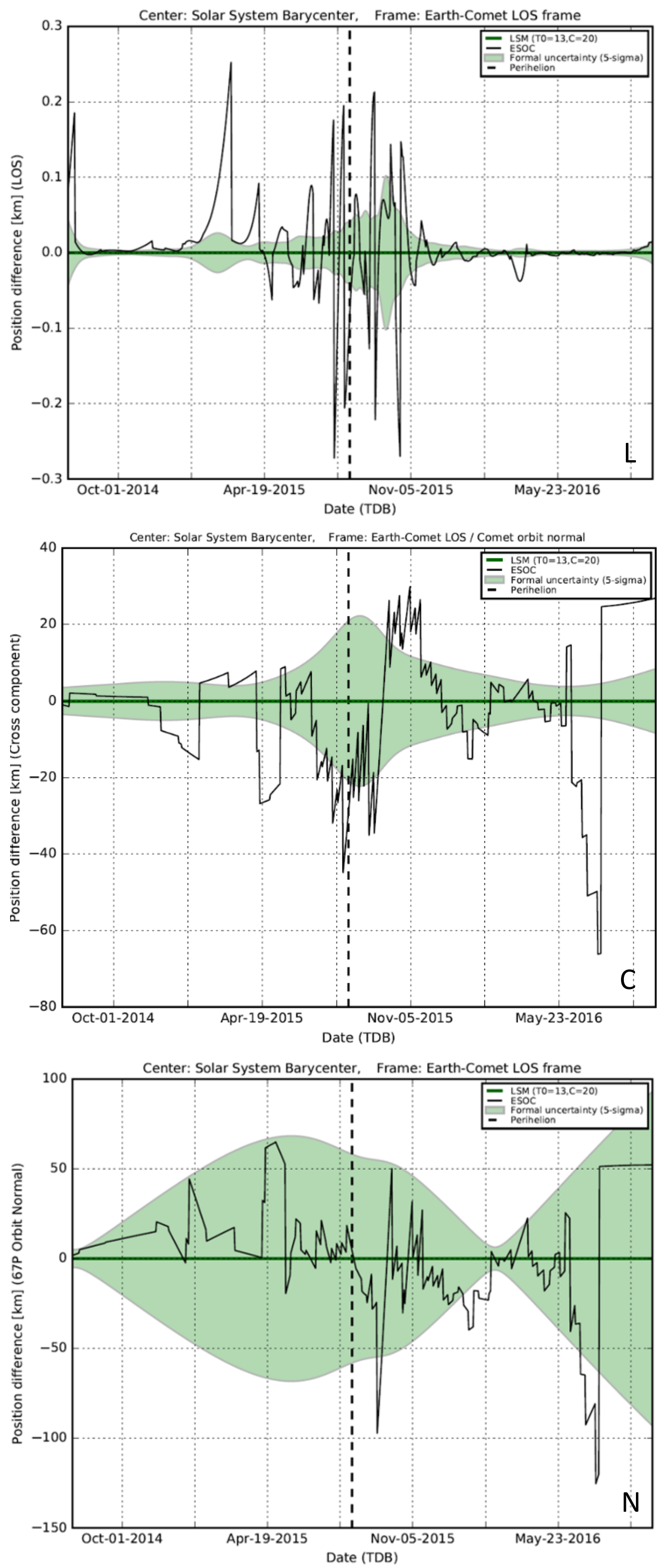


Figure 3-35 Position differences and uncertainties between the reference solution and the ESOC trajectory (LOS frame).

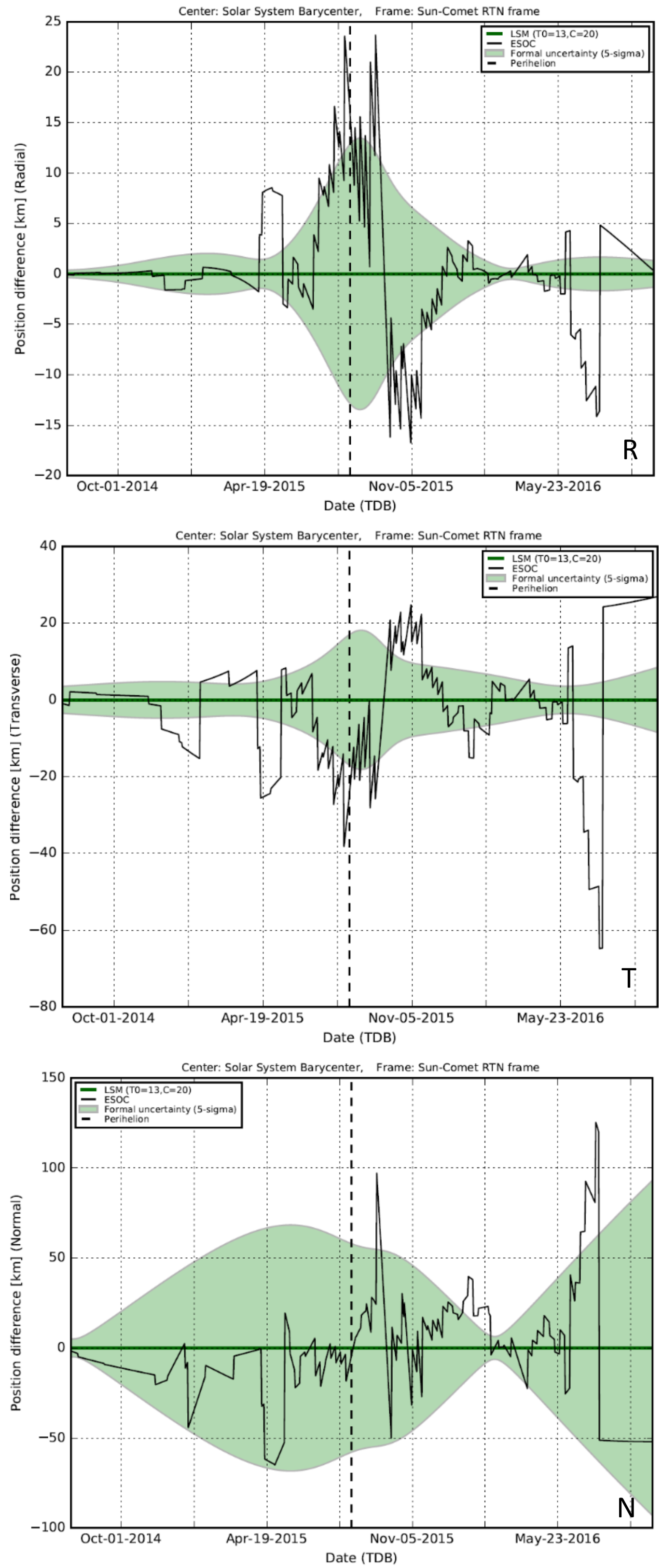


Figure 3-36 Position differences and uncertainties between the reference solution and the ESOC trajectory (RTN frame).

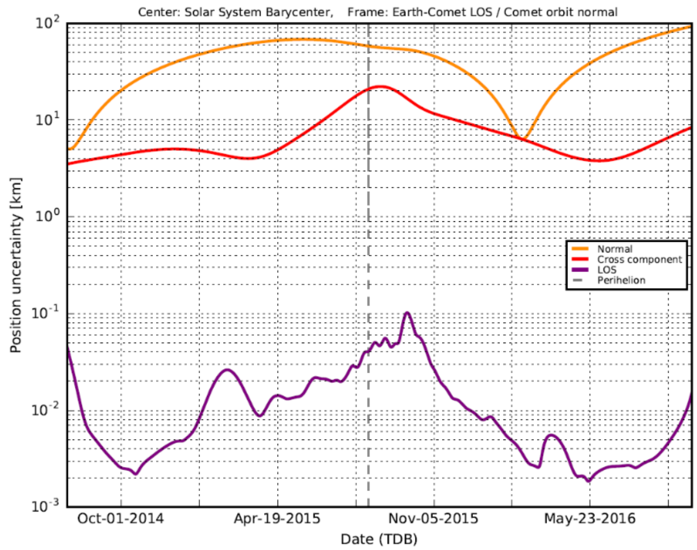


Figure 3-37 Estimated position uncertainty in the LOS frame.

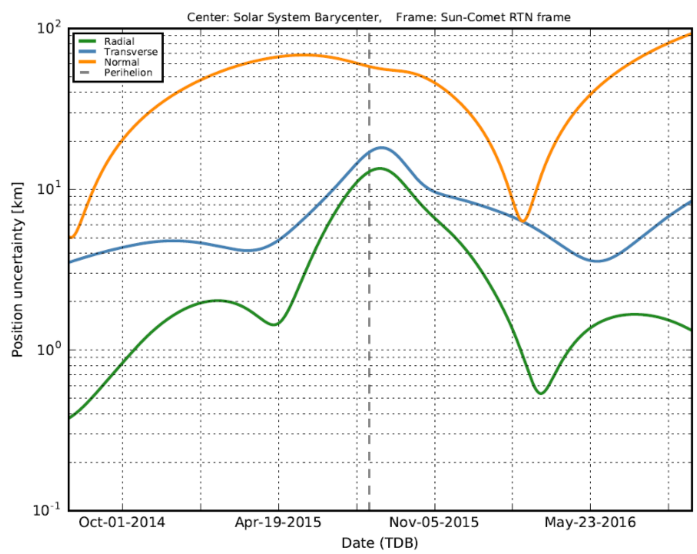


Figure 3-38 Estimated position uncertainty in the RTN frame.

## 3.8 Interpretation

The main outcome of the results presented in 3.7 are the following:

- Simple global models like the SM and ESM are not adequate to fit Rosetta's radiometric measurements to values consistent with the errors in the relative orbit trajectory. Two-way range residuals show RMS values in the order of 20-30 km, which are much larger than the assumed errors due to the relative trajectory, which are in the order of 1 km at maximum (see Section 3.5.7).
- Using a higher fidelity global model like the RJM significantly improves the accuracy of the fit, with RMS values for the range residuals in the order of 1.2 km. However, this model is still not able to produce an adequate fit and relies on several assumptions on the physical parameters involved in the outgassing process
- The introduction of simple stochastic models (i.e. based on time varying parameters) allows to reduce the magnitude of the radiometric residuals by more than one order of magnitude, with RSM values of roughly $100\,m$ for the 2-way range and $0.5\,ns$ for the ΔDOR. Maximum range residuals around

perihelion have values in the order of $400\ m$, which are consistent with the observed discontinuities in the relative orbit trajectory.

- The improvement of the post-fit residuals comes at the cost of an increased complexity and of a high dependency of the estimated comet ephemeris on the parameters used for the stochastic model definition. Depending on the values for the minimum stochastic interval length $\Delta T_0$, and of the constraint factor $C$, the estimation process may lead to either realistic or completely non-physical solutions for the comet ephemeris and NGA components. This effect is most likely caused by the discontinuities in Rosetta's relative orbit reconstruction, which the filter tries to compensate-for by adjusting the stochastic NGA parameters.
- The selection process proposed in 3.7.1 and 3.7.4, which is based on the evaluation of the reduced chi-squared statistics and on the minimization of the position residuals with respect to the original ESOC solution, leads to an estimation of the comet NGAs that is consistent for all the proposed test cases, providing an indication of the robustness of the  solution.
- The reconstructed trajectory, which employs the LSM with a minimum stochastic interval $\Delta T_0 = 13\ days$ and a constraint factor $C = 20$, produces a continuous ephemeris reconstruction for 67P/CG with maximum uncertainties around perihelion of roughly $10\ km, 20\ km, 70\ km$ in the RTN reference frame. These uncertainties are consistent with the position differences between the final trajectory and the ones obtained for the alternative test cases, suggesting that values of the estimated uncertainties may provide a good indication of the real reconstruction error.
- As expected, the highest reduction in position uncertainty with respect to the ESOC solution is obtained along the Earth-comet LOS direction, where most of the information content for the 2-way range measurements resides. Limited uncertainty reductions are observed along the POS directions, which rely heavily on the ΔDOR measurements to complement the limited information content of ranging data.

# 4 Conclusions and future work

## 4.1 TDCS testbed

The work presented in this thesis had as subject the performance characterization of a new prototype of Tropospheric Delay Calibration System installed at the DS3 ESTRACK complex in Malargue.

An extensive testbed campaign was carried out between February and September 2019, using the TDCS alongside the main DS3 antenna to track the GAIA spacecraft during a series of schedules passes. The described analysis, which does not replicate the full OD solution used for the navigation of GAIA, was mostly intended as a side by side comparison of the filter performances when TDCS-based tropospheric calibrations are used in place of standard GNSS-based calibrations.

The instrument performances were characterized in terms of RMS values of the Doppler postfit residuals and ASD values computed at characteristic stability intervals. The OD results indicate that an average improvement of approximately 46% is observed in the RMS of the Doppler residuals when TDCS-based calibrations are used. The actual magnitude of this improvement strongly depends on the atmospheric conditions occurring during the tracking pass, with maximum reductions around 60% and a few passes with no appreciable RMS reduction. This high variability is mainly a result of the different air volumes sampled by TDCS with respect to the propagation path of the DSA tracking link and by the sensitivity of the neural-network retrieval algorithms to variations of the observed atmospheric scene. Another possible cause is represented by the low water vapor content and still air conditions that are observed for particular passes (all GAIA passes occur at night), which cause the tropospheric excess path length to become negligible with respect to other errors sources.

Although these results are promising, a complete statistical characterization of the TDCS performances would require the analysis of a larger sample of tracking passes under various observing conditions. Of the 44 total passes that were recorded during the testbed campaign, only 32 were actually included within the orbit determination due to TDCS technical issues that resulted in data losses. Nonetheless, the experience gathered during the course of this testbed campaign was pivotal to develop operational and data handling procedures to improve the reliability of TDCS products.

Future work will include additional observations for the GAIA spacecraft, with the introduction of 2-way range data as part of the OD process. Moreover, a new testbed campaign is currently underway for the BepiColombo s/c, which uses a $K_A/K_A$ band tracking link. Most of the BC observations will be conducted during daytime and with the s/c near solar conjunction, allowing to characterize the TDCS performances under diverse observational environments.

## 4.2 Rosetta OD analysis

The reference heliocentric trajectory for comet 67P/Churyumov-Gerasimenko is represented by the reconstructed operational solution from ESOC FD, which is the product of several long-arc and short-arc OD solutions collected during the Rosetta mission operations. Several discontinuities are present within this trajectory, due to the lack of a dynamical model for the representation of the comet NGAs.

The work presented in this thesis represents an effort to produce an accurate and continuous ephemeris reconstruction for comet 67P/Churyumov-Gerasimenko using Range and ΔDOR radiometric observables collected during the proximity phase of Rosetta around the comet. Considering the relative orbit trajectory as a time-varying offset, these measurements were mapped to the nucleus center and used to estimate the comet state, along with additional physical and observational parameters, most notably the NGAs. Determining the uncertainty of the mapped radiometric measurements has proven to be a challenging task, since an accurate model of the uncertainty for the relative orbit of Rosetta around the comet was not available. An empirical approach was therefore proposed, which defines the relative state uncertainty only as a function of the s/c cometocentric distance using the limited information from literature as boundary conditions.

Several OD runs were performed by varying the dynamical model used to represent the NGAs acting on the comet due to surface outgassing and the values of some key parameters used in the model definitions. Preliminary results from these runs indicated that time-independent empirical models, like the ones developed by Mardsen and Yeomans, are not adequate to describe the observed measurements.

The introduction of the higher-fidelity rotating-jet model, allowed to significantly improve the quality of the fit by including information on the comet rotational state and using a-priori knowledge on the physical properties of the surface. However, this model is still not adequate to describe the observed short-term variability of the comet outgassing around the perihelion.

Therefore, simple stochastic models using polynomial accelerations to represent the comet NGA were proposed. The advantage of using these stochastic models is that they are agnostic and provide useful inputs for further investigation involving detailed physical models of the cometary activity.

The selected test-case for the final OD reconstruction uses piecewise linear stochastic accelerations with interval lengths that vary between 13 days at perihelion and 2 months at higher heliocentric distances. This model allows for a continuous orbit reconstruction, with maximum uncertainties of roughly 10 km, 20 km, and 70 km in the RTN reference frame.

The proposed OD approach is useful in constraining the magnitude of the true NGAs acting on the comet. However, to obtain higher accuracies in the state estimation, more complex dynamical models will be needed, which make use of the actual physical processes occurring at the comet's surface. These will be the subject of further investigations.

It should also be noted that the estimated uncertainty of the out-of-plane component of the comet state, is one order of magnitude higher than the ones for the tangential and radial components. This is mainly due to the limited information content provided by the range measurements, particularly at the low declination values encountered during the last months of the Rosetta mission.

Ground-based astrometric measurements may represent a useful addition to the OD estimation, by complementing the ΔDOR measurements. Further investigations may address whether these observables may be successfully retrieved and integrated within the filter estimation, particularly during the months close to perihelion, where the accuracy of the relative orbit reconstruction is reduced.

Future works may also include a complete orbit determination reconstruction for both 67P/CG and of the Rosetta s/c by processing Doppler and optical measurements. This would allow to bypass the dependance on the relative state uncertainty for the mapping of radiometric observables.

# 5 References


[1] C. L. Thornton and J. S. Border, Radiometric Tracking Techniques for Deep-Space Navigation, John Wiley & Sons, 2003.

[2] T. D. Moyer, Formulation for observed and computed values of Deep Space Networks data types for navigation, John Wiley & Sons, 2005.

[3] L. Iess, M. Di Benedetto, N. James, M. Mercolino, L. Simone and P. Tortora, "Astra: Interdisciplinary study on enhancement of the end-to-end accuracy for spacecraft tracking techniques," *Acta Astronautica,* vol. 94, no. 2, pp. 699-707, 2014.

[4] L. Iess, S. Asmar and P. Tortora, "MORE: An advanced tracking experiment for the exploration of Mercury with the mission BepiColombo," *Acta Astronautica,* vol. 65, no. 5-6, pp. 666-675, 2009.

[5] C. Naudet, C. Jacobs, S. Keihm, G. Lanyi, R. Linfield, G. Resch, L. Riley, H. Rosenberger and A. Tanner, "The Media Calibration System for Cassini Radio Science: Part I," *The Telecommunications and Mission Operations Progress Report,* pp. 42-123, 2000.

[6] P. Tortora, S. Crewell, G. Elgered, A. Graziani, P. Jarlemark, U. Loehnert, A. Martellucci, M. Mercolino, T. Rose and J. Schween, "AWARDS: Advanced microwave radiometers for deep space stations," in *Space Communications*, 2013.

[7] G. Maschwitz, H. Czekala, E. Orlandi and T. Rose, "Accuracy and Performance of Atmospheric Delay by a RPG Microwave Radiometer With Respect to Ground Calibration Systems for ESA Radioscience," in *TT&C workshop*, Darmstadt, 2019.

[8] R. Lasagni Manghi, G. Maschwitz, P. Tirtira, T. Rose, A. Martellucci, J. De Vicente, J. Villalvilla, M. Mercolino, A. Graziani, H. Czekala, E. Orlandi, D. Vanhoenacker-Janvier and L. Quibus, "Tropospheric Delay Calibration System (TDCS): design and performances of a new generation of microwave radiomters for ESA deep space ground stations," in *TT&C workshop*, Darmstadt, 2019.

[9] A. Graziani, P. Jarlemark, G. Elgered, A. Martellucci, M. Mercolino and P. Tortora, "Assessment of Ground-Based Microwave Radiometry for Calibration of Atmospheric Variability in Spacecraft Tracking," *IEEE Transactions on Antennas and Propagation,* vol. 62, no. 5, pp. 2634-2641, 2014.

[10] T. Prusti, J. De Brujine, A. Brown and e. al., "The Gaia mission," *Astronomy & Astrophysics,* vol. 595, no. A1, 2016.

[11] ESOC, "Tool for Auxiliary Scientific Calculations (TASC)," [Online]. Available: https://www.fd-tasc.info/roscmd/.

[12] W. M. Folkner, J. G. Williams, D. H. Boggs, R. S. Park and P. Kuchynka, "The planetary and lunar ephemerides DE430 and DE431," Interplanetary Network Progress Report 196(1), 2014.

[13] M. Ricart, "IFMS-OCC Interface Control Document 14.1.8," Makalumedia Internet & Engineering Services GMBH, 2011.

[14] J. W. Marini, "The effect of satellite spin on two-way doppler range-rate measurements," *IEEE Transactions on Aerospace and Electronic Systems,* Vols. AES-7, no. 2, pp. 316-320, 1971.

[15] N. Jakowski, M. Hoque and C. Mayer, "A new global TEC model for estimating transionospheric radio wave propagation errors," *Journal of Geodesy,* vol. 85, no. 12, p. 965'974, 2011.

[16] *TRK-2-23 Media Calibration Interface,* JPL, 2008.

[17] A. E. Niell, "Global mapping functions for the atmosphere delay at radio wavelengths," *Journal of geophysical research: solid earth,* vol. 101, no. B2, pp. 3227-3246, 1996.

[18] A. Martellucci, "TDCS reference document for definitions of parameters and test procedures (TEC-EEP/2016.184/AM v2.3)," 2019.

[19] ESOC, "Media calibrations for ESA spacecraft tracking data, DOPS-SYS-ICD-0510-OPS-GN v1.0," 2017.

[20] J. Saastamoinen, "Atmospheric Correction for the Troposphere and Stratosphere in Radio Ranging Satellites," in *The use of artificial satellites for geodesy*, American Geophysical Union (AGU), 1972, pp. 247-251.

[21] M. Ricart, *TTCP Software Interface Control Document (ICD) for RM datasets, Issue 2.1,* 2018.

[22] Radiometer Physiscs, A Rhode & Schwarz Company, "Instrument Operation and Software Guide, Operational Principles and Software Description for RPG Tropospheric Delay Calibration System - TDCS (G5 series)," 2018.

[23] F. Molteni, R. Buizza, T. Palmer and T. Petroliagis, "The ECMWF ensemble prediction system: Methodology and validation," *Quarterly journal of the royal meteorological society,* vol. 122, no. 529, pp. 73-119, 1996.

[24] T. Morley and F. Budnik, "Rosetta navigation at its first Earth swing-by," in *Proceedings of the International Symposium on Space Technology and Science*, 2006.

[25] F. Budnik and T. Morley, "Rosetta Navigation at its Mars Swing-by," in *Proceedings of the 20th International Symposium on Space Flight Dynamics*, 2008.

[26] T. Morley and F. Budnik, "Rosetta Navigation for the Fly-by of Asteroid 2867 Šteins," in *Proceedings of the 21st International Symposium on Space Flight Dynamics*, 2009.

[27] T. Morley, F. Budnik, M. Croon and B. Godard, "Rosetta navigation for the fly-by of asteroid 21 Lutetia," in *Proceedings 23rd International Symposium on Space Flight Dynamics*, 2012.

[28] A. Accomazzo, P. Ferri, S. Lodiot, J. L. Pellon-Bailon, A. Hubault, R. Porta, J. Urbanek, R. Kay, M. Eiblmaier and T. Francisco, "Rosetta following a living comet," 2016.

[29] B. Godard, F. Budnik, G. Bellei and T. Morley, "Multi-arc Orbit Determination to determine Rosetta trajectory and 67P physical parameters," 2017.

[30] P. Muñoz, V. Companys, F. Budnik, B. Godard, D. Pellegrinetti, G. Bellei, R. Bauske and W. Martens, "Rosetta Navigation during the End of Mission Phase," 2017.

[31] N. Attree, L. Jorda, O. Groussin, S. Mottola, N. Thomas, Y. Brouet, E. Kührt, M. Knapmeyer, F. Preusker, F. Scholten, J. Knollenberg, S. Hviid, P. Hartogh and R. Rodrigo, "Constraining models of activity on comet 67P/Churyumov-Gerasimenko with Rosetta trajectory, rotation, and water production measurements," *Astronomy and Astrophysics,* vol. 630, 10 2019.

[32] T. Kramer and L. Matthias, "Outgassing-induced acceleration of comet 67P/Churyumov-Gerasimenko," *Astronomy and Astrophysics,* 2019.

[33] D. Farnocchia, j. Bellerose, S. Bhaskaran, M. Micheli and R. Weryk, "High-fidelity comet 67P ephemeris and predictions based on Rosetta data," *Icarus,* 2020.

[34] S. R. Chesley and D. K. Yeomans, "Nongravitational accelerations on comets," in *Proceedings of the International Astronomical Union 2004 (IAUC197)*, 2004.

[35] A. S. Konopliv, J. K. Miller, W. M. Owen, D. K. Yeomans, J. D. Giorgini, R. Garmier and J.-P. Barriot, "A global solution for the gravity field, rotation, landmarks, and ephemeris of Eros," *Icarus,* vol. 160, no. 2, pp. 289-299, 2002.

[36] A. S. Konopliv, R. S. Park, A. T. Vaughan, B. G. Bills, S. W. Asmar, A. I. Ermakov, N. Rambaux, C. A. Raymond, J. C. Castillo-Rogez, C. T. Russell, D. E. Smith and M. T. Zuber, "The Ceres gravity field, spin pole, rotation period and orbit from the Dawn radiometric tracking and optical data," *Icarus,* vol. 299, pp. 411-429, 1 2018.

[37] A. S. Knopliv, C. F. Yoder, E. M. Standish, D.-N. Yuan and W. L. Sjogren, "A global solution for the Mars static and seasonal gravity, Mars orientation, Phobos and Deimos masses, and Mars ephemeris," *Icarus,* no. 182, pp. 23-50, 2006.

[38] F. L. Whipple, "A comet model. I. The acceleration of Comet Encke," *The Astrophysical Journal,* vol. 111, pp. 375-394, 1950.

[39] D. Björn and P. J. Gutiérrez, "Estimating the nucleus density of Comet 19P/Borrelly," *Icarus,* vol. 168, no. 2, pp. 392-408, 2004.

[40] Z. Sekanina, P. W. Chodas and D. K. Yeomans, "Tidal Disruption and the Appearance of Periodic Comet Shoemaker-Levy 9," *The Astronomical Journal,* 1993.

[41] B. Mardsen, Z. Sekanina and D. Yeomans, "Comets and non-gravitational forces," *Astronomical Journal,* vol. 78, pp. 211-225, 1973.

[42] M. Micheli, D. Farnocchia, K. J. Meech, M. W. Buie, O. R. Hainaut, D. Prialnik, N. Schörghofer, H. A. Weaver, P. W. Chodas, J. T. Kleyna, R. Weryk, R. J. Wainscoat, H. Ebeling, J. V. Keane, K. C. Chambers, D. Koschny and A. E. Petropoulos, "Non-gravitational acceleration in the trajectory of 1I/2017 U1 ('Oumuamua)," *Nature,* 2018.

[43] M. Krolikowska, "67P/Churyumov-Gerasimenko-potential target for the Rosetta mission," *Acta Astronautica,* vol. 53, pp. 195-209, 2003.

[44] K. A. J.-J. B. A. B. N. B. D. B.-M. U. C. F. C. M. R. C. J. D. K. B. F. N. F. S. A. F. S. G. T. I. G. Z. H. L. L. R. S. L. H. N. M. R. Kenneth C. Hansen, "Evolution of water production of 67P/Churyumov–Gerasimenko: an empirical model and a multi-instrument study," *Monthly Notices of the Royal Astronomical Society,* vol. 462, no. Suppl_1, pp. 491-506, 2016.

[45] D. K. Yeomans and P. W. Chodas, "An asymmetric outgassing model for cometary nongravitational accelerations," *Astronomical Journal,* vol. 98, no. 3, 1989.

[46] CCSDS , "Tracking Data Message - Recommended Standard, Issue 1, 503.0-B-1," 2007.

[47] California Institute of Technology, "DSN Telecommunication Links Design Handbook - Sequential Ranging - 203 Revision C," 2009.

[48] Budnik, Frank;, "Mathematical formulation for AMFIN," ESA, 2008.

[49] T. Morley and F. Budnik, "Effects on Spacecraft Radiometric Data at Superior Solar Conjunction," *Proceedings of the 20th International Symposium on Space Flight Dynamics,* 2007.

[50] M. Pätzold, M. Hahn, S. Tellmann, B. Häusler, M. K. Bird, L. J. Tyler, S. W. Asmar and B. T. tsurutani, "Coronal Density Structures and CMEs: Superior Solar Conjunctions of Mars Express, Venus Express, and Rosetta: 2004,2006, and 2008," *Solar Physics,* vol. 279, pp. 127-152, 2012.

[51] ESOC, "Rosetta Mission Operations Report (MOR # 205) Period [23 March 15 - 31 March 15]," 2015.

[52] ESOC, "Rosetta Mission Operations Report (MOR # 266) Period [23 May 16 - 30 May 16]," 2016.

[53] B. Godard, F. Budnik, P. Muñoz, T. Morley and V. Janarthanan, "Orbit Determination of Rosetta Around Comet 67P/Churyumov-Gerasimenko," 2015.

[54] G. Sitarski, "On the perihelion asymmetry for investigations of the nongravitational motion of comets," *Acta Astronautica,* vol. 44, pp. 91-98, 1994.

[55] T. Morley, F. Budnik, B. Godard, P. Muñoz and V. Janarthanan, "Rosetta Navigation from Reactivation until Arrival at Comet 67P/Churyumov-Gerasimenko," 2015.

[56] A. K. Verma, A. Fienga, J. Laskar, K. Issautier, H. Manche and M. Gastineau, "Electron density distribution and solar plasma correction of radio signals using MGS MEX and VEX spacecraft navigation data and its application to planetary ephemerides," *Astronomy and Astrophysics,* vol. 550, 2013.

[57] . Galileo Project Office, "Galileo Reference Troposphere Model for the User Receiver," Noordwijk, 2014.

[58] P. Muñoz, F. Budnik, V. Companys, B. Godard, C. M. Casas, T. Morley and V. Janarthanan, "Rosetta navigation during lander delivery phase and reconstruction of Philae descent trajectory and rebound," *25th International Symposium on Space Flight Dynamics,* 2015.

[59] L. Iess, S. Asmar and P. Tortora, "MORE: An advanced tracking experiment for the exploration of Mercury with the mission BepiColombo," *Acta Astronautica,* vol. 65, no. 5-6, pp. 666-675, 1 9 2009.

[60] L. Iess, M. Di Benedetto, N. James, M. Mercolino, L. Simone and P. Tortora, "Astra: Interdisciplinary study on enhancement of the end-to-end accuracy for spacecraft tracking techniques," *Acta Astronautica,* vol. 94, no. 2, pp. 699-707, 2014.

[61] P. Tortora, S. Crewell, G. Elgered, A. Graziani, P. Jarlemark, U. Loehnert, A. Martellucci, M. Mercolino, T. Rose and J. Schween, "AWARDS: Advanced microwave radiometers for deep space stations," in *Space Communications*, 2013.